Influence of Modeling Choices on Nonlinear-Dynamic Behavior of a Single-Layer Reticulated Dome

by

Akshay Arun Somkuwar

A thesis submitted in partial fulfilment of the requirements for the degree of Doctor of Engineering

Examination Committee:	Dr. Ryota Matsui
	Dr. Masaru Kikuchi
	Dr. Taichiro Okazaki
	Dr. Nobuo Takai

Doctoral Thesis No:

Division of Architectural and Structural Design

Graduate School of Engineering, Hokkaido University

December 2024

ABSTRACT

Nonlinear time history response analysis is a reliable approach for examining the large deformation of steel structures, particularly for the next generation structural design. The impact of modeling choices on the nonlinear response of steel structures has garnered significant attention in earthquake-prone regions. While the inertia force commonly retain the initial condition, the modeling of restoring and damping forces play a critical role in capturing nonlinear-behavior of steel structures. Fiber elements are frequently used to represent the nonlinearity of restoring forces because they can trace the propagation of plasticity along the length of structural members. However, the sensitivity of computational results of highly nonlinear-behavior, such as global buckling, local buckling and curvature distribution—depends heavily on the discretization schemes and element formulations. Observation of damping ratios by vibration tests have provided strong evidence that these ratios remain relatively constant across relevant vibrations modes. However, since the vibration frequencies of inelastic system differ from those of elastic system, the use of damping models based on initial stiffness can result in unintended spurious damping forces. This study examines the influence of modeling choices on the dynamic response of a reticulated dome, analyzed by nonlinear time history response analysis using the platform OpenSees.

A reticulated dome with a span of 40.0 m and a rise of 13.3 m supported entirely by pinned connections, was selected as a representative model of spatial structures for seismic risk estimation. The dome was designed to remain stable under dead load and sustain insignificant and moderate damage states when subjected to Taft ground motions, with peak accelerations scaled to 0.45g and 0.7g based on a previous seismic risk study. Round hollow structural sections (HSS) were used for the individual members of the reticulated dome. Fiber elements based on force- and displacement-based formulations were validated against physical test results of round HSS members with slenderness ratios ranging from 40 to 74, which were commonly used in the dome. The validation considered models with 2, 4, 8, 10 and 30 segments. The displacement-based fiber element with 8 segments demonstrated high-fidelity in predicting the global response of the dome members in the reticulated dome with high-fidelity, accounting for plastic curvature induced by global buckling within the contraction range of -0.5\% to 0.5\%.

The force- and displacement-based fiber elements with 2, 4, 8 and 10 segments were utilized to investigate the impact of the member discretization on the dynamic response of the inelastic dome. The displacement-based fiber element with 8 segments demonstrated the highest accuracy in capturing both the global system and component-level behavior of the dome. The

inherent damping of the reticulated dome was examined using three models: the initial-stiffness-proportional Rayleigh model, the tangent-stiffness-proportional Rayleigh model, and the modal-damping model. For the study of the damping models, the Taft ground motion and a suite of 28 pairs of ground motions selected by Table A-6C in (FEMA P695 2009), scaled to 1.3 times the design spectrum specified in Japanese Standard Law with a 10\% probability of exceedance in 50 years, was employed. For all ground motion cases, at least 95\% of the individual members exhibited contraction and elongation within ±0.5\%. This result affirmed the reliability of the computational outcomes, as they aligned with the validated behavior of the members. A representative damping ratio for the dome was calculated using the modal-damping model incorporating a step-by-step update based on elastic-plastic behavior. The representative damping ratios in all three directions for the initial-stiffness-proportional damping were 1.26 times the target damping ratio, while those for tangent-stiffness-proportional Rayleigh damping and modal-damping model were closely matched the target value. Among the damping models, the tangent-stiffness-proportional Rayleigh model produced the largest 84th percentile displacement, whereas the initial-stiffness-proportional Rayleigh model yielded the smallest. When the tangent-stiffness-proportional Rayleigh model was used, it produced the most severe damage evaluations compared to the initial-stiffness-proportional Rayleigh model and the modal damping model. The initial-stiffness-proportional Rayleigh model has a potential to yield less unconservative evaluation of damage states for spatial structures compared to the other two models. The modal-damping model is recommended for the seismic risk analysis to mitigate the effects of the spurious damping forces and ensure more accurate assessment for the reticulated domes.

Subsequently, to capture local buckling induced strength and stiffness deterioration in a steel concentrically braced frame (CBFs) calibration and extension of material model proposed by Suzuki and Lignos termed the SL Model was conducted. The SL Model was integrated into OpenSees to reproduce the hysteretic behavior of steel braces with round-HSS. The parameters for the SL Model were calibrated through regression analysis on round-HSS stud column data. The calibrated SL model was validated against round-HSS braces with slenderness ratios ranging from 16 to 103, and diameter-to-thickness ratios ranging from 16 to 63. The calibrated SL material model is supposed to be implemented in an 8-story chevron braced frame. In this frame, the lateral loads were primarily resisted by chevron braces, while the beams were designed as simply supported and proportioned to remain elastic under tension forces and brace compression, in accordance with the US Provisions.

ACKNOWELDGEMENT

This thesis is the result of computational work conducted at Laboratory of Structural engineering, Department of Architectural and Structural Design, from where I was able to gather the data and knowledge regarding the research.

First and foremost, I would like to extend my deepest and most sincere gratitude to my supervisor Dr. Ryota Matsui for his guidance, support, and patience over the past four years. Without his mentorship, I would not have been able to complete this research. I am immensely thankful for his ability to steer me back on track whenever I felt lost or uncertain about how to proceed. I am indebted to him for providing me the opportunity to conduct this research under his supervision.

I would also like to express my heartfelt thanks to Prof. Taichiro Okazaki for his invaluable advice, which were fundamental in completion of this research and thesis.

I would like to specially thank Dr. Dias, and Raheem Ibrahim, for their constant support, both technically and on a personal level, throughout this journey. I am also grateful to my colleagues from research group, in particular Yi Qie, LI Jionghui, Martin Somarriba, Lillian Lai, Rafiqul, Ota Massahiro and the many other students at the Laboratory of Structural Engineering, Hokkaido University, for their collaboration and friendship.

Above all, I would like to thank my family, especially my brother Pranay Somkuwar, my sister Poonam Somkuwar, for their love and support, without them I would not be here. I am also deeply thankful to my friends Vrushabh, Rashmi, and Lipsa for their unwavering support.

Finally, I am truly grateful to JICA for the financial support and granting me the opportunity to study in Japan over the past three years through the IITH-FRIENDSHIP scholarship.

1 Table of Contents

List of Figures

List of Tables

1 INTRODUCTION

1.1 General

The main objective of the seismic design is to accurately predict dynamic behavior of structures subjected to ground motions such as maximum displacement, velocity and acceleration responses, base shear, and shear distribution over the height. In addition to these responses, for inelastic system, the plastic deformation capacity, energy dissipation mechanism, and seismic risk evaluation are critical to assess the performance of steel structures. Nonlinear time history response analysis, i.e., numerical integration scheme is a reliable approach for examining elastic-plastic behavior of steel structures, particularly for the next generation structural design. Researchers have proposed numerous strategies of modeling to track the large deformation of component-level response in steel structures, to compute the dynamic response of steel structures with enhanced quality. The impact of modeling choices on the outcomes of nonlinear time history response analysis for steel structures has garnered significant attention in earthquake-prone regions.

Numerical integration provides the dynamic response of structures step-by-step by resolving the equation of motion. For inelastic system, while the inertia force commonly retains the initial condition, the parameters for restoring and damping forces alter depends on the elastic-plastic behavior. As shown in Figure 3.1 (a) Schematic of beam-column element for brace specimen (b) material parameters of Giuffre-Menegotto-Pinto material model, fiber elements track the propagation of plasticity along the length of structural members to represent the nonlinearity of restoring force and stiffness at an instant. The fiber elements are frequently used because the tracking the propagation of plasticity is relatively reliable. However, the sensitivity of computational results of highly nonlinear-behavior, such as global buckling, local buckling, and curvature distribution—depend heavily on the discretization schemes, and element formulations.

Past vibration tests on structures observed the damping ratios of structures rather remain relatively constant across relevant vibration modes (Tatemichi et al. 1997). By contrast, since the frequencies of inelastic system differ from elastic system, the use of damping models based on initial stiffness can result in untended spurious damping forces.

1.2 Objectives

The main objectives of this dissertation are investigation on the influence of modeling choice on the nonlinear-behavior of steel structures as follows:

(1) Investigate the impact of discretization scheme on the elastic-plastic dynamic response of a reticulated dome;
(2) Investigate the influence of damping models on the nonlinear displacement response and the equivalent damping ratio of the reticulated dome;
(3) Extend SL material model to circular HSS section to capture local buckling induced strength and stiffness degradation
(4) Analyse the structural response of a Chevron braced frame considering local buckling behavior of braces.

1.3 Outline

To achieve these goals, this dissertation composed of 7 Chapters:

Chapter 1 discuss the background, scope of the research, research gap and objectives of the research.

Chapter 2 presents current state of knowledge through review of the past research on the axially loaded members and inherent damping in spatial structures.

Chapter 3 discusses the numerical approach for modeling axially loaded members used in the numerical analysis of reticulated dome structures within the finite element software OpenSees, along with their validation against test data. The chapter also examines the force-deformation response and the curvature distribution along the length of axially loaded members.

Chapter 4 discusses the numerical modeling of the reticulated dome structure and the modal analysis of the dome. It further elaborates on the material models to be used in modeling the dome in Adina for benchmarking purposes. The chapter also covers the response spectrum and ground motions to be utilized in conducting transient analysis.

Chapter 5 presents the elastic and inelastic responses of the reticulated dome subjected to the Taft ground motion scaled to 0.5g and 0.7g. The chapter discusses the peak displacement response, base shear response, and drift experienced by the reticulated dome during elastic analysis. For the inelastic response, it examines the effect of the number of segments per member on the dome's behavior. Additionally, this chapter explores the concepts of equivalent and representative damping ratios as parameters to differentiate the responses of various damping models and element formulations. It also investigates the effects of damping models on deformation, frequency, deformation distribution on the dome's surface, member-level response, and observed failure patterns, concluding with key findings.

Chapter 6 discusses the seismic risk evaluation of lattice dome to 28 pairs of ground motion pairs followed by the key observations.

Chapter 7 delves into strength and stiffness degradation induced by local buckling and the corresponding modeling approach within the OpenSees framework. This chapter details the calibration process for the SL material model in OpenSees for round HSS sections, using monotonic stress-strain curves of round HSS stub columns. It further validates the calibrated model against experimental tests conducted on braces with varying slenderness and compactness ratios. Chapter 8 provides main conclusion of this research.

2 LITERATURE REVIEW

2.1 General

This section discusses on the background of axially loaded members found in spatial structures and conventional braced frames, followed by the background on inherent damping modes available in the literature.

2.2 Modeling choices for axially-loaded members

Numerical models for axially-loaded members such as truss elements are commonly applied to individual members in spatial structures and steel braces in braced frames. Round hollow structural sections (HSS) are normally used for the individual members in the spatial structures; therefore, the following section firstly addresses the validation studies of axially-loaded members in the context of steel braces.

Extensive research has been conducted worldwide on the seismic behaviour of steel braces, supported by experimental studies (Black, Wenger, and Popov 1980; Tremblay 2002; Shaback and Brown 2003; Goggins et al. 2005; Agüero, Izvemari, and Tremblay 2006; Fell et al. 2009; Takeuchi and Matsui 2011, Takeuchi and Matsui 2015; Matsumoto 2016) and many others. These investigations examined the effects of various design parameters—such as cross-sectional properties, slenderness ratios, connection types, and loading protocols—on the cyclic performance of steel braces. This body of work established critical seismic design parameters for concentrically braced frames (CBFs) and formed the foundation for analytical models simulating the inelastic cyclic behavior of braces at both member and system levels.

According to the terms suggested by Ikeda and Mahin (1986) modeling choices for simulating seismic brace hysteresis fall into three categories: physical-theory models (Nonaka 1973), phenomenological models (Ikeda, Mahin, and Dermitzakis 1984; Ikeda and Mahin 1986) and numerical models (Uriz, Filippou, and Mahin 2008; Fell et al. 2009; Karamanci and Lignos 2014). In the physics-based models, the brace is represented by two elastic beam-column elements connected by a plastic hinge at midpoint which typically exhibits elastic-perfectly plastic behavior (Nonaka 1973; Ikeda and Mahin 1986). Upon load reversal, the hysteretic response is computed through closed-form solutions that trace the brace's behavior.

While these models are simple and reasonably accurate, they cannot capture local buckling or the spread of plasticity along the axial direction.

The phenomenological models, in contrast are developed by fitting certain hysteretic rules, or mathematical formulas, to measured or simulated hysteretic behavior of steel braces. Wakabayashi et al. (1977) developed a versatile model that is popularly used in Japan, Zheng and Fan (2019) calibrated a model to capture degradation in tensile and compressive strength as well as fracture. Such phenomenological models are computationally efficient, but their applicability is bounded by the range of data used for calibration. Jin and El-Tawil (2003) proposed a stress-resultant framework for tubular steel braces, which accounts for the spread of plasticity and stiffness deterioration due to local buckling. Although computationally efficient, the accuracy of these models is constrained by the quality and range of the experimental data used for calibration.

The numerical models provide detail simulations by discretizing braces into numerous finite elements, with material properties defined by plasticity theories. Advances in finite element methods enable simulations of brace failure under low-cycle fatigue, such as through the crack void growth model (Fell et al. 2009). These models accurately replicate both local and global brace behavior, but are computationally expensive, limiting their application to large-scale structural assessments. To address this, fiber-based models—such as those implemented in OpenSees (McKenna, Scott, and Fenves 2010)—offer a computationally efficient alternative. Fiber-based models effectively simulate cyclic and low-cycle fatigue responses with reasonable accuracy for global and local behaviors (Uriz and Mahin 2008; Karamanci and Lignos 2014). However, they are best suited for slender braces or axial members where global buckling precedes local buckling. This limitation makes them less effective for simulating stocky braces. Given the importance of accurately modeling local buckling to understand the actual behavior of braced frames and spatial structures, the limited research in this area presents a critical gap.

To capture the realistic behavior of axially-loaded members in spatial structures, researchers have chosen different element types: elastic-plastic truss elements (Ishikawa and Kato 1997; Sadeghi 2004), calibrated phenomenological elements (Ikeda, Mahin, and Dermitzakis 1984; Ikeda and Mahin 1986), three-dimensional finite element models (Fell et al. 2009; Haddad 2017). One of the most refined elements for the axially-loaded members in spatial structures is a model aligned in a series of three plastic hinges and two elastic beam-column elements proposed by S. Kato, Ueki, and Mukaiyama (1997), illustrated in Figure 2.1. However, such simplified models do not represent the longitudinal spread of yielding in individual members. As described earlier, the fiber elements capture the spread of plasticity by tracing the elastic-plastic uniaxial response of fibers, or discretized segments of the cross sections. The elements are formulated by imposing equilibrium (force formulation) or compatibility (stiffness formulation) at discrete sections using interpolation functions. The discretization approaches for individual members depends on the type of element employed (Zhong et al. 2018; D. Yang et al. 2018; F. Yang, Zhi, and Fan 2019; Vazna and Zarrin 2020) achieving balance between accuracy and computational efficiency.

2.3 Inherent damping models

All building structures experience some level of energy dissipation when subjected to motion. In numerical simulations, this energy loss is attributed to the nonlinear behavior of structural members and inherent damping mechanisms. Among various damping mechanisms, two widely discussed models include the friction damping model. This model stems from interfacial damping mechanisms between structural components, such as connections and non-structural elements like partitions and facades, as well as other frictional forces within the system. Experimental studies have revealed that most energy dissipation mechanisms in structures are more influenced by displacement amplitude than by structural frequency. Consequently, the friction damping model is considered a highly suitable representation for describing damping behavior.

Table 2.1 provides an additive list of available inherent viscous damping models in the literature, as described by Fukutomi et al. (2020), where $[c]$ is the damping matrix, $[m]$ is the mass matrix, $[k]$ is the stiffness matrix, a_n is the corresponding coefficient for mode n, ζ_n is the damping ratio for mode n, $\{\phi_n\}$ is the eigenvector of mode n, and $[\Phi]$ is the modal matrix. $[k^*]$ and $a_n{}^*$ are computed based on tangent stiffness of the inelastic system. The available damping models in five software frameworks for simulating of the behavior of structural systems under dynamic loading. These include the open-source software OpenSees and four general-purpose products: ADINA, SAP2000, Abaqus, and ANSYS. Five frameworks provide Damping Models 1, 2, 5, 9 and 12, i.e., mass-proportional model, initial-stiffness-proportional model, initial-stiffness-proportional Rayleigh model, Caughey series, and modal-damping model, respectively. These popular models premise the initial parameters of both mass and stiffness, which result in constant damping coefficients throughout dynamic analysis. Damping Models 3, 4, 6, 7 and 8 require the step-by-step eigenvalue analysis. Damping Model 7 retain the original damping ratio for inelastic systems suggested by Charney (2008). Hall (2006) suggested Damping Model 8 as a refined approach to reduce the impact of mass-proportional term. Bernal (1994) recommended Damping Model 10, which incorporates the Caughey model with term n set to less than or equal to zero, to address issues related to damping force in springs with no rotational mass. Shing and Mahin (1987) introduced a tangent-stiffness-proportional term as Damping Model 11 to eliminate the spurious damping force caused by higher-mode effects. Fukutomi et al. (2020) proposed that Damping Model 13 provides the most accurate definition of the damping matrix, as it retains a constant damping ratio for each vibration mode. Damping Model 14 provides the damping ratios specifically applied to structural elements used in vibration-controlled and seismically isolated structures. Damping Model 15 termed Band-Limit Damping caps the damping ratio over a specific range of frequencies with the low-pass filter operator, allowing for a more accurate simulation of realistic energy dissipation.

Tatemichi et al. (1997) conducted a vibration test on a suspendome, shown in Figure 2.2, to capture the vibration frequencies and damping ratios. Two electromagnetic exciters were attached to the roof of the dome, along with 16 accelerometers to measure the amplitude of the dome for a series of steady-state and free vibration tests. The observations showed that the damping ratios of the structure remained relatively constant across the relevant vibration modes. By contrast, since the frequencies of an inelastic system differ from those of an elastic system, the use of damping models based on initial stiffness can result in unintended spurious damping forces.

For conventional building structures, Hall (2006) and Charney (2008) investigated the Rayleigh model of an elastic-plastic system in which the vibration frequencies decreased. These studies pointed out the inaccuracy that arose from the use of the initial stiffness for the Rayleigh model, which may induce spurious damping forces in building structures, to mitigate the problem, the tangent-stiffness proportional Rayleigh damping model was recommended. Medina and Krawinkler (2004) addressed that the spurious damping forces arise at the degree of freedoms, leading to an underestimation of the system’s peak displacement demands and an overestimation of internal forces for the element in the system that do not experience changes in stiffness. Chopra and Mckenna (2016) demonstrated the plastic hinge rotation of a 20-story steel moment frame computed using initial-stiffness-proportional Rayleigh model was approximately 2 to 10 times lower than that computed using modal-damping model applied to all modes when using concentrated plasticity model. In contrast, the difference in the plastic hinge rotation between the damping models was limited when the distributed hinge model was used. Gremer, Adam, and Furtmüller (2023) examined the effect of Rayleigh model by a comparative study of different coefficient choices on the vertical acceleration response of steel moment frames. Authors found that assigning the damping coefficient for the higher-frequency component of Rayleigh model to the fundamental vertical vibration mode produced a more realistic vertical acceleration response compared with that assigning it to the mode where the cumulative horizontal or vertical effective modal masses reached 95% of the total mass, a common practice for perceived accuracy. Kitayama and Constantinou (2023) conducted an extensive numerical study of the effect of various damping models on engineering demand parameters, specifically noticeable difference in the mean annual frequency of exceeding these engineering demand parameters between models with 2% or 5% damping ratio and those with no damping was found. However, aside from models using element-specific initial-stiffness proportional damping, the impact of the damping models on the mean annual frequency on the engineering demand parameters was generally minimal. Based on these findings, Kitayama et al. recommended a damping model with virtual linear viscous dampers without damping force caps for its simplicity.

In spatial structures, as opposed to conventional frames many higher modes significantly contribute to the response of the structure due to their complex geometry and dynamic characteristics. The modal frequencies in this type of structures are closely spaced, if appropriate modes are not considered, Rayleigh damping may provide insufficient damping ratios for intermediate modes between the two specified modes and larger damping ratios for modes exceeding the higher mode within the specified range. To address the impact of different modes, D. B. Yang, Zhang, and Wu (2010) suggested coefficient for the Rayleigh model based on the contribution of strain energy rather than mass participation, to retain consistent damping ratio across the significant modes. In a related study, F. Yang, Zhi, and Fan (2019) proposed a complex damping model distinct from Rayleigh model. To integrate complex damping into the computer program for response history analysis with numerical integration, five integer-order derivative parameters of the material constitutive law were introduced. The proposed model maintained constant damping ratios across all vibration modes without introducing non-causality. Consequently, the choice of modelling for inherent damping against various structural types has attracted considerable interest.

2.4 Dynamic-behavior of spatial structures

The dynamic-behavior of steel spatial structures has received much attention in earthquake-prone areas, as described in the *Guide to Earthquake Response Evaluation of Metal Roof Spatial Structures* (IASS WG8 2019). The premise of structural design of spatial structures are commonly based on linear elastic response analysis: static analysis using equivalent static loads, modal response spectrum, or time history response analysis are available. An important feature of spatial structures is that many higher modes with closely spaced modal frequencies contribute to their dynamic response, making the analysis results highly dependent on modelling choices. For structures with closely spaced and coupled frequencies, the Complete Quadratic Combination (CQC) rule of modes is a computationally effective approach to estimate the peak elastic responses of these structures (Wilson, Der Kiureghian, and Bayo 1981). Further, Takeuchi, Ogawa, and Kumagai (2007) demonstrated that the acceleration and displacement response of domes and cylindrical shells could be estimated using the CQC modal combination rule with only 4 principal vibration modes covering more than 80% of the total effective mass ratio of the structure.

Despite the intent of structural design provisions (Architectural Institute of Japan (AIJ) 2016) to prevent significant loss of strength due to buckling or yielding of individual members, damage to spatial structures has been observed after past earthquakes. A notable example is damage to many school gymnasiums, where roof braces buckled, potentially leading to failure at their bracing bolted connections (IASS WG8 2019), as shown in Figure 2.3. Currently, there are limited guidelines available for the nonlinear time-history response analysis of spatial structures. More than their elastic response, the computed nonlinear response of spatial structures may be highly dependent on modelling choices, especially concerning structural element and damping. The axially-loaded members comprising spatial structures can undergo substantial changes in stiffness due to flexural global buckling in compression and subsequently recovery of axial stiffness in tension. As described in the preceding section, although numerous approaches were proposed, fiber element is one of the most efficient and accurate models to reproduce the deterioration behavior due to local buckling and yielding along the length of the axially-loaded members.

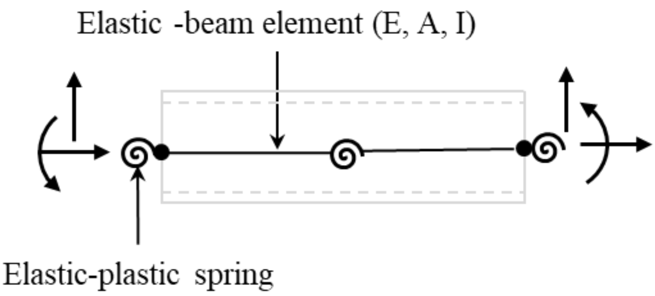

Figure 2.1 Plastic hinge model for axially-loaded member (based on S. Kato, Ueki, and Mukaiyama 1997)

Figure 2.2 Vibration test on a full size suspen-dome (source: Tatemichi et al. 1997)

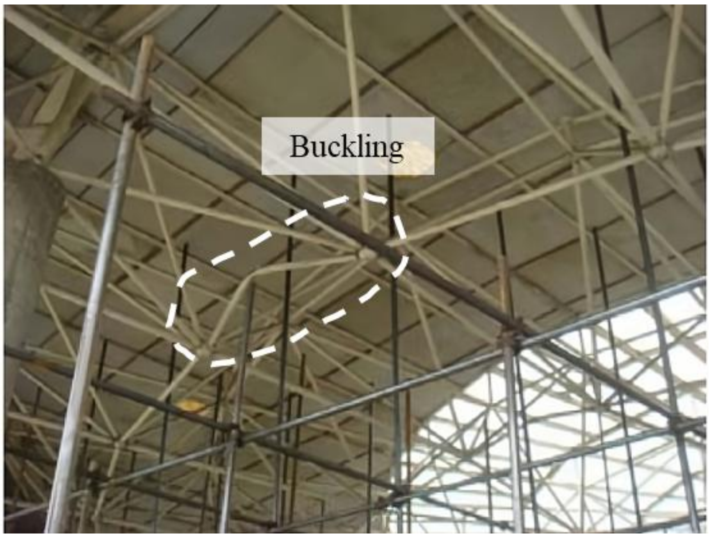

Figure 2.3 Buckling of a member observed in a grid shell located in Mianyang City after the Wenchuan Earthquake (2008) (source: IASS WG8 2019)

Table 2.1 Damping models (Fukutomi et al. 2020)

No.	Equation	Open Sees	ADINA	SAP 2000	Abaqus	ANSYS
1	$[c] = a_0[m]$	○	○	○	○	○
2	$[c] = a_1[k]$	○	○	○	○	○
3	$[c] = a_1[k^*]$	○	○			
4	$[c] = a_1^*[k^*]$					
5	$[c] = a_0[m] + a_1[k]$	○	○	○	○	○
6	$[c] = a_0[m] + a_1[k^*]$	○	○			
7	$[c] = a_0^*[m] + a_1^*[k^*]$					
8	$[c] = a_0[m][k]^{-1}[k^*] + a_1[k^*]$					
9	$[c] = [m]\sum_{n=0}^{N-1} a_n([m]^{-1}[k])^n$					○
10	$[c] = a_{-1}[m][k]^{-1}[m]+a_0[m]$					
11	$[c] = a_{-1}[m][k]^{-1}[m] + a_0[m] + a_1[k^*]$					
12	$[c] = [m]\left(\frac{\sum_{n=0}^{N}(2\zeta_n\omega_n)}{M_n}\{\phi_n\}\{\phi_n\}^T\right)[m]$	○	○	○	○	○
13	$[c] = [m]\left(\frac{\sum_{n=0}^{N}(2\zeta_n\omega_n)}{M_n}\{\phi_n^*\}\{\phi_n^*\}^T\right)[m]$					
14	$[c] = [m][\Phi][\backslash 2\zeta_n\omega_n][\Phi]^T[m]$		○			○
15	$\{f_d\} = \frac{\eta\sum_{n=1}^{N}(2\alpha_n)}{\omega_{cn}}L_n\{\dot{f}_0\}$				○	

3 VALIDATION OF MEMBERS IN A RETICULATED DOME

3.1 Introduction

Domes are one of the oldest structural forms and have been used in architecture since the earliest times. They enclose a maximum amount of space with a minimum surface and can be very economical in terms of materials (Makowski 1962). The axial force dominantly acts to the individual members in reticulated domes, whose behaviour is approximately identical with steel braces in multi-story braced frames. Since a reticulated dome consist of members of varying slenderness ratio (approximately 30 to 60) this section is aimed at understanding the force deformation relationship of axial member at global level and curvature distribution along the length of axially loaded member.

3.2 Numerical Study on Axial member

The analytical models for steel axial members are typically categorized as follows: phenomenological models (Ikeda, Mahin, and Dermitzakis 1984; Ikeda and Mahin 1986); segmented beam-column models (Agüero, Izvemari, and Tremblay 2006; Uriz, Filippou, and Mahin 2008; Karamanci and Lignos 2014); and three-dimensional finite element models (Fell et al. 2009; Haddad 2017). In this study, the segmented beam-column models using force and displacement formulation with fiber discretization, were selected to account for the inelastic interaction between the axial force and flexural moment of the element for the axial members, which are based on the assumption of Euler Bernoulli theory in which plane section remain before and after the deformation. For the modeling of axial member, the following recommendations were suggested for use of the beam-column model element using force formulations to capture the evolution of inelastic response: the minimum number of subdivisions should be two; the initial camber displacement at the midspan should be 0.05 to 0.1% of the total length; and the number of layers across the depth of section should be ten to fifteen (Uriz, Filippou, and Mahin 2008). The type of the element formulation was validated to appropriately reproduce the response of axial members having the slenderness ratio close to the members in the reticulated dome. It should be noted that this numerical model is applicable to the axial members folded at the midpoint, excluding other failure modes. Consequently, the validation was conducted exclusively using tests where failure occurred at the midpoint. Table

3.1 shows the axial member employed as examples for validation to reproduce global buckling induced degradation by fiber elements with force- and displacement-based formulation. Figure 3.1 illustrates the schematic view of the fiber elements for refinement of axial members. All specimens were pin to pin supported. The specimens were subdivided into two, four, eight, ten, and thirty elements for comparative study between simulated and tested response. The initial camber displacement at the midpoint of the axial member was defined as 0.1% as suggested by the past study (Uriz, Filippou, and Mahin 2008). To monitor the inelastic behaviour of members, the integration rules of Gauss-Lobatto with five integration points were utilized for force-based fiber elements (Karamanci and Lignos 2014) and Gauss-Legendre with minimum of three integration points were utilized for displacement-based fiber elements because the accuracy of these elements depends on the mesh refinement (Neuenhofer and Filippou 1997). The section of each element was subdivided by 16 fibers in the circumferential direction and 4 fibers in the radial direction. The value of the yield strength was identical with the measured yield strength from the tension coupon tests. The Giuffre-Menegotto-Pinto model, namely Steel02 in OpenSees, was used for the hysteretic response of material with kinematic and isotropic hardening. As recommended by the past studies (Uriz and Mahin 2008; Agüero, Izvemari, and Tremblay 2006), parameters for evolution of strain hardening were determined as follows: for transition from elastic to plastic state, R_0 = 25, cR_1 = 0.925, and cR_1 = 15.0; for the isotropic hardening, a_1 = a_3 = 0.0005, and a_2 = a_4 = 0.01; and for the kinematic hardening, b is set to 0.001.

Figure 3.2 and Figure 3.3 show the force-deformation relationship under cyclic loading for force- and displacement-based fiber elements respectively. As observed from the figures it is evident that all subdivision is able to capture the peak compressive strength with sufficient accuracy. For the case of KL/r = 74, numerical simulation captures the cyclic response with sufficient accuracy along with the post buckling stiffness, similar response was observed for KL/r = 53. However, for the relatively stockier axial member with KL/r = 40 although the peak compressive strength was captured with sufficient accuracy, the numerical model predicted stiffer response in post-buckling phase, the selected fiber element was not able to capture the local buckling explicitly, such as effect of degradation in stiffness and strength which will lead to pinching effect. The buckling capacity (N_{cr}) was calculated according to the section E3 of AISC 360-16, the ultimate compressive strength (N_u) was taken as the 0.3 times the N_{cr}. The tensile capacity (N_y) was calculated as tensile strength (σ_y) times the gross area of the section and the effective length factor K was set 1.0. While the force- and displacement-based fiber elements provided essentially the same hysteretic response of the axial members, the selection of the formulation and the subdivisions plays an important role in determination of the local behaviour in the members, which affects the inelasticity of section. Figure 3.4 and 3.5 show the impact of the subdivisions on the curvature distribution along the axial members at the identical axial contraction of 0.11% at the time of overall buckling for the cases of *KL/r* = 74 and 53, and axial contraction of 0.08% for *KL/r* = 40. For both the formulations, it can be observed that if the number of subdivisions increased the curvature distribution decreases in the vicinity of the midpoint, while the cyclic response nearly identical for all subdivision. With less subdivision both force- and displacement- based fiber model tends to produce higher curvature at the middle which corresponds to increase in moment based on the constitutive relationship for the material (Uriz, Filippou, and Mahin 2008). Although, it was not validated which model provided the best solution in determination of local behavior in the axial members, but further examination including numerical simulation of test will be performed. The current study focused on the force-deformation response, where the number of subdivisions had no significant impact. However, for fatigue and fracture failure, curvature distribution plays a critical role, a finer subdivision would have been more appropriate. Therefore, a compromise was made to use 8 subdivisions, as it provided a curvature distribution similar to that of 10 and 30 subdivisions, while reducing computational time.

3.3 Conclusions

The chapter presents numerical model for the cyclic behaviour of axial member. The numerical model consists of force- and displacement based-fiber element. The response of the element can be derived by integration of the uniaxial stress strain relationship of the fibers and can account for kinematic and isotropic hardening. The large displacement geometry is included in the non-linear transformation of the force-deformation relation of the axially-loaded members using fiber elements following corotational formulation concept. The current modeling approach is applicable to the axial member which are failing at the middle due to compression. For axially-loaded members, the force-based fiber element with 2 segments effectively traced the force-displacement relationship. Conversely, for displacement-based fiber elements require a minimum of 8 segments to accurately predict the measured global response of these members, accounting for plastic curvature induced by global buckling. Even though the slenderness ratios of these axially-loaded members were out of the range that was used for validation of the fiber-based element in the study performed by past researchers (Uriz, Filippou, and Mahin 2008), similar conclusions were achieved, which shows the robustness of the fiber modeling:

1. Significant impact of element subdivision was not observed for the fiber elements with both force- and displacement formulations. All cases of subdivision were able to capture the peak compressive strength of the axial member with sufficient accuracy.
2. For axial member in which overall buckling (*KL/r* = 74 and 53) occurs before the local buckling the post buckling stiffness was sufficiently captured by the numerical model.
3. For axial member (*KL/r* = 40) in which local buckling occurs before or simultaneously with overall buckling, the numerical model predicted stiffer response post buckling. The simulated response closely mirrored the tested response within the range of normalized deformation δ/L -0.5% to 0.5%.
4. The selected numerical approach cannot capture the pinching effect arises from the occurrence of local buckling because the numerical formulation is based on the Euler Bernoulli theory in which plane section remain before and after the deformation.
5. For both the formulations, it can be observed that if the number of subdivisions increased the curvature distribution gets affected while the cyclic response nearly identical for all subdivision. With less subdivision both force- and displacement-based fiber model tends to produce higher curvature at the middle which corresponds to increase in moment based on the constitutive relationship for the material.

Table 3.1 Axial member specimen

Specimen	kL/r	L [mm]	D [mm]	t [mm]	A [mm^2]	σ_y [N/mm^2]	E [N/mm^2]
721	70	2219	89.1	4.2	1120.2	354	205000
528	53	1622	89.1	3.2	863.6	349	205000
C3N	40	1930	139.8	3.5	1498.7	254	205000

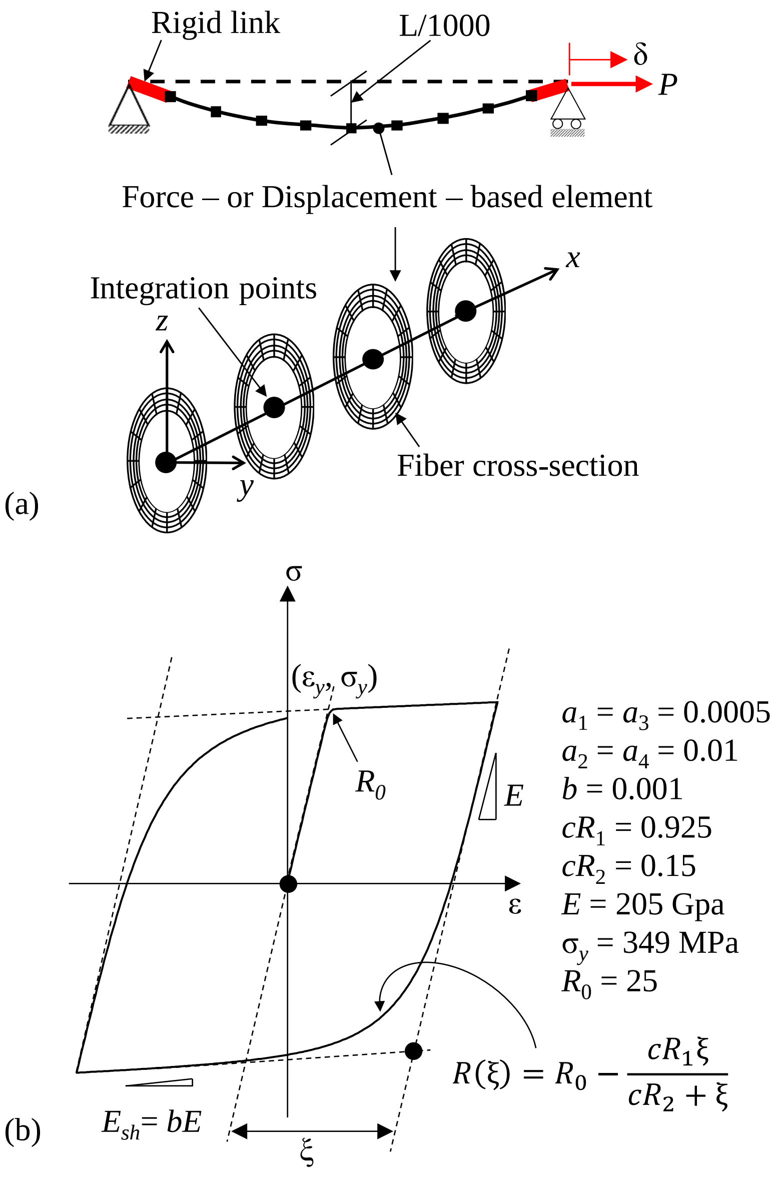

Figure 3.1 (a) Schematic of beam-column element for brace specimen (b) material parameters of Giuffre-Menegotto-Pinto material model

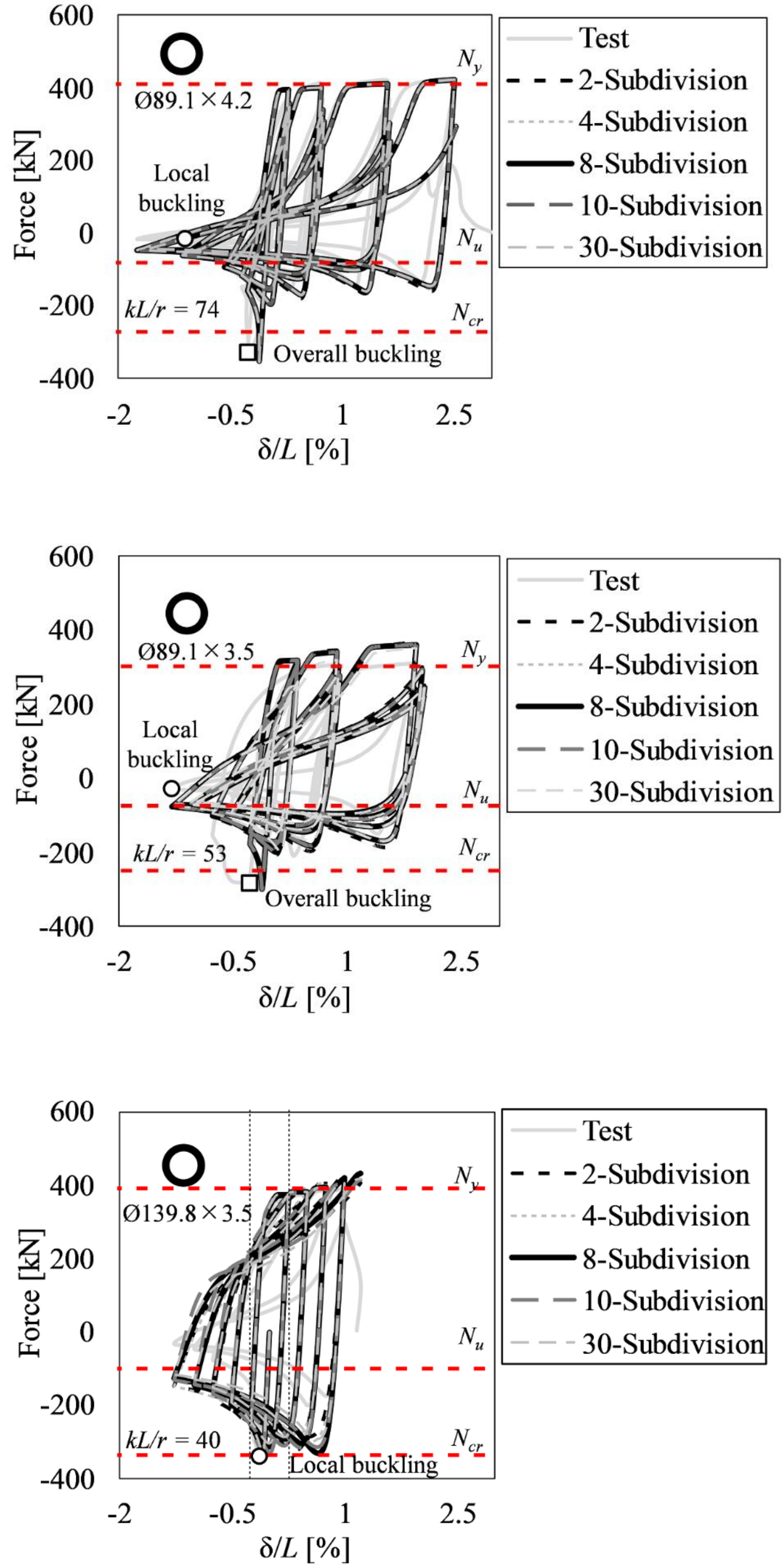

Figure 3.2 Force – deformation response for force-based fiber element:

(a): 721; (b) 528; and (c) C3N

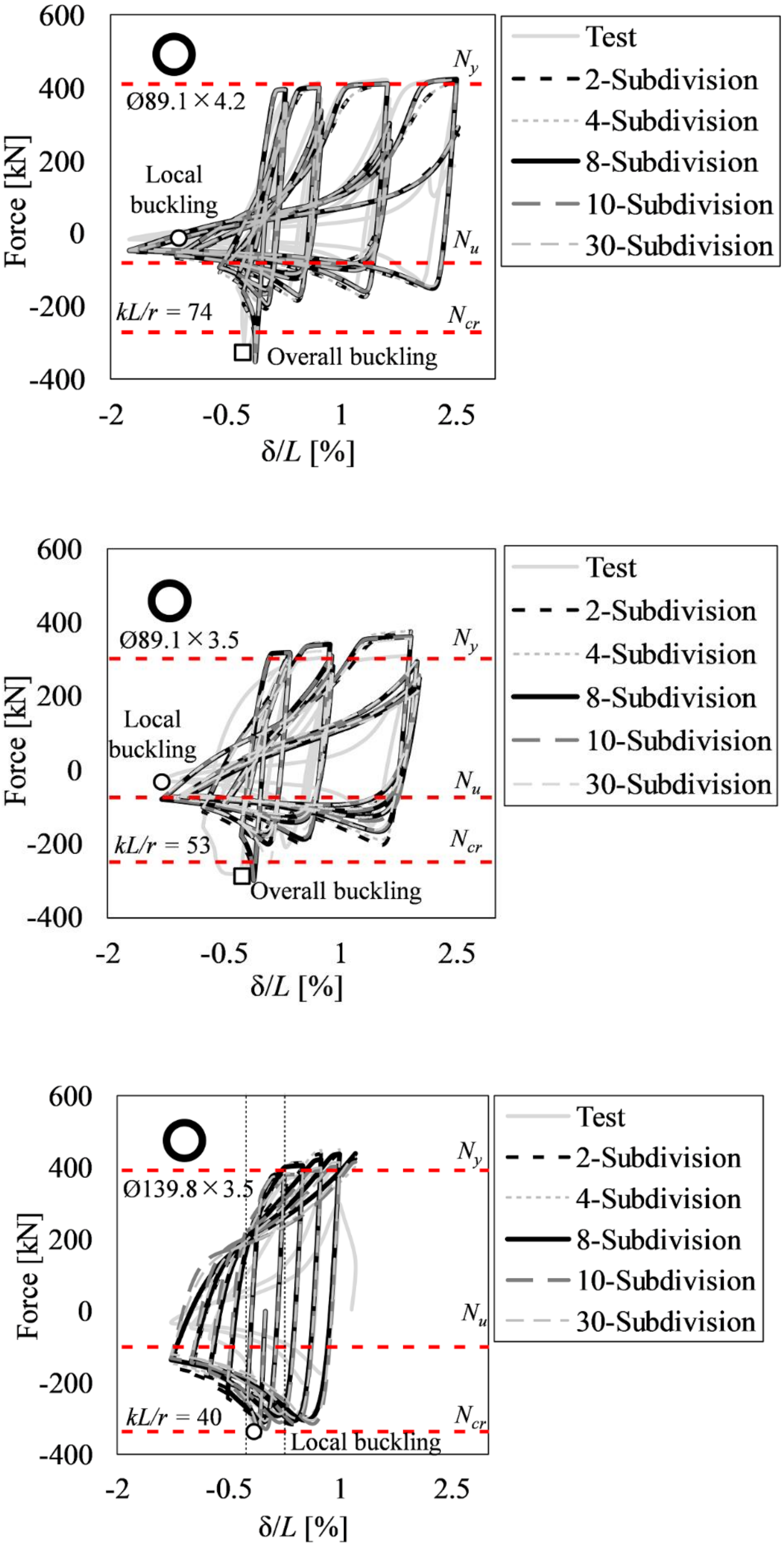

(a)

(b)

(c)

Figure 3.3 Force – deformation response for displacement-based fiber element:

(a): 721; (b) 528; and (c) C3N

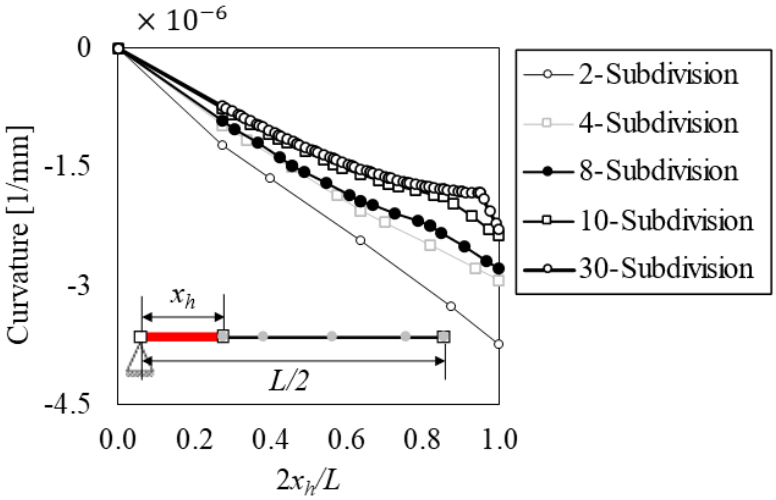

(a)

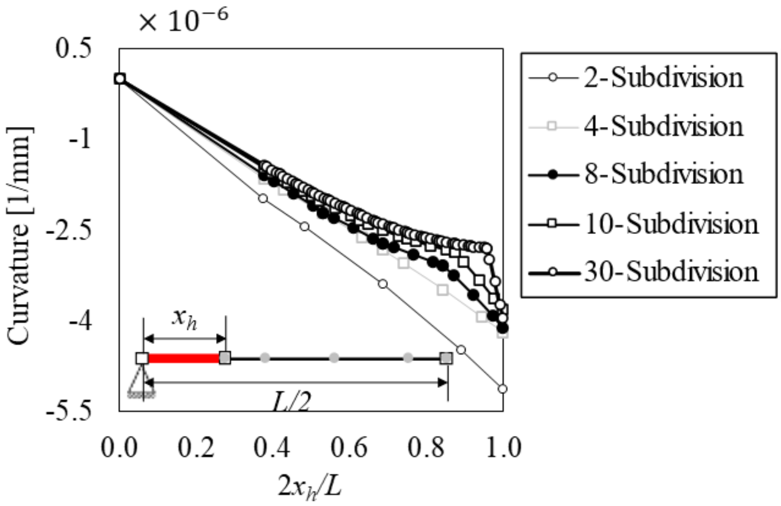

(b)

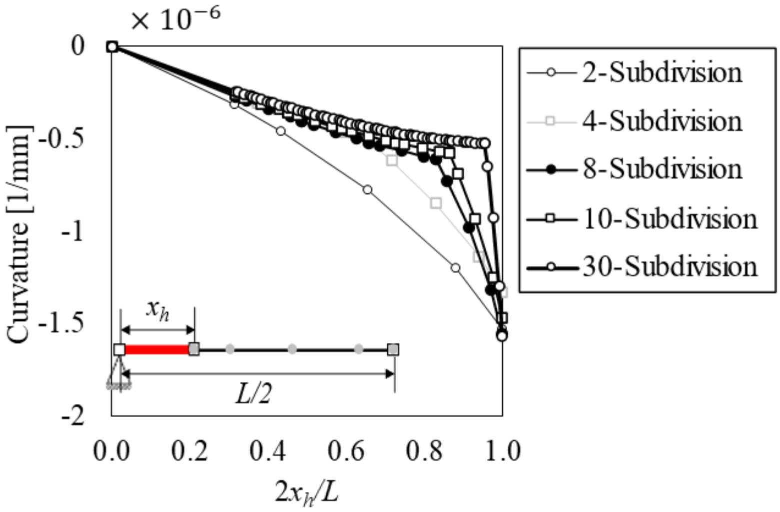

(c)

Figure 3.4 Curvature distribution for force-based fiber element

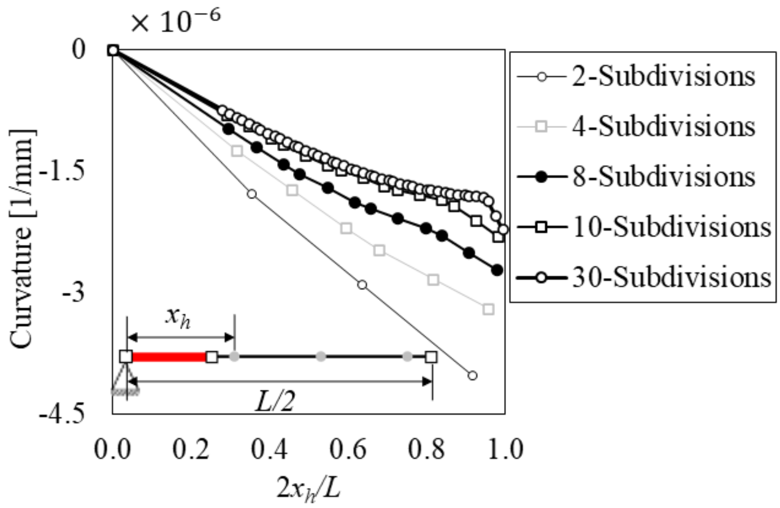

(a)

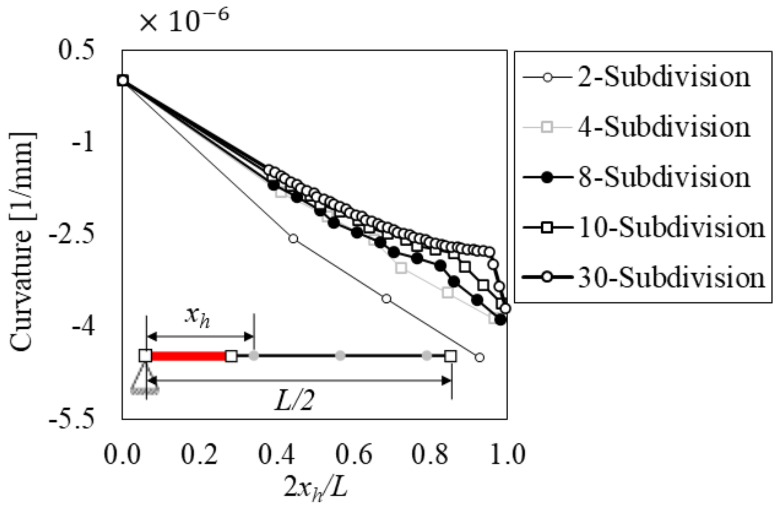

(b)

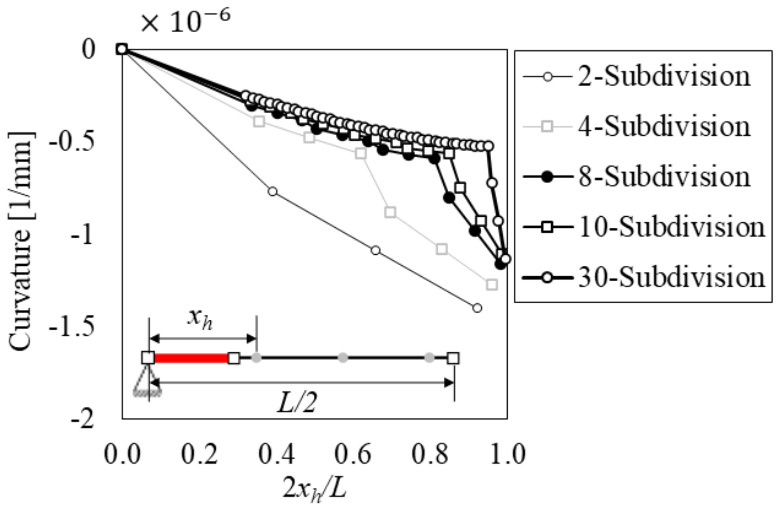

(c)

Figure 3.5 Curvature distribution for displacement-based fiber element

4 NUMERICAL MODELING OF LATTICE DOME

4.1 Introduction

Reticulated domes can be categorized based on the arrangement of their axial members. Among these, ribbed domes are some of the oldest and most widely constructed lattice domes globally. A ribbed dome typically consists of a combination of meridional "rib" elements and horizontal "ring" elements, both of which lie on a spherical surface known as the circumsphere. The rib elements meet at the crown of the dome, while the ring elements interconnect the ribs at various horizontal levels, forming polygonal shapes. Schwedler domes share structural similarities with ribbed domes, including the presence of meridional ribs and horizontal rings. However, they distinguished by inclusion of diagonal elements that subdivide the trapezoidal sections formed by the ribs and rings. Lamella domes, another prominent type of lattice dome, are characterized primarily by their diagonal elements arranged on a spherical surface. These diagonal members create a distinctive pattern of rhombuses or diamonds, commonly referred to as "lamellas." This configuration is both structurally efficient and aesthetically appeal (Hosseinizad 2018).

Braced domes hold special significant in engineering practice. They are composed either of members lying on a surface of revolution, or straight members with their connecting points positioned on such a surface. Braced domes are typical example of 3D structure, in which any applied load is among numerous interconnected members. Braced domes can be categorized into the following types:

1. Single layer dome
2. Double layer dome (Truss type)
3. Stressed skin type
4. Formed surface type (Makowski 1962).

This chapter explains the one of a specific type of single layer dome, called as Kiewit dome which is used for numerical studies. It discusses its, dynamic properties and includes verification of dome structure.

4.2 Numerical modelling of Kiewit dome

The Kiewit dome is one of the most effective types of domes, characterized by its of cyclically symmetrical sectors braced by two sets of lamella members, each parallel to main radial ribs (Makowski 1962). As shown in Figure 4.1, a Kiewit dome divided into 8 sectors was adopted as a design example of reticulated domes as described in the past studies (Fan et al. 2005; G. B. Nie et al. 2014; F. Yang, Zhi, and Fan 2019). The reticulated dome featured 40 m-span, and 13.33 m-high. All members were made from round-HSS having diameter 120 mm and thickness 4.5 mm. These members had an initial cambering of $L/300$, a yield strength of 235 MPa, an elastic modulus of 205 GPa and coefficient for kinematic hardening of 0.01. The Giuffre-Menegotto-Pinto model, namely Steel02 in OpenSees, was used to the material's hysteretic response with kinematic and isotropic hardening parameters, as detailed in Chapter 3. As observed in the Figure 4.1 the braced dome consists with axial member of varying slenderness ratios. The diagonal and radial member exhibit slenderness ratios ranging from 50 to 60, whereas the ring member (highlighted in red) have slenderness ratios ranging from 30 to 40. According to AISC Section B 4.1 the D/t ratio for the pipe sections is 26.7, classified them as compact. Therefore, local buckling was assumed to be negligible when the axial contraction is less than from 1.0% to 2.0% times members' length. All members were assumed to have welded together thus, the joint was rigid. A uniformly distributed load of 180kg/m^2, measured per unit of the dome's triangle. To allocate this distributed load to the nodes, triangular shell elements were defined along the dome's surface in Staad.Pro. The shape functions of these shell elements were then used to determine equivalent nodal loads, as illustrated in Figure 4.2. These nodal loads were subsequently implemented in the OpenSees as concentrated nodal loads. Pinned boundary conditions at all supports were used.

The members of the dome were subdivided into eight segments and modelled using force- and displacement-based fiber elements. The force-based fiber elements utilized five integration points, while the displacement-based fiber elements used three integration points respectively using default integration schemes: Gauss-Lobatto and Gauss-Legendre rules respectively. Each fiber section has been provided with 16 fibers in circumferential direction and 4 fibers in radial direction. The following section will go through the dynamic characteristic of the dome structure followed by response spectrum definition and verification of lattice dome to elastic time history analysis.

4.3 Modal Analysis

Figure 4.3 illustrate the effective modal mass participation ratios for all the modes contributing to the structural response, achieving an effective mass participation of nearly 99% in all the three directions. In the *x*-direction, mode 1 was the dominant mode with effective mass participation ratio of 0.55 followed by mode 124, which had an effective mass participation ratio of 0.12. In the *y*-direction, modes 2 and 122 contributed with effective mass participation ratio of 0.55 and 0.12, whereas, in the vertical *z*-direction was dominated by higher modes, mode 122 having an effective mass participation ratio of 0.57, followed by the mode 186 with a ratio of 0.25.

Figure 4.4 depicts the mode shape of modes that significantly contribute to the structural response based on their effective mass participation ratios. It can be observed that for higher modes, the corresponding periods were less than 1.0 s, and a combination of many smaller modes.

Figure 4.5 illustrates the cumulative mass participation ratio, showing a total contribution of 99% in all the three directions. As describe in IASS design guidelines (IASS WG8 2019), 90% contribution in all the three directions is sufficient to capture the sufficiently accurate response. Therefore, for the subsequent numerical analysis, the first 200 modes were considered, achieving at least 90% contribution in all three directions.

4.4 Taft ground motion

The Taft ground motion was used to perform the time history response analysis (THA). For linear THA, the ground motion was scaled to 0.5g, while for nonlinear THA, it was scaled to 0.7g. The acceleration spectrum of the Taft ground motion at 0.7g was approximately 1.3 times the design response spectrum at safety level for soil type 2 defined by the Japanese building standard having a 10% probability of exceedance in 50 years over a range of the natural periods of the vibration modes. Figure 4.6 compares the Taft ground motion to the response spectrum calculated according to Japanese building standard is expressed by the following equations:

Period, s	Acceleration response spectral value, m/s^2
$T < 0.16$	$(0.64 + 6T)Z$
$0.16 < T < 0.64$	$1.6Z$
$0.64 < T$	$\left(\frac{1.024}{T}\right)Z$

Where, T is the period of the structure in seconds and Z is the seismic zone factor defined according to Japanese building standard. For the development of the spectrum, Z was taken as 1.0. The equation provides the spectral values at damage limit state. To obtain the spectral values at safe limit state, the damage state spectral values are multiplied by 5.

A response spectrum consists of three parts acceleration-sensitive, velocity-sensitive, and displacement-sensitive regions. For defining viscous damping $(F_d = c\dot{u})$, the velocity-sensitive region is where the most effect of viscous damping is most pronounced, as the damping force is proportional to the velocity of the structure (Chopra 2012). In Figure 4.6, the shaded region represents the spread of fundamental periods for the first 200 vibration modes of the dome. The vibration periods of modes up to mode 120 lies within the velocity-sensitive region or the constant acceleration region of the response spectrum, while modes above mode 120 enters the acceleration-sensitive region, where the effect of damping is less significant. To apply Damping Models 5 and 6, modes 1 and 120 were selected, respectively.

4.5 Numerical modelling in Adina

4.5.1 Material model

The material model adopted in ADINA is referred to as the Plastic Cyclic Model, which incorporates a combination of isotropic and kinematic hardening rules. This model was originally developed by Armstrong and Frederick and later enhanced by Chaboche (Lemaitre and Chaboche 1991). Based on the von Mises yield criterion, the general expression for stress and plastic strain under monotonic loading is given as:

$$\sigma = \sigma_y^0 + \frac{C_1}{\gamma_1}\left[1 - e^{-\gamma_1 \varepsilon^p}\right] + \frac{C_2}{\gamma_2}\left[1 - e^{-\gamma_2 \varepsilon^p}\right] + H\varepsilon^p \tag{4.1}$$

where, σ is the uniaxial stress, ε^p is uniaxial plastic strain, σ_y^0 is the initial yield stress, C_1, γ_1, C_2, and γ_2 are kinematic hardening parameters, and H is isotropic hardening parameter. Figure

4.7 illustrates the modification of the yield surface due to plastic deformation in principle stress space. When γ_i is set to zero, using Taylor series for $e^{-\gamma_i \varepsilon^p}$ ($e^{-\gamma_i \varepsilon^p} \approx 1 - \gamma_i \varepsilon^p + 0\gamma_i^2$), the second term simplifies to a linear term $C_i \varepsilon^p$. This allows the equation to be used for determining the monotonic plasticity parameters as described in the study (Huang and Mahin 2010). To better understand the physical implications, setting $C_2 = H = 0$ in Eq. (4.1), enables further simplification. C_1 and γ_1 can be calculated as outlined by Huang and Mahin (2010). The resulting reduced equation is illustrated in Figure 4.8. It is expressed such that the initial slope corresponds to C_1, and the saturated yield stress equal to $\sigma_y^0 + \frac{C_1}{\gamma_1}$.

$$\sigma = \sigma_y^0 + \frac{C_1}{\gamma_1}\left[1 - e^{-\gamma_1 \varepsilon^p}\right] \tag{4.2}$$

In (ADINA R & D 2021) the isotropic hardening parameter is expressed as

$$E_p = H = \frac{E E_T}{E - E_T} \tag{4.3}$$

where E_T represents the slope of stress-strain curve during plasticity, the bilinear isotropic hardening is shown in Figure 4.9. A tension coupon simulation was conducted in ADINA, with the modelling approach in

Figure 4.10. In this simulation, a single beam column element of unit length was subjected to both monotonic and cyclic loading. The calibration of parameters was carried out using a trial-and-error method, with the cross-sectional dimensions matching those used in the lattice dome. Table 4.1 represents the calibrated parameters. Figure 4.11 illustrates the resulting calibrated stress-strain curve, while Figure 4.12 compares the peak stress obtained from OpenSees and Adina over multiple cycles. As a result, the calibrated parameters for material properties in ADINA closely matched those in OpenSees, effectively replicating the development of the yield surface.

For the model of the reticulated dome constructed in ADINA, a 2-node beam element with a constant cross-section was used. The beam element employed the Newton-cotes integration scheme along the length of the element and radial direction of the pipe section, whereas composite trapezoidal rule in the tangential or circumferential direction. Specifically, 5 integration points were used along the length, while 3 integration points along the radial/thickness direction, and 8 integration points equally spaced along the circumferential direction in cross section (ADINA R & D 2021). The other conditions for the model in ADINA was identical to those in OpenSees. Initially, an eigenvalue analysis was conducted, followed by a linear time history analysis, mirroring the procedures in OpenSees. The following section presents the verification of OpenSees model against ADINA model and compares the results with findings from previous research (F. Yang, Zhi, and Fan 2019).

4.6 Verification of OpenSees modeling scheme

For the time history analysis, Damping Model 5 i.e., Rayleigh damping with initial stiffness was employed. As described earlier, the time periods of modes 1 to 120 lie in the velocity-sensitive region of the response spectrum, where the maximum effect of damping was observed. Modes 1 and 120 were used for the calculation of damping coefficients a_0 and a_1, respectively. Newmarks integration method was applied to solve the differential equations, with parameters $\gamma = 0.5$ and $\beta = 0.25$. To capture the effect of higher modes and ensure convergence, a time increment of 0.001 s was chosen based on a convergence study, which will be discussed in later chapter. The numerical analysis was conducted on a system equipped with an 11th Gen Intel(R) Core (TM) i9-11900K @ 3.5GHz processor, and 32GB of installed RAM. Figure 4.13 compares the damping ratios obtained in this study with those reported by past researchers (F. Yang, Zhi, and Fan 2019) and independently reproduced by ADINA. The first 200 modes were considered in the analysis, as the cumulative effective mass participation was almost 90% in all the three directions. For the elastic THA, Damping Models 5 and 12 were employed, as Damping Model 6 is essentially identical to Damping Model 5. Figure 4.14 shows the variation of damping ratio with the frequencies. For higher modes beyond mode 120, Damping Model 5 yields a larger damping ratio. The difference becomes particularly significant for modes with frequencies exceeding 100 rad/s, where the disparity between Damping Models 5 and 12 is substantial.

4.7 Damping ratio and coefficients

The response of a numerical model is highly dependent on the accuracy of the numerical modeling scheme adopted. As outlined in Chapter 3, the cross-section was discretized using 16 fibers along the circumferential direction and 4 fibers in the radial direction. For transient analysis, Newmark's integration scheme was employed. The first 200 modes were included in the analysis as they account for 90% of the cumulative mass participation ratio in all three directions. For Damping Models 5 and 6, modes 1 and 120 were specifically chosen, because these modes lie within the constant-acceleration region or medium-frequency range, where the effects of mass and stiffness were more prominent. For Damping Model 12, a target damping ratio of 0.02 was applied across the first 200 modes. The damping ratio was calculated using Eq. (4.4). When expressed in matrix form with two modes, the equation is further simplified as follows:

$$\begin{pmatrix} a_0 \\ a_1 \end{pmatrix} = \frac{2\omega_1\omega_{120}}{\omega_{120}^2 - \omega_1^2}\begin{pmatrix} \omega_{120} & -\omega_1 \\ \frac{-1}{\omega_{120}} & \frac{1}{\omega_1} \end{pmatrix}\begin{pmatrix} 0.02 \\ 0.02 \end{pmatrix} \tag{4.4}$$

where, a_0 and a_1 are damping coefficients, ω_1 and ω_{120} are frequencies for mode 1 and mode 120 and 0.02 is the target damping ratio, the ω_1 and ω_{120} are 20.094 and 41.84 rad/s respectively which gives the values of a_0 and a_1 as 0.543 and 0.000646 respectively.

4.8 Nonlinear-THA for A suite of 28 pairs of ground motions for near-field

The acceleration response spectrum for a suite of for near-field ground motions was selected by Table A-6C in (FEMA P695 2009), as shown in Figure 4.15. Given the natural period of mode 1, it is particularly sensitive to the near-fault earthquake ground motions. Therefore, a suite of ground motions was used as a representative sample for the study of seismic performance. Table 4.2 lists the ground motions, including components in two directions: the fault-normal and the fault-parallel. The peak ground accelerations (PGA) ranged from 5.12 m/s^2 to 12.6 m/s^2, closely matching the suite of ground motions used in the seismic risk analysis conducted by Zhi et al. (2012), which evaluated the collapse of the same reticulated dome as in this study. Table 4.3 presents the PEER NGA record information in two directions, along with fault type and site-source distance of the recording station (FEMA P695 2009).

Table 4.4 provides details of the computers used for running the nonlinear time history response analysis. The computer numbers in

Table 4.4 correspond to the labels shown in the last two columns of Table 4.2. As depicted in Figure 4.15, the suite of ground motions was adjusted to 1.3 times design basis earthquake, corresponding to a 10% probability of exceedance in 50 years, following the Building Standard Law in Japan. This design spectrum aligns with the selected ground motion in Section 4.4. The scaling ranged from 0.2 to 2.0 times the natural period. For the study of these 28 ground motions, a displacement-based fiber element formulation with 8 segments per member was used to represent the plasticity of the members in the longitudinal direction. Meanwhile, Damping Models 5, 6 and 12 were employed to examine the effects of inherent damping on the displacement response.

4.9 Conclusions

A numerical model of reticulated dome structure was successfully developed in the finite element software OpenSees, Similar model was constructed in ADINA for independent validation, after the calibration of material properties. The model was subjected to an eigenvalue analysis, the results of which indicated that Mode 1 was dominant in the horizontal x-direction, Mode 2 was dominant in the horizontal y-direction, and Mode 122 was dominant in the vertical z-direction. To achieve a cumulative effective mass participation of 99% in all three directions, contributions from 450 modes were required. However, 200 modes were sufficient to achieve 90% cumulative effective mass participation in all three directions. The reproduced response was validated against the results reported by past researcher (F. Yang, Zhi, and Fan 2019) and ADINA. The numerical model successfully captured the fundamental frequencies and damping ratios in the modes with sufficient accuracy.

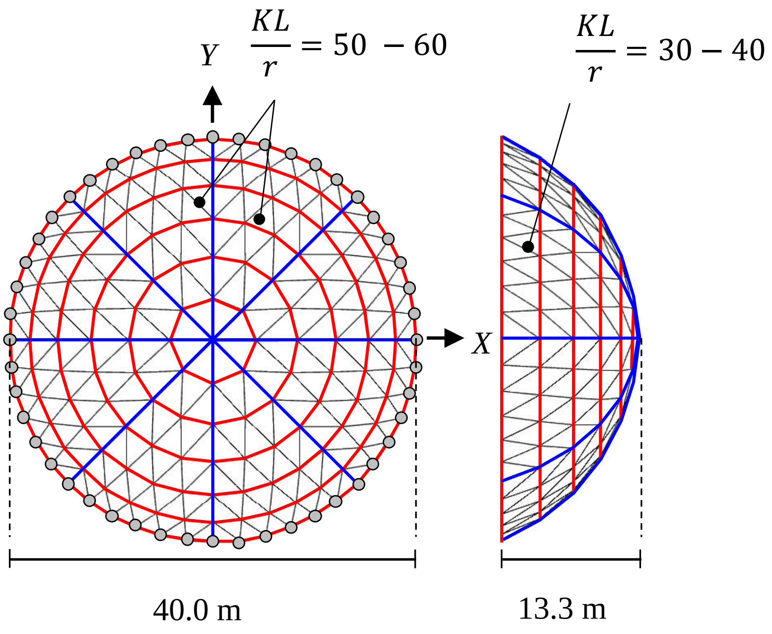

Figure 4.1 Geometrical dimensions, boundary condition, and variation of slenderness ratio of member

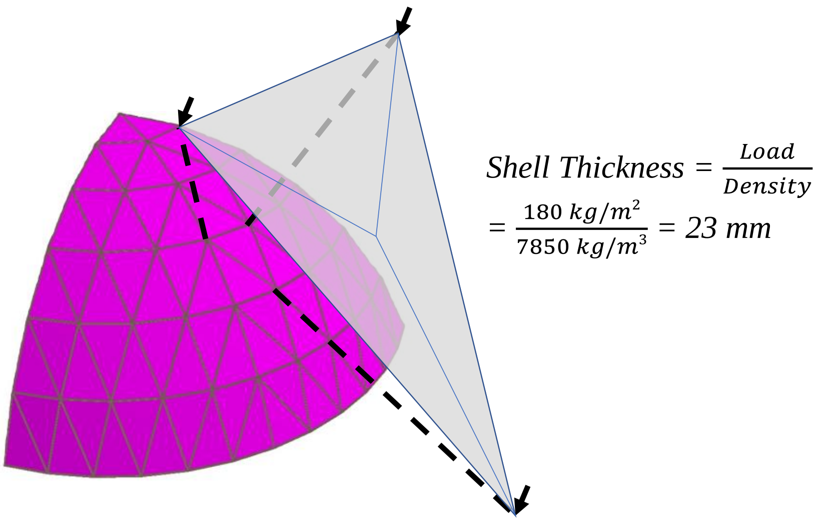

Figure 4.2 A gravity load of 180 kg/m^2 is assigned to the nodes

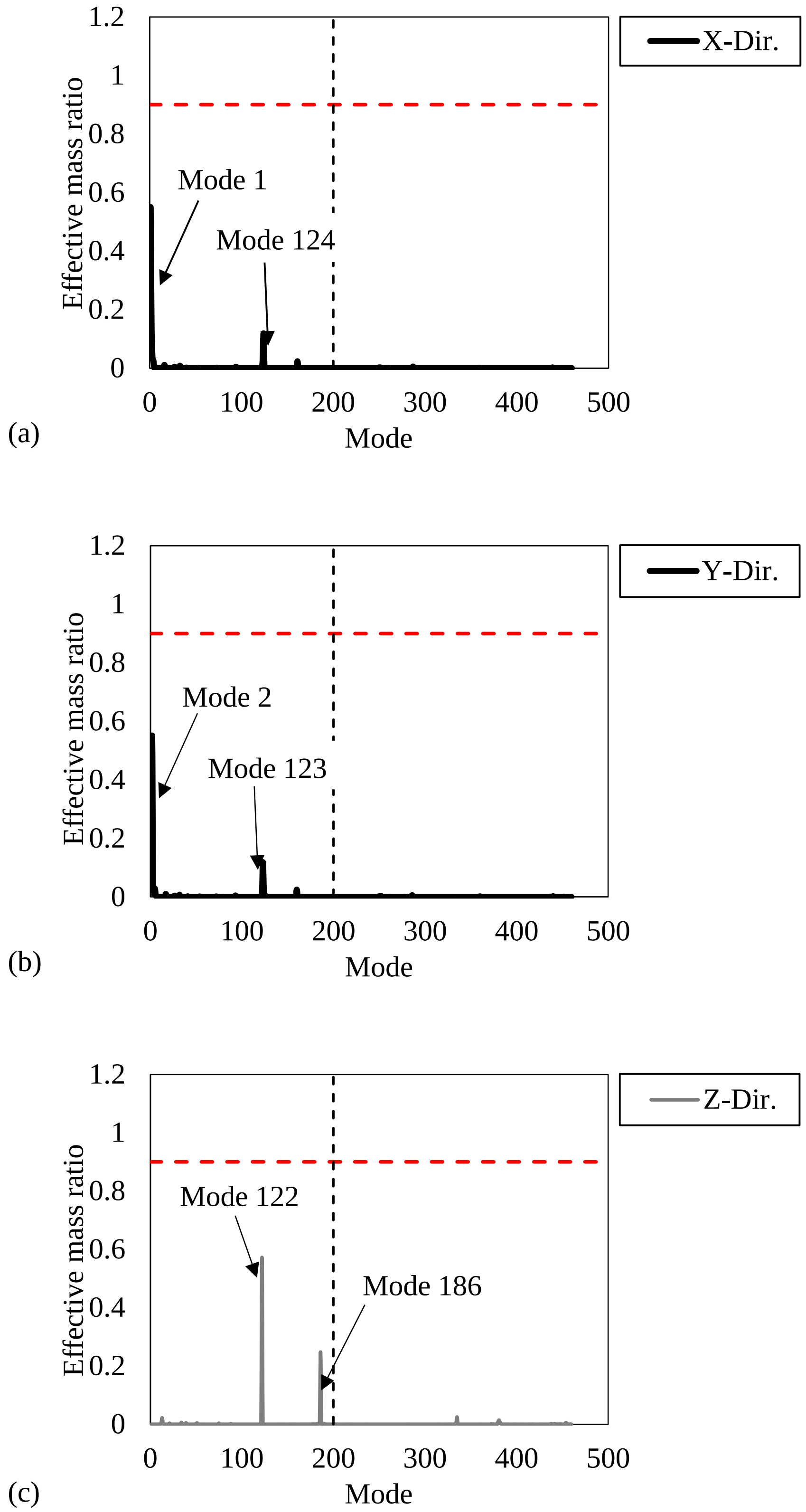

Figure 4.3 Effective modal mass participation ratio in all the three directions

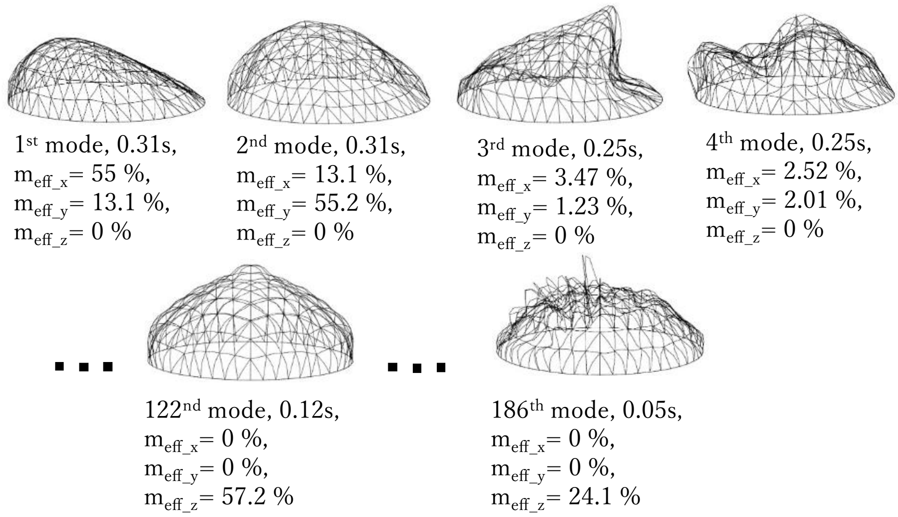

Figure 4.4 Selected Mode shapes of the reticulated dome

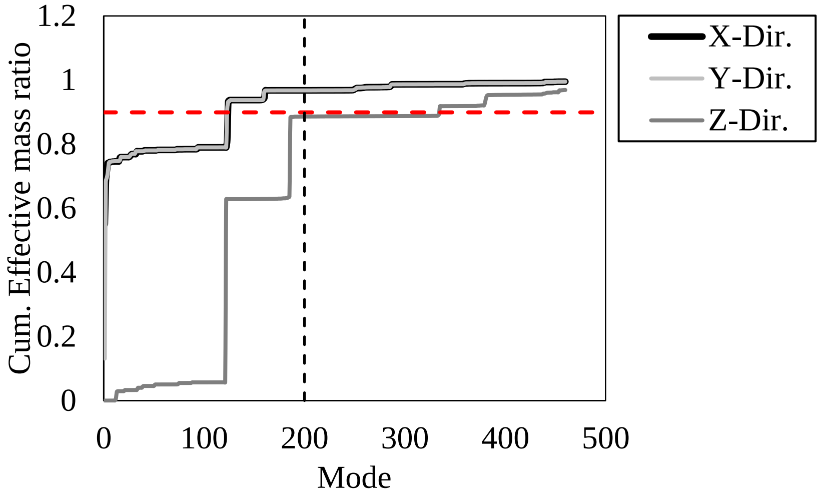

Figure 4.5 Cumulative effective mass participation of modes

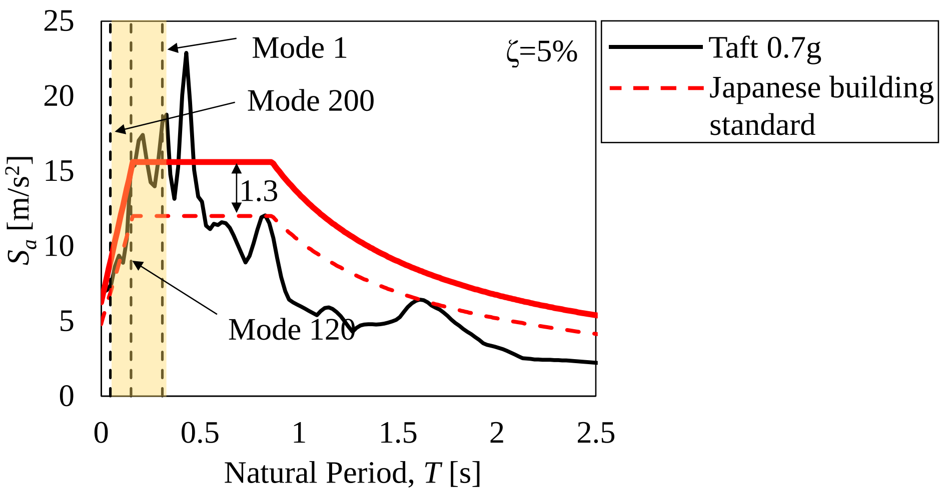

Figure 4.6 Response spectrum of Taft ground motion

(a)

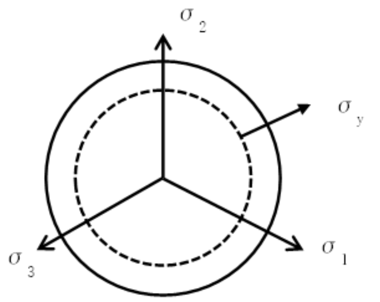

(b)

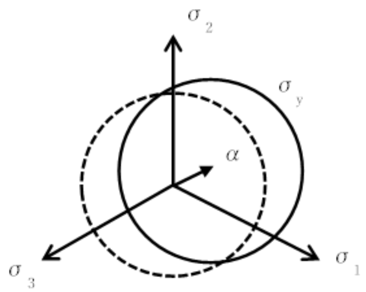

(c)

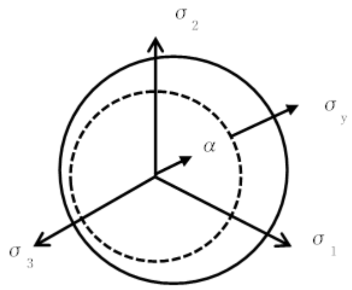

Figure 4.7 Yield surface modification with plastic deformation in principle stress space: (a) Isotropic hardening; (b) Kinematic hardening; and (c) Combined hardening (based on Broggiato, Campana, and Cortese 2008)

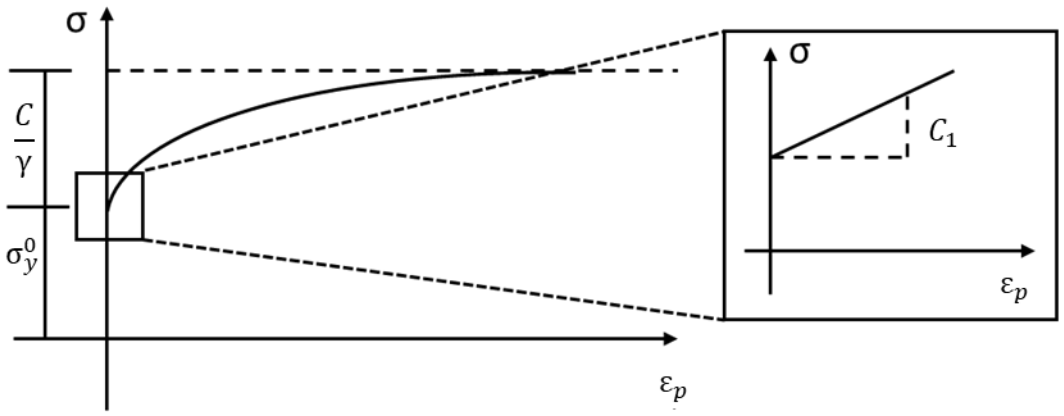

Figure 4.8 Illustration of kinematic hardening parameters (based on Huang and Mahin 2010)

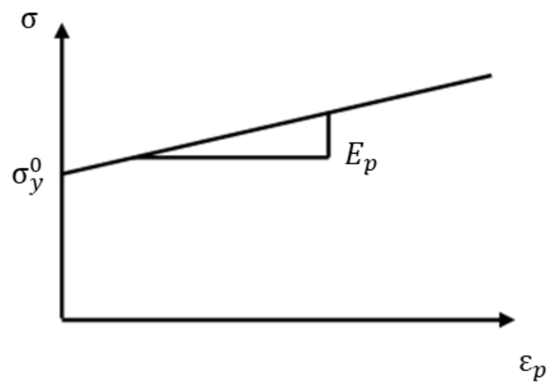

Figure 4.9 Illustration of isotropic hardening parameters (based on ADINA R & D 2021)

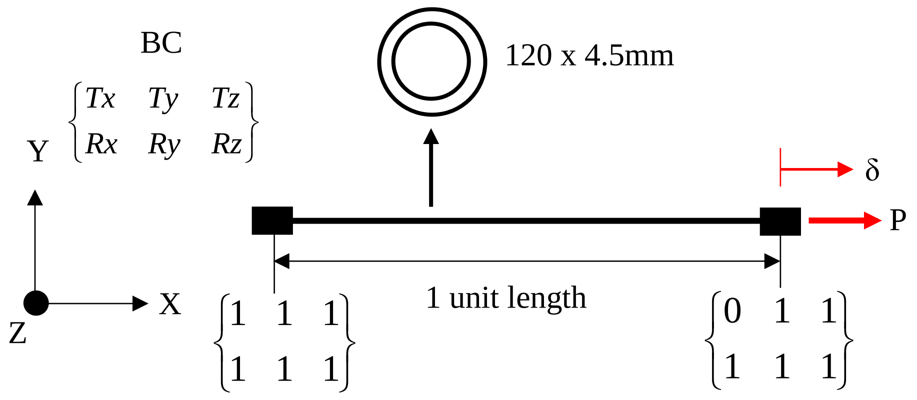

Figure 4.10 FE model for coupon simulation

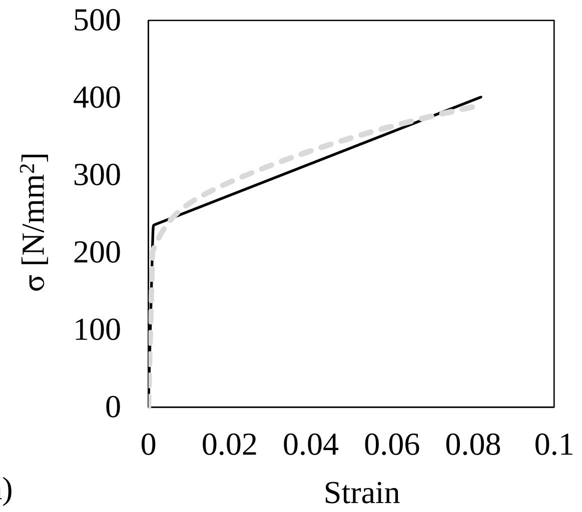

(a)

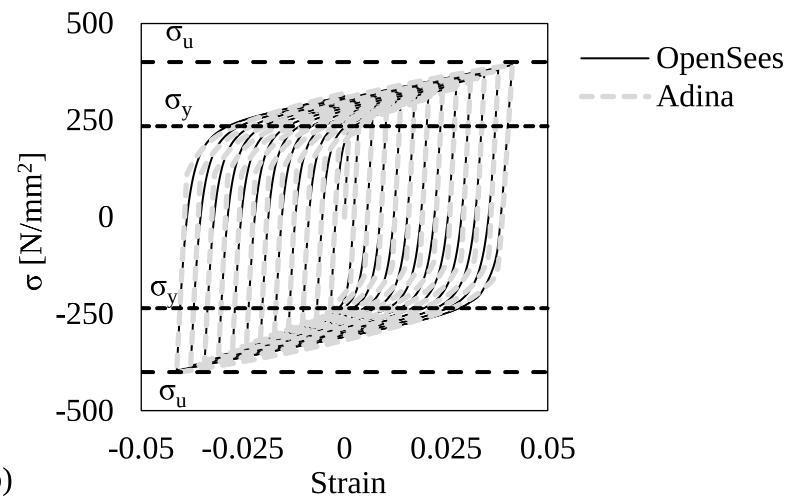

(b)

Figure 4.11 Comparison of stress strain curve (a) monotonic loading; (b) cyclic loading

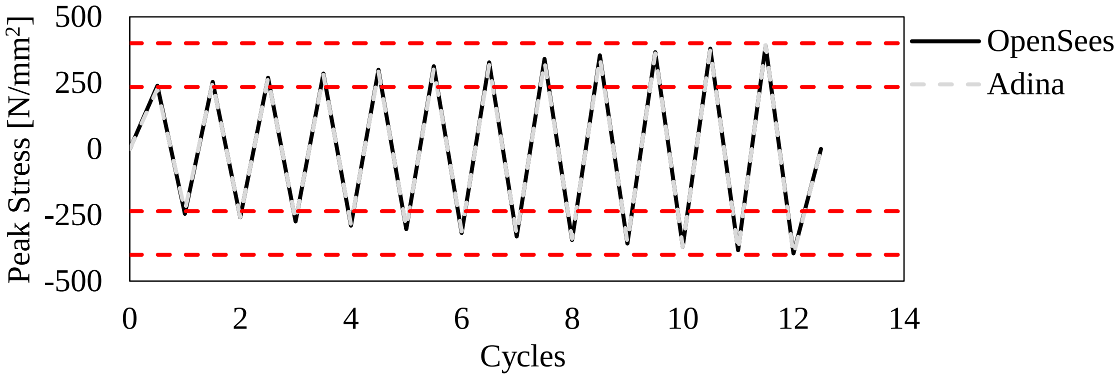

Figure 4.12 Comparison of peak stress between Adina and OpenSees

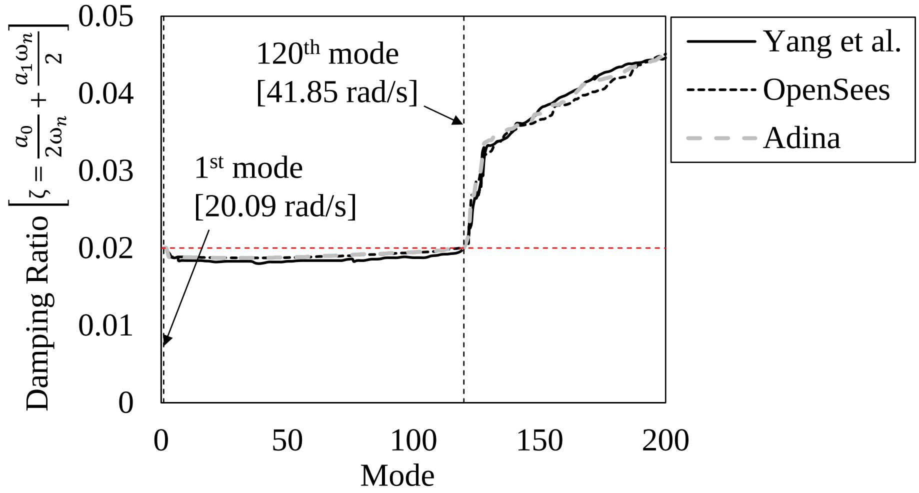

Figure 4.13 Comparison of damping ratio

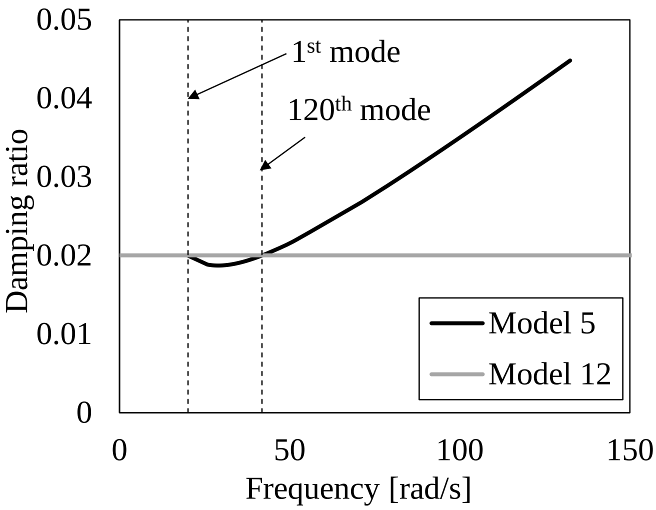

Figure 4.14 Frequency vs. damping ratio

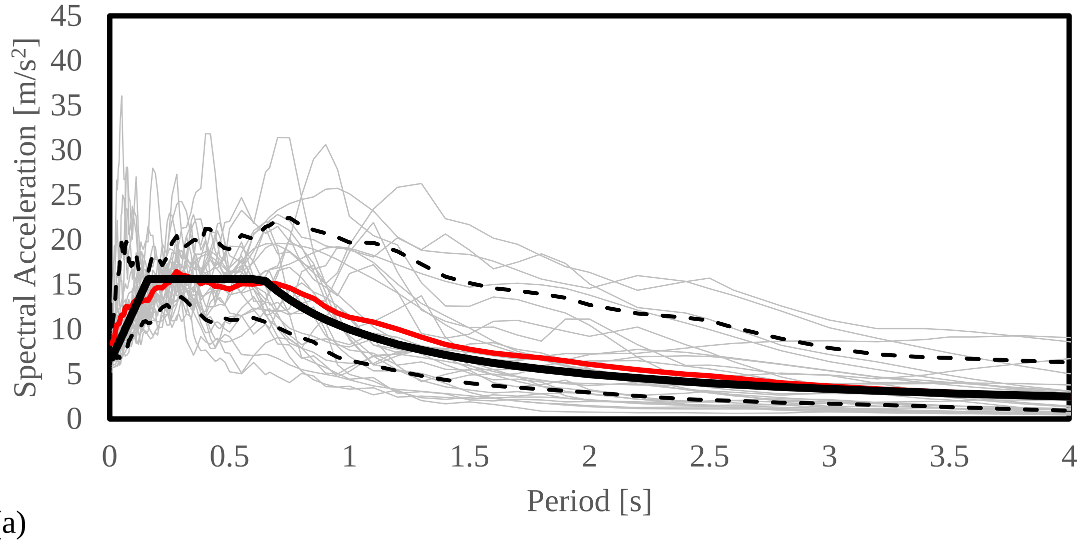

(a)

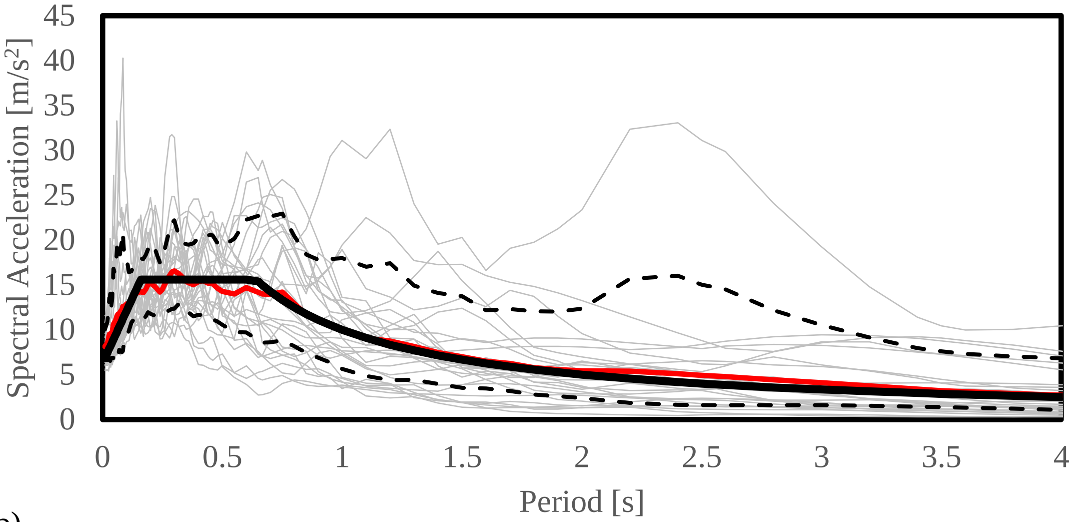

(b)

Figure 4.15 A suite of 28 pairs of ground moitions for near-field: (a) Fault-Normal; and (b) Fault-Parallel.

Table 4.1 Calibrated material parameters

OpenSees [Steel02]	Adina [Plastic cyclic]
σ_y = 235 MPa	σ_y^0 = 200.9 MPa
E = 205000 MPa, b = 0.01	E = 205000 MPa
R_0 = 25.0	E_p = 56.38 MPa
cR_1 = 0.925	C_1 = 1163209
cR_2 = 0.15	C_2 = 2814.592
a_1, a_3 = 0.0005	γ_1 = 273.47
a_2, a_4 = 0.01	γ_2 =12.46

Table 4.2 Ground motions of 28 pairs for seismic risk analysis and system used.

Case	Record Serial Number (RSN)	PGA [m/s^2]		Computer	
		FN	FP	FN	FP
1	181	8.26	8.30	1	1
2	182	9.85	9.15	1	1
3	292	5.71	6.07	1	1
4	723	8.20	8.35	2	2
5	802	9.53	6.73	2	2
6	821	8.41	7.90	2	3
7	828	8.99	8.42	2	3
8	879	8.82	10.0	2	3
9	1063	8.13	5.43	3	3
10	1086	8.69	6.97	3	3
11	1165	6.41	6.56	3	3
12	1503	11.3	9.60	2	2
13	1529	10.7	9.20	4	4
14	1605	6.89	8.39	4	4
15	126	7.19	8.79	1	1
16	160	6.94	5.96	1	1
17	165	7.40	7.71	1	1
18	495	9.81	10.4	1	1
19	496	12.6	9.20	2	1
20	741	5.12	5.41	2	2
21	753	7.24	7.97	2	2
22	825	8.76	11.3	3	3
23	1004	8.40	6.92	3	3
24	1048	5.85	6.02	3	3
25	1176	6.86	9.29	3	3
26	1504	9.17	6.33	4	4
27	1517	8.81	7.28	4	4
28	2114	8.67	10.5	4	4

Table 4.3 PEER NGA record information, fault type, and site-source distance for ground motions.

Case	Record Serial Number (RSN)	PEER NGA Record Information		Source (Fault Type)	Site-Source Distance (km)			
		FN Component	FP Component		Epicentral	Closest to Plane	Campbell	Joyner-Boore
1	181	IMPVALI/H-E06_233	IMPVALI/H-E06_323	Strike-slip	27.5	1.4	3.5	0
2	182	IMPVALI/H-E07_233	IMPVALI/H-E07_323	Strike-slip	27.6	0.6	3.6	0.6
3	292	ITALYA/STU_223	ITALYA/STU_313	Normal	30.4	10.8	10.8	6.8
4	723	SUPERSTR/B-PTS_037	SUPERSTR/B-PTS_127	Strike-slip	16	1	3.5	1
5	802	LOMAP/STG_038	LOMAP/STG_128	Strike-slip	27.2	8.5	8.5	7.6
6	821	ERZIKAN/ERZ_032	ERZIKAN/ERZ_122	Strike-slip	9	4.4	4.4	0
7	828	CAPEMEND/PET_260	CAPEMEND/PET_350	Thrust	4.5	8.2	8.2	0
8	879	LANDERS/LCN_239	LANDERS/LCN_329	Strike-slip	44	2.2	3.7	2.2
9	1063	NORTHR/RRS_032	NORTHR/RRS_122	Thrust	10.9	6.5	6.5	0
10	1086	NORTHR/SYL_032	NORTHR/SYL_122	Thrust	16.8	5.3	5.3	1.7
11	1165	KOCAELI/IYT_180	KOCAELI/IYT_270	Strike-slip	5.3	7.2	7.4	3.6
12	1503	CHICHI/TCU065_272	CHICHI/TCU065_002	Thrust	26.7	0.6	6.7	0.6
13	1529	CHICHI/TCU102_278	CHICHI/TCU102_008	Thrust	45.6	1.5	7.7	1.5
14	1605	DUZCE/DZC_172	DUZCE/DZC_262	Strike-slip	1.6	6.6	6.6	0
15	126	GAZLI/GAZ_177	GAZLI/GAZ_267	Thrust	12.8	5.5	5.5	3.9
16	160	IMPVALI/H-BCR_233	IMPVALI/H-BCR_323	Strike-slip	6.2	2.7	4	0.5
17	165	IMPVALI/H-CHL_233	IMPVALI/H-CHL_323	Strike-slip	18.9	7.3	8.4	7.3
18	495	NAHANNI/S1_070	NAHANNI/S1_160	Thrust	6.8	9.6	9.6	2.5
19	496	NAHANNI/S2_070	NAHANNI/S2_160	Thrust	6.5	4.9	4.9	0
20	741	LOMAP/BRN_038	LOMAP/BRN_128	Strike-slip	9	10.7	10.7	3.9

21	753	LOMAP/CLS_038	LOMAP/CLS_128	Strike-slip	7.2	3.9	3.9	0.2
22	825	CAPEMEND/CPM_260	CAPEMEND/CPM_350	Thrust	10.4	7	7	0
23	1004	NORTHR/0637_032	NORTHR/0637_122	Thrust	8.5	8.4	8.4	0
24	1048	NORTHR/STC_032	NORTHR/STC_122	Thrust	3.4	12.1	12.1	0
25	1176	KOCAELI/YPT_180	KOCAELI/YPT_270	Strike-slip	19.3	4.8	5.3	1.4
26	1504	CHICHI/TCU067_285	CHICHI/TCU067_015	Thrust	28.7	0.6	6.5	0.6
27	1517	CHICHI/TCU084_271	CHICHI/TCU084_001	Thrust	8.9	11.2	11.2	0
28	2114	DENALI/ps10_199	DENALI/ps10_289	Strike-slip	7	8.9	8.9	0

Table 4.4 Assigned computers

No.	CPU Processor	Memory of RAM
1	10th Gen Intel@ CoreTM i9-10900X @ 3.7 GHz	32 GB
2	AMD RyzenTM 7 5800X @ 3.8 GHz	16 GB
3	11th Gen Intel@ CoreTM i9-11900X @ 3.5 GHz	32 GB
4	9th Gen Intel@ CoreTM i9-9900K @ 3.6 GHz	64 GB

5 RESPONSE OF THE DOME SUBJECTED TO TAFT GROUND MOTION

5.1 Introduction

This chapter discusses the response of the reticulated dome subjected to two patterns of scaled Taft ground motions: one of in which the dome remained in an elastic state, and the other in which it underwent inelastic behavior. To carry out elastic time history analysis, the Taft ground motion, scaled to 0.5g, was applied in horizontal *x*-direction with the plasticity disabled by setting a higher yield strength for the members. In the elastic analysis, both formulations—force-based and displacement-based fiber formulations—were identical. Two damping models were employed to study their effect on the fundamental characteristic of the dome, including peak displacement response, base shear, and drift (horizontal displacement at the apex). To examine the inelastic response, the dome was subjected to the Taft ground motion scaled to 0.7g in horizontal *x*-direction. The impact of element formulations and damping models was investigated. Additionally, a representative damping ratio, introduced by the study (Fukutomi et al. 2020), was applied to study its effect on various parameters in the nonlinear range.

5.2 Elastic response

Figure 5.1(b), (c), and (d) show a comparison of peak displacement responses recorded at the locations indicated in Figure 5.1(a). It can be observed that the ADINA model reproduced an identical response in horizontal *x*- and vertical *z*-direction, but slightly underestimated the response in horizontal *y*-direction.

Figure 5.2 illustrates the base shear experience by the reticulated dome under seismic excitation, with a maximum magnitude of 3,722 kN. Both damping models produced identical results.

Figure 5.4 and Figure 5.4 presents the peak displacement response for Damping Model 5 and 12. As shown, both the element formulations and damping models produced similar results. The absolute peak displacements in the *x*-, *y*-, and *z*-directions were 40 mm, 13 mm, and 34 mm, respectively.

A similar trend was observed in the drift, here drift is considered as the horizontal displacement in x-direction observed at the apex response comparison, shown in Figure 5.5.

In conclusion, an elastic time-history analysis of the reticulated dome was performed using the Taft ground motion scaled to 0.5g, with plasticity effects disabled. Both the OpenSees and ADINA models produced comparable responses in the elastic state, confirming that the numerical modeling scheme applied in OpenSees is reasonably accurate and suitable for further analysis. Therefore, OpenSees was used for subsequent analyses. A comparison of peak displacement, base shear, and drift was conducted for both formulations and various damping models. The results show that both element formulations and damping models yielded consistent and identical responses.

5.3 Elastic-plastic response

5.3.1 Selected time increment

Selecting an appropriate time increment is crucial for achieving convergence in numerical analysis, while ensuring sufficient accuracy and avoiding excessive computational demands. Figure 5.6 illustrates the peak displacement response for the displacement-based formulation in both horizontal and vertical directions. The maximum time increment that allowed the dome model with 8 segments per member, using both formulations to converge successfully was 0.0025 s.

Figure 5.7 presents the peak displacement response for the force-based fiber element. When a time increment of 0.0025 s was applied in the transient analysis, the force-based formulation encountered convergence errors and could not complete the analysis. To address these issues, the HHT (Hilber-Hughes-Taylor) integration scheme was employed instead of Newmark’s integration scheme. The HHT method introduces artificial numerical damping, determined by the chosen α parameter, which helped stabilize the analysis at 0.0025-s time increment, resulting in a damped response in the vertical direction.

A time increment of 0.001 s was chosen for the following nonlinear analysis in this section. This increment ensures that the accurate capture of higher modes (fundamental period of mode 200 was 0.045 s) and allows for the continued use of Newmark’s integration scheme across both formulations.

5.3.2 Number of Segments per member

Depending on the type of element formulation, the number of segments used per member can significantly affect the transient response. For plastic state, Damping Model 6 was used to compare the outcomes across different element formulations—both force-based and displacement-based—where each joint-to-joint distance of the individual members evenly divided into 2, 4, 8, and 10 segments.

Figure 5.8 illustrates contours plotted at the instant when the peak vertical displacement was observed for force-based formulation. Solid black lines indicate areas with the positive vertical displacements, while areas with dotted lines show the distribution of negative vertical displacements. The force-based fiber elements with 2, 4, 8, and 10 segments produced a similar distribution of vertical displacement across the dome. For the force-based fiber elements, the peak vertical displacement for 2, 8, and 10 segments differed by up to 14%. The model using 4-segment elements showed a peak value 33% lower than that of the 10-segment elements, highlighting the sensitivity of the results to choice of segment number. In contrast to the force-based fiber elements, the models using displacement-based fiber elements with 2 and 4 segments displayed an asymmetrical distribution of vertical deformation along the NS direction, as shown in Figure 5.9 (a) and (b). However, this asymmetry was not observed in the models with 8 and 10 segments, as depicted in Figure 5.9 (c) and (d).

The peak displacement predicted by the displacement-based fiber elements with 2 or 4 segments was 2.4 times lower than that predicted by the 8-segment and 10-segment models. As noted by the study (Neuenhofer and Filippou 1997), the accuracy of the model using displacement-based fiber elements improved as the number of segments increased. Peak displacements computed using the displacement-based fiber elements with 8 and 10 segments occurred at the same node, with the difference between these displacements being within 1%. The distribution of vertical displacement was similar, indicating that convergence had been achieved. To ensure computational efficiency while maintaining model accuracy, a minimum of 8 segments was deemed sufficient for numerical modeling.

Therefore, a force-based fiber element with 2 segments may offer reasonable resolution for nodal displacement response, i.e., the global response. For the displacement-based fiber element, segmenting into 8 segments is recommended for accurately capture both the global system and component-level responses. For simplicity, the force-based fiber element with 2 segments was superior to the displacement-based fiber element with 8 segments in terms of computational time, while still capturing a reasonable global response.

Table 5.1 summarizes the peak vertical displacement and the computational time for each model. The models using displacement formulation across all four patterns demonstrated shorter computational times compared to those using the force-based formulation. This is due to the force-based formulation, where equilibrium between element basic forces and section forces, as well as compatibility between element deformations and section deformations, must be satisfied at every integration point within a segment. Increasing the number of integration points per segment for same discretization scheme results in longer computational times.

Figure 5.10 and Figure 5.11 illustrate the distribution of vertical deformation for various damping models with 8 segments per member along the ridge AOA'. An asymmetrical distribution of vertical deformation about the NS direction was only observed for Damping Model 5, while Damping Models 12 and 6 displayed relatively symmetrical distributions. For force-based formulation, the choice of damping model influenced the distribution of deformation. In contrast, the models using displacement-based fiber elements produced asymmetric vertical distribution for all damping models about the NS direction.

In conclusion the figures suggest that damping models can influence the deformation pattern. This highlights the importance of selecting an appropriate formulation based on the structural behavior and desired accuracy of the results. Which is further discussed in coming sections.

5.4 Equivalent damping ratio

To enable a comparative study on damping ratios for inelastic state, the concept of the representative damping ratio, as proposed by Fukutomi et al. (2020), was utilized. Calculating the representative damping ratio requires introducing the concept of the equivalent damping ratio.

When a structural system transitions into the inelastic state, its stiffness changes due to nonlinear behavior, resulting in a shift in the frequencies of its contributing modes. The equivalent damping ratio represents the damping ratio assigned to each contributing mode, accounting for the inelasticity experienced by the structural system. This approach provides a more realistic representation of energy dissipation in systems undergoing nonlinear deformations. The equivalent damping ratio $\zeta_{n,eq}$ for each mode is calculated as follows:

$$\zeta_{n,eq} = \frac{\{\phi_n^*\}^T[c]\{\phi_n^*\}}{2 \cdot \omega_n{}^* \cdot \{\phi_n^*\}^T[m]\{\phi_n^*\}} \tag{5.1}$$

$$\gamma_n{}^* = \frac{M_n{}^*}{\sum_{n=1}^{N} M_n} \tag{5.2}$$

$$M_n{}^* = (\Gamma_n{}^*)^2 \cdot M_n \tag{5.3}$$

In the above equations, $\omega_n{}^*$ is the frequency of elastic-plastic system updated step by step, $\gamma_n{}^*$ is the ratio of effective modal mass to total mass, $M_n{}^*$ is the effective modal mass, and Γ_n is the modal participation factor.

Figure 5.12 (a) illustrates an example of the equivalent damping provided by each damping model for an inelastic state of the dome, calculated for the displacement-based fiber element with 8 segments at 15 s when peak vertical deformation was observed for Damping Model 12. For Damping Model 5, the equivalent damping ratios in plastic state deviate from those in elastic state, ranging from -5.5% to 30% across the corresponding modes. This discrepancy arose from Damping Model 5's inability to maintain proportionality in the elastic-plastic system, similar response was observed when first 460 modes were checked, as illustrated in Figure 5.12 (b) in which substantial increase in Equivalent damping ratio was observed for the modes above 230, however when effective mass contribution of this modes were negligible as illustrated in Figure 4.3. For Damping Model 6, although the equivalent damping ratio aligned with the initial-stiffness-proportional Rayleigh curve used in Damping Model 5 in elastic state, different damping ratios were observed for the updated frequencies due to a decrease in frequencies compared to elastic state. In plastic state, Damping Model 5 exhibited equivalent damping ratios that were 0.94 to 1.46 times higher than those of Damping Model 6. For Damping Model 12, the equivalent damping ratio retained at the initial value of 0.02 up to mode 460, where the cumulative mass participation reached 99% for all three directions. The first 200 modes were utilized to retain the damping ratio, which contributed to reduce computational time.

5.5 Representative damping ratio

A representative damping ratio ζ_{rep} is calculated as per Eq. (5.4)

$$\zeta_{rep} = \sum_{n=1}^{N} \zeta_{n,eq} \cdot \gamma_n{}^* \tag{5.4}$$

In the above equation, $\zeta_{n,eq}$ is the equivalent damping ratio, calculated as Eq. (5.1) and $\gamma_n{}^*$ is the effective modal mass ratio, where N = 200 is the number of modes considered

5.5.1 Force – based formulation

Figure 5.13 - Figure 5.15 illustrate calculation of representative damping ratio for models with fiber-based element formulation for 1.0 s interval between 15 s and 16 s. This duration corresponds to the time when the maximum displacement at a node was observed for Damping Model 12 with the displacement-based fiber element. Note that the equivalent damping ratio corresponds to a particular mode and thus exhibit directionality. The values reflect the overall damping behavior of the system. For better clarity, the equivalent damping ratio for modes contributing more than 5% of the effective mass the in *x*-, *y*-, *z*- direction is illustrated across all directions. This facilitates a clearer understanding of the representative damping ratio. Table 5.3 lists equivalent damping ratio for the selected modes.

For Damping Model 5, the maximum contribution was observed as follows: mode 1 in the horizontal *x*–direction, modes 2 and 3 in horizontal *y*-direction, and mode 122 in the vertical *z*-direction. The average equivalent damping ratio over the time for mode 1 and mode 2 was higher by 50%. whereas maximum damping observed was 0.067 for both the modes. The average representative damping ratios observed were 0.03, 0.025, and 0.027 in *x*-, *y*-, and *z*–direction, respectively. The average of representative damping across all three directions was 0.027, which was 37% higher than the target damping ratio of 0.02.

For Damping Model 6, the maximum contributions were observed as follows: modes 1, 2 and 3 in horizontal *x*-direction, modes 2, 3, and 4 in the horizontal *y*-direction, and mode 122 in vertical *z*-direction. 5. The average equivalent damping ratio over the time for mode 1 and mode 2 was higher by 20%. whereas the maximum damping ratio observed was 0.039 and 0.023 respectively. The average representative damping ratios observed were 0.021, 0.021, and

0.023 in the *x*-, *y*-, and *z*–directions, respectively. The average of representative damping in all three directions was 0.021, which is 7.5 % higher than the target damping ratio of 0.02.

For Damping Model 12, the maximum contributions were as follows: mode 1 in the horizontal x-direction, mode 2 in the y-direction, and mode 122 in z direction. 3. The average equivalent damping ratio over the time for mode 1 and mode 2 was 0.02. whereas the maximum damping ratio observed was 0.024 and 0.021 respectively. The average representative damping ratios observed were 0.02, 0.02, and 0.018 in x-, y-, and z–direction respectively. The average of representative damping in all three direction was 0.019, 5 % lower than the target damping ratio of 0.02.

5.5.2 Displacement – based formulation

Figure 5.16 - Figure 5.18 illustrate the calculation of representative damping ratio for models with displacement-based fiber element formulation. Table 5.4 lists equivalent damping ratio for the selected modes.

For Damping Model 5, the maximum contribution was observed as follows: mode 1 in the horizontal *x*-direction, mode 2 in the horizontal *y*-direction, and mode 122 in the vertical *z*-direction. 3. The average equivalent damping ratio over the time for mode 1 and mode 2 was higher by 35% and 5%. whereas the maximum damping ratio observed was 0.056 and 0.057 respectively. The average representative damping ratios observed was 0.026, 0.023, and 0.026 in the *x*-, *y*-, and *z*–directions, respectively. The overall average representative damping ratio across all three directions was 0.025, which is 26 % higher than the target damping ratio of 0.02.

For Damping Model 6, the maximum contribution was observed as follows: modes 1, 2, 3, 4 and 5 in the horizontal *x*-direction, modes 3, 4, 5, and 6 in the horizontal *y*-direction, and mode 122 in vertical *z*-direction. 7. The average equivalent damping ratio over the time for mode 1 and mode 2 was higher by 20%. whereas the maximum damping ratio observed was 0.032 and 0.028 respectively. The average representative damping ratios over the time range were 0.021, 0.021, and 0.022 in the *x*-, *y*-, and *z*–directions, respectively. The overall average representative damping ratio across all three-direction was 0.021, which is 7.5% higher than the target damping ratio.

For Damping Model 12, the maximum contribution was observed as follows: modes 1, 2, 3 and 4 in the horizontal *x* – direction, modes 2, 3, 4 and 6 in the horizontal *y*-direction, and mode 122 in the horizontal *z*-direction. 3. The average equivalent damping ratio over the time for mode 1 and mode 2 was 0.02. whereas the maximum eq. damping ratio observed was 0.043 and 0.026 respectively. The average representative damping ratios observed were 0.02, 0.02, and 0.018 in the *x*-, *y*-, and *z*–directions, respectively. The overall average representative damping ratio across all three-direction observed in the system was 0.019, 5% lower than the target damping ratio.

For both formulations, the representative damping ratio in inelastic state in Damping Model 5 was the largest among all damping models in all three directions. The mean representative damping ratios for all directions in Damping Model 5 were 1.37 times the target value of 0.02 for the force-based formulation and 1.26 times the target value for the displacement-based formulation. In contrast, the mean representative damping ratios in all directions for Damping Models 6 and 12 were 1.08 times and 0.95 times the target value of 0.02, respectively, for both formulations. The influence of higher damping ratios on the fundamental characteristics was discussed further in the following sections.

5.6 Effect on deformation and frequency

This section discusses the effect of different damping models and element formulations on the vertical deformation and modal frequency when the reticulated dome structure was at an instant in inelastic state. Figure 5.19 - Figure 5.20 illustrates the vertical deformation at the apex of the reticulated dome structure, for force-based and displacement-based fiber element, respectively. The dome remained in elastic state until 9.5 s, after which residual deformation was observed. Both the formulations produced identical response at the apex. However, Damping Model 5 underestimated the residual displacement by nearly 50% compared to Damping Models 6 and 12.

Figure 5.21 - Figure 5.22 illustrate the effect on frequency throughout the transient analysis. Due to high computational costs, the data was extracted at the time increments of 4 s. Since modes 1 and 120 were used to define the damping coefficients, these modes were considered for analysing the frequency effect. A general trend of frequency decrease over the time was observed for all three damping models in both element formulations. Damping Model

5 exhibited the smallest decrease in frequency compared to Damping Models 6 and 12, due to its higher representative damping ratio. Nanhai and Jihong (2014) performed shake table tests on three Kiewitt-6 single-layer reticulated dome scale models. The prototype for these models had a span of 75 meters and a rise-to-span ratio of 0.5, with a geometric similarity ratio of 1:10 maintained between the models and the prototype. To ensure maximum mechanical similarity, the number of nodes and members in the prototype was not simplified, meaning the topological configuration remained consistent across both the test models and the prototype. Additionally, mass, load, stiffness, boundary conditions, and initial conditions were matched to ensure equivalence. Based on their sweep frequency tests, The Authors observed a decrease in fundamental frequency with increasing PGA, indicating a gradual reduction in structural stiffness aligning well with the numerical response observed.

However, in the simulated results no significant effect on higher modes was observed. Mode 1, the dominant mode in the horizontal *x*-direction based on mass participation ratio, showed the most significant impact. These results suggest that damping models and element formulations affect the dynamic response of the dominant mode, which plays a more substantial role in the global structural response.

5.7 Distribution of vertical deformation on the surface of dome

Figure 5.23 illustrates the contour of vertical displacement at an instant when the peak displacement at a node was observed. It is important to note that the timing of the peak displacement varied depending on the damping model and types of element formulation used. The peak displacement was concentrated at Ring number 2 from the supports.

In the force-based fiber element formulation, Damping Models 5 and 12 exhibited similar symmetrical distributions of vertical deformations about the EW direction, with a peak close to 55 mm, while Damping Model 6 showed a higher peak deformation close to 115 mm, along with negative displacements concentrated in the central zone. In the displacement-based fiber element formulation, Damping Model 5 had the lowest peak displacement (close to 55 mm) and showed asymmetry along the NS direction. Damping Models 6 and 12 displayed peak deformations (close to 115 mm), with Damping Model 6 also displaying a central negative displacement.

Although Damping Model 12 exhibited minimal sensitivity to element formulation in terms of deformation distribution patterns, the difference in peak displacement between the force-based and displacement-based formulations was significant. This discrepancy highlights the importance of carefully evaluating the choice of element formulation when analyzing peak responses. While the deformation contours remain relatively consistent, the marked difference in peak values can significantly impact overall structural performance predictions, particularly under critical loading conditions.

Table 5.2 presents the computational time required by both element formulations for each damping model. Among the models, Damping Model 5 required the least computational time. In Damping Model 6, the damping matrix is assembled at each time step based on the updated stiffness of the structure. As a result, the computational time required by Damping Model 6 is approximately 1.6 times that of Damping Model 5.

In the Newmark's integration method, the residual and tangent stiffness (effective stiffness) is given by Eq. (5.5)-(5.6) for time step *i* and iteration j, were $\{R\}$ is the residual force, $\{p\}$ is external force $\{f_s\}$ is restoring force vector, $[c]$ is damping matrix and $[m]$ is the mass matrix. Vectors $\{u\}$, $\{v\}$, and $\{a\}$ represents the displacement, velocity and acceleration respectively.

$$\{R_{i+1}^j\} = \{p_{i+1}\} - \{f_{s,i+1}^j\} - [c]\{v_{i+1}^j\} - [m]\{a_{i+1}^j\} \tag{5.5}$$

$$[\hat{k}_{T,i+1}^j] = [k_{T,i+1}] + \frac{[m]}{\beta \Delta t^2} + \frac{\gamma [c^*]}{\beta \Delta t} \tag{5.6}$$

$$[\hat{k}_{T,i+1}^j]\{\Delta u\} = \{R_{i+1}^j\} \tag{5.7}$$

The modal damping matrix assembled in OpenSees is fully populated given by $[c]$. OpenSees assembles the dynamic tangent (effective stiffness matrix $[\hat{k}_T]$) into the matrix storage scheme using the 'system' command. However, since the modal damping matrix is fully populated, even when the matrix storage, is banded (BandGeneral), some terms in the dynamic tangent matrix will be zero despite being non-zero in the original modal damping matrix $[c]$. This results in an approximate modal damping matrix, $[c^*]$, which is a subset of $[c]$ (Chopra and Mckenna, 2016). Due to this approximation, convergence issues arise because the dynamic tangent becomes inconsistent with the residual matrix given by Eq. (5.7). As a result, the analyses do not converge in single iteration, requiring additional iterations within a single timestep, leading to increased computational time. Additionally, the memory requirement to store the eigenvectors- each having a size equal to degree of freedom of the structure for *n* modes resulted, increases computational time. This may be particularly problematic for large structures, such as a dome with a high number of degree of freedoms, where the contribution of higher modes is substantial. Because of this Damping Model 12 required nearly 3 times as much as Model 5. The results show that the computational time between both element formulations was competitive, thus limiting the potential advantage of using finer subdivisions in the force-based fiber element.

5.8 Member level response

Figure 5.24 shows the maximum elongation (represented by white circles) and contraction (represented by black circles, with δ/L expressed as a percentage) experienced by the members throughout the excitation duration, comparing the results from the force-based and displacement-based fiber elements. For Damping Model 5, the simulated maximum elongation of members was nearly identical when using the force-based and displacement-based elements. For Damping Models 6 and 12, the contraction of members with the displacement-based fiber element was 1.2 to 2.0 times greater than that with the force-based fiber element. This trend was observed only in the diagonal members at the location where the maximum vertical displacement response occurred. The primary cause of this difference was the force equilibrium at the nodes in the force-based element formulation, where forces are redistributed once the member experiences residual deformation. This effect is less pronounced in the displacement-based fiber element.

The effect of axial deformation was also evident in the member hysteresis response shown in Figure 5.25 for one of the members that experienced the maximum axial deformation. The elongation-to-contraction ratio and hysteretic dissipation energy observed with Damping Model 5 were nearly half of those observed with Damping Models 6 and 12. In general, the elongation and contraction of steel braces were closely correlated with the story drift in multi-story braced frames. This suggests that the members in the reticulated dome experienced less inelastic deformation compared to the story drift of 1% in multi-story braced frames.

5.9 Failure pattern of members of dome

Figure 5.26 provides an overview of members that experienced buckling, tensile yielding, as well as their maximum elongation and contraction. The number of members that experienced buckling was greater than the number that experienced tensile yielding. These occurrences were primary concentrated in the vicinity of the supports in predominantly symmetry in the NS direction about the EW direction. Buckling was mainly observed in the diagonal members that connect the ring members to the radial members. The number of members that experienced tensile yielding remained similar across all damping models.

5.10 Conclusions

This chapter presents a numerical study on the dynamic response of a spherical reticulated dome with a 40-m span and 13-m high, representing a benchmark model for evaluating the seismic performance of spatial structures. The study validated the applicability of beam-column fiber elements formulated based on force or displacement, with segmentations of 2, 4, 8, 10, or 30 segments, for axially-loaded members of the reticulated dome. The open-source analysis platform OpenSees was utilized to investigate the effect of element formulations and damping models on the vibration displacement response of the dome. The structure was subjected to the Taft ground motion scaled to 1.3 times the design spectrum, corresponding to a 10% probability of exceedance in 50 years. The findings and conclusions are summarized as follows:

1. Regardless of the number of segments or the choice of damping models, numerical models using force-based and displacement-based fiber elements consistently predicted identical elastic dynamic responses of the reticulated dome in OpenSees.

2. The choice of force formulations, damping models and the number of segments significantly influenced the elastic-plastic response of the reticulated dome, even though the system's plasticity was not extensive. This differs with the findings of the study (Chopra and Mckenna 2016), which suggested that the influence of damping models on dynamic responses in the multi-story frames was limited for the distributed plasticity models.

3. A force-based fiber element with 2 segments may offer reasonable resolution for nodal displacement response, i.e., the global response. Specifically, the displacement-based fiber element with 8 segments is recommended for reliably estimating both global system and component-level responses in dome structures, while balancing computational efficiency. For simplicity, the force-based fiber element with 2 segments was superior to the displacement-based fiber element with 8 segments in terms of computational time, while still capturing a reasonable global response.

4. The average representative damping ratios across all three directions for Rayleigh model with initial stiffness were 1.26 times the target damping ratio, whereas those for Rayleigh damping with tangent stiffness and modal damping were nearly identical with the target. Displacement response computed with Rayleigh model based on tangent stiffness tends to show 1.1 to 1.2 times higher than those by modal-damping model based on the study of a suite of ground motions. Consequently, modal-damping model emerged as the most reliable choice among the selected damping models, as it retained consistent damping ratios for higher modes while accurately representing the degradation of the reticulated dome structure.

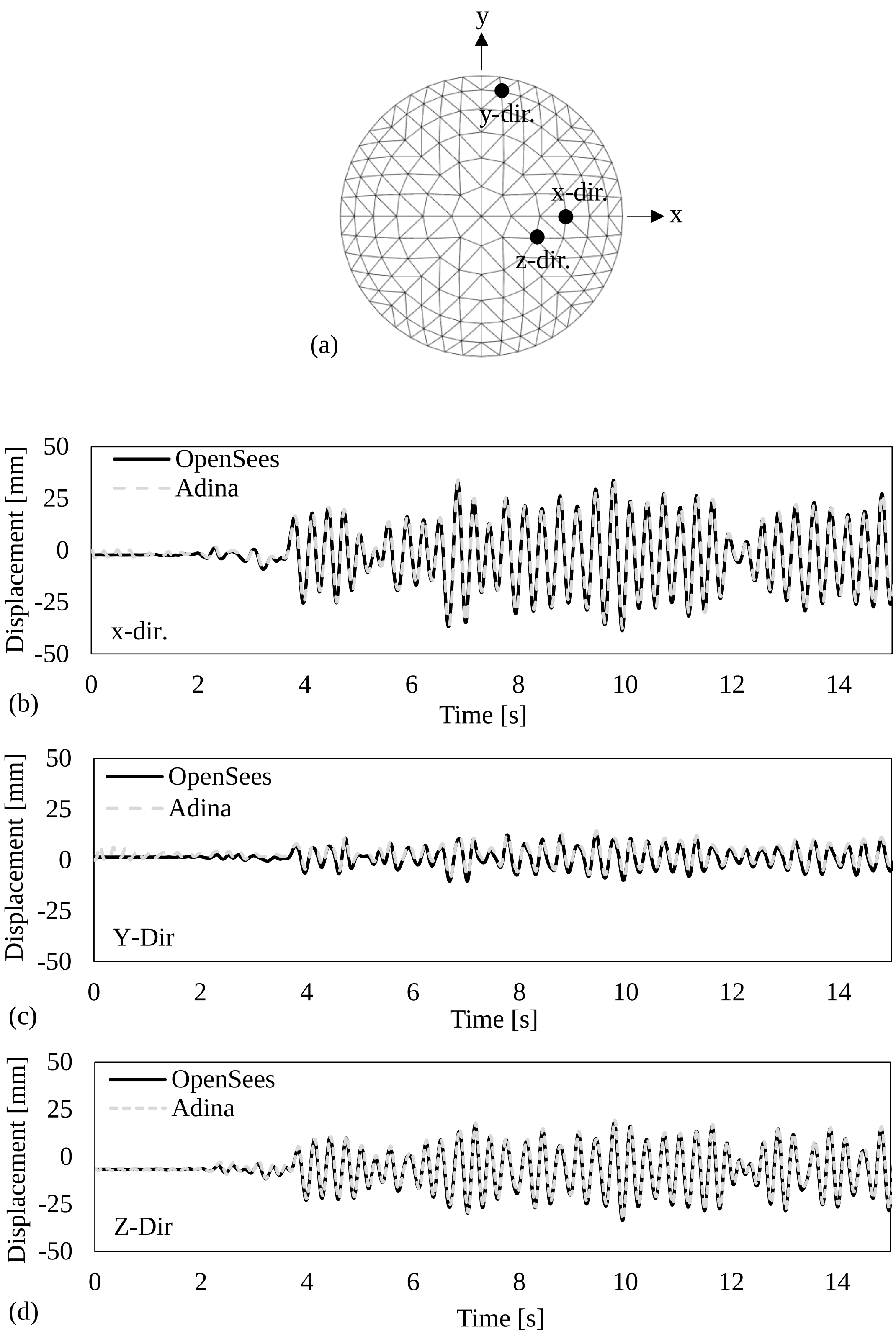

Figure 5.1 Comparison of peak displacement (a) location of measurement; (b) x-dir.; (c) y-dir.;(d) z-dir.

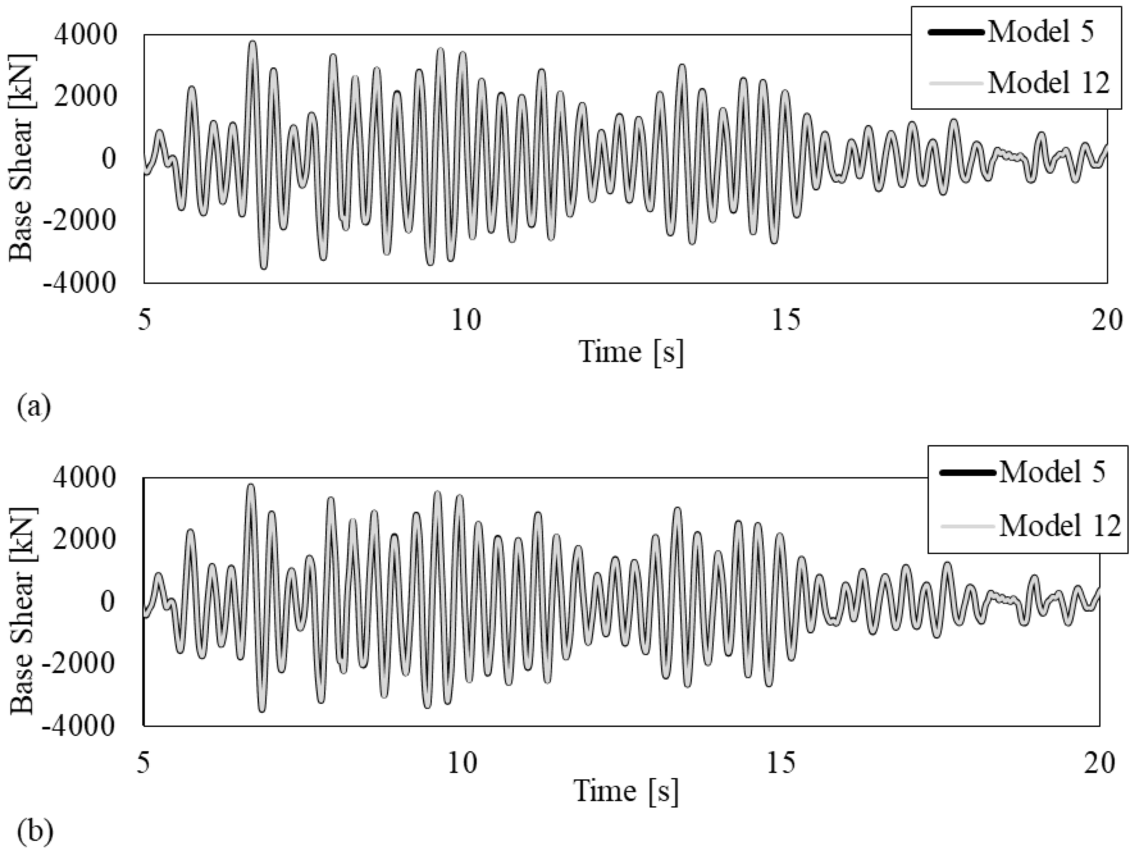

Figure 5.2 Comparison of base shear for Damping Model 5 and 12 for (a) force-based element formulation; (b) displacement-based element formulation

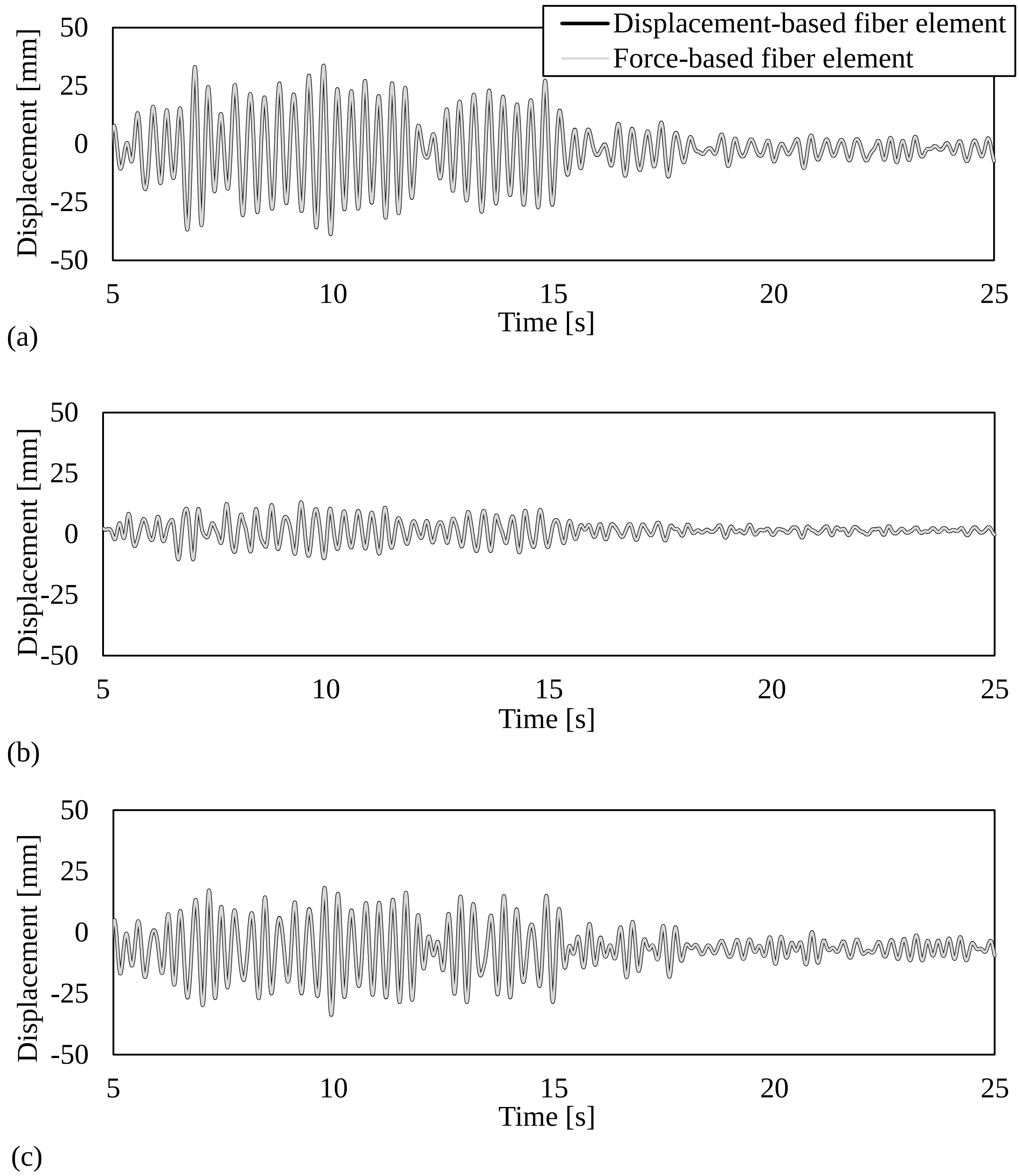

Figure 5.3 Comparison of peak displacement histories (a): *x*-direction; (b): *y*-direction; (c) *z*-direction for Model 5

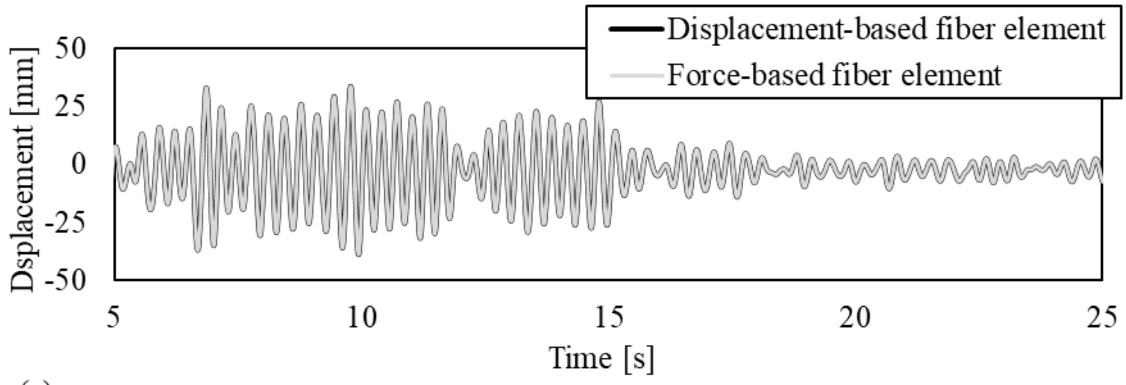

(a)

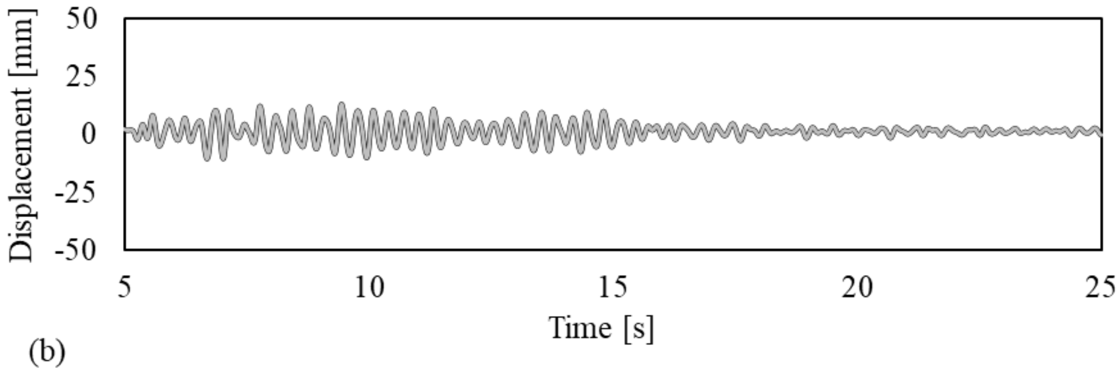

(b)

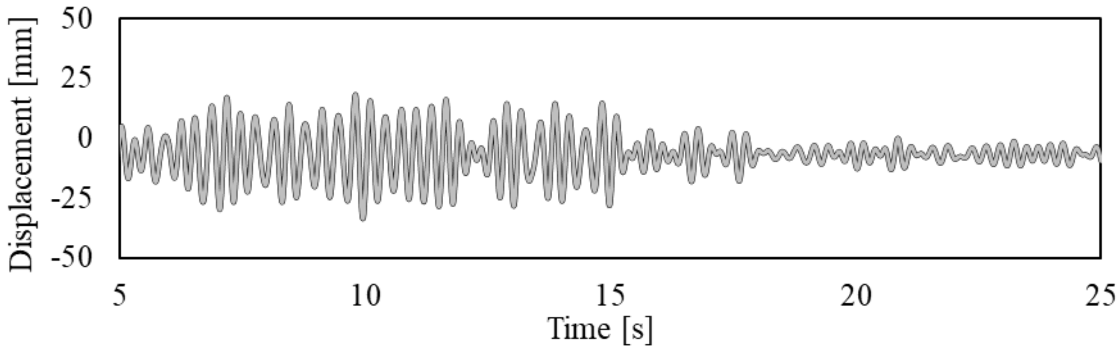

(c)

Figure 5.4 Comparison of peak displacement histories (a): *x*-direction; (b): *y*-direction; (c) *z*-direction for Model 12

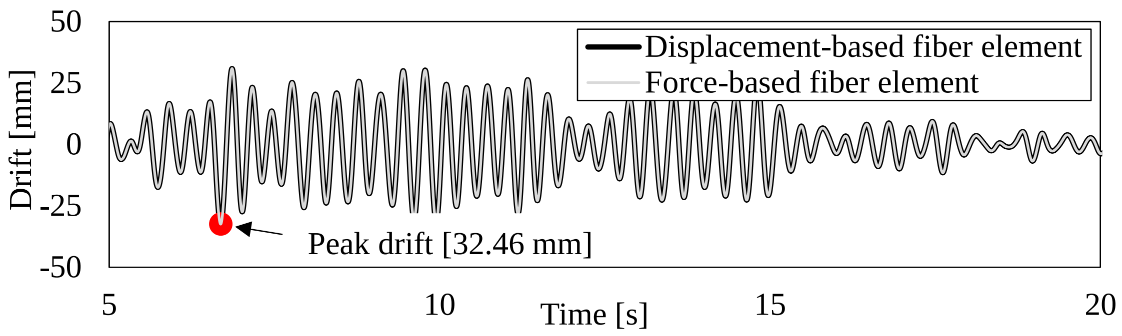

Figure 5.5 Drift response experienced by both formulation for Damping Model 5

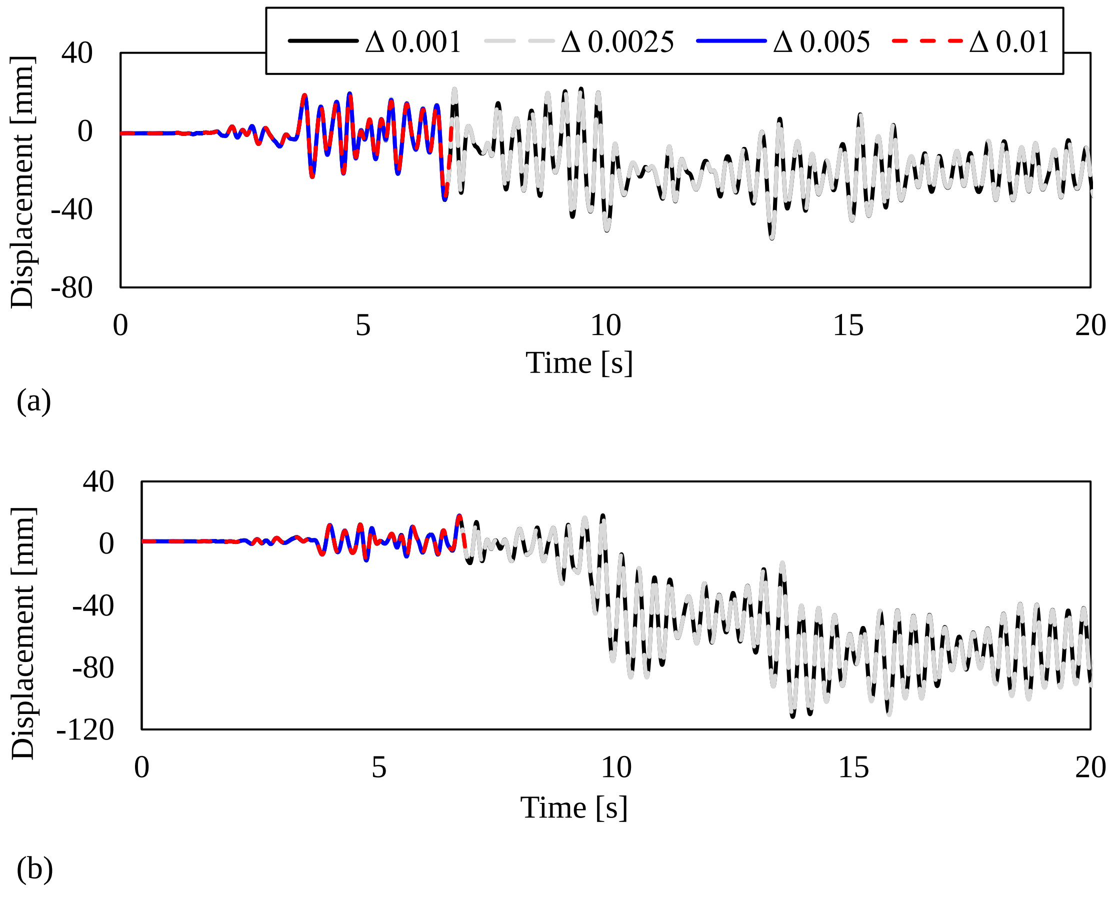

Figure 5.6 Peak elastic-plastic displacement response for displacement-based fiber element; (a) *x*-direction; (b) *z*-direction

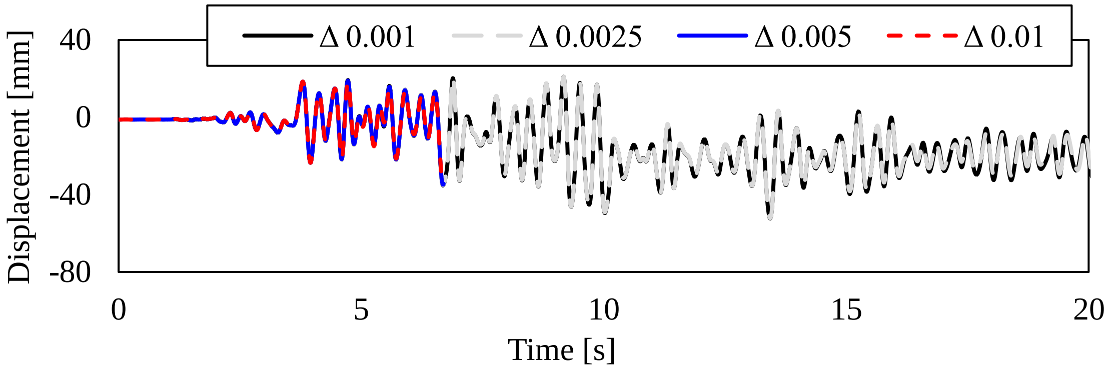

(a)

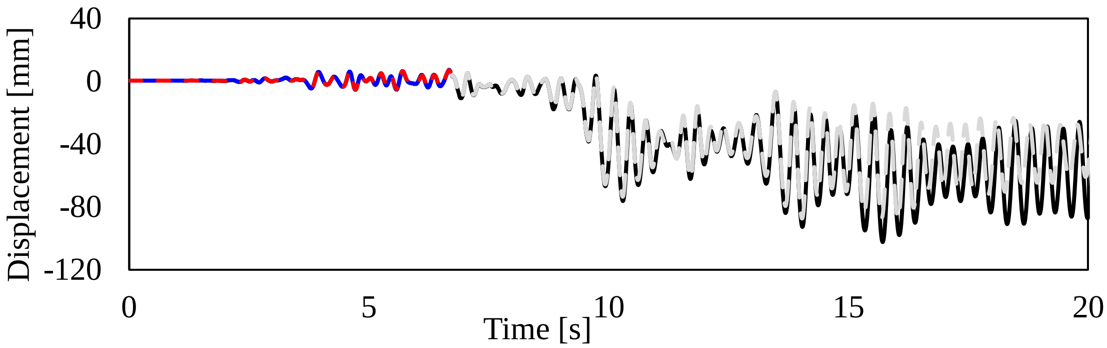

(b)

Figure 5.7 Peak elastic-plastic displacement response for force-based fiber element; (a) *x*-direction; (b) *z*-direction

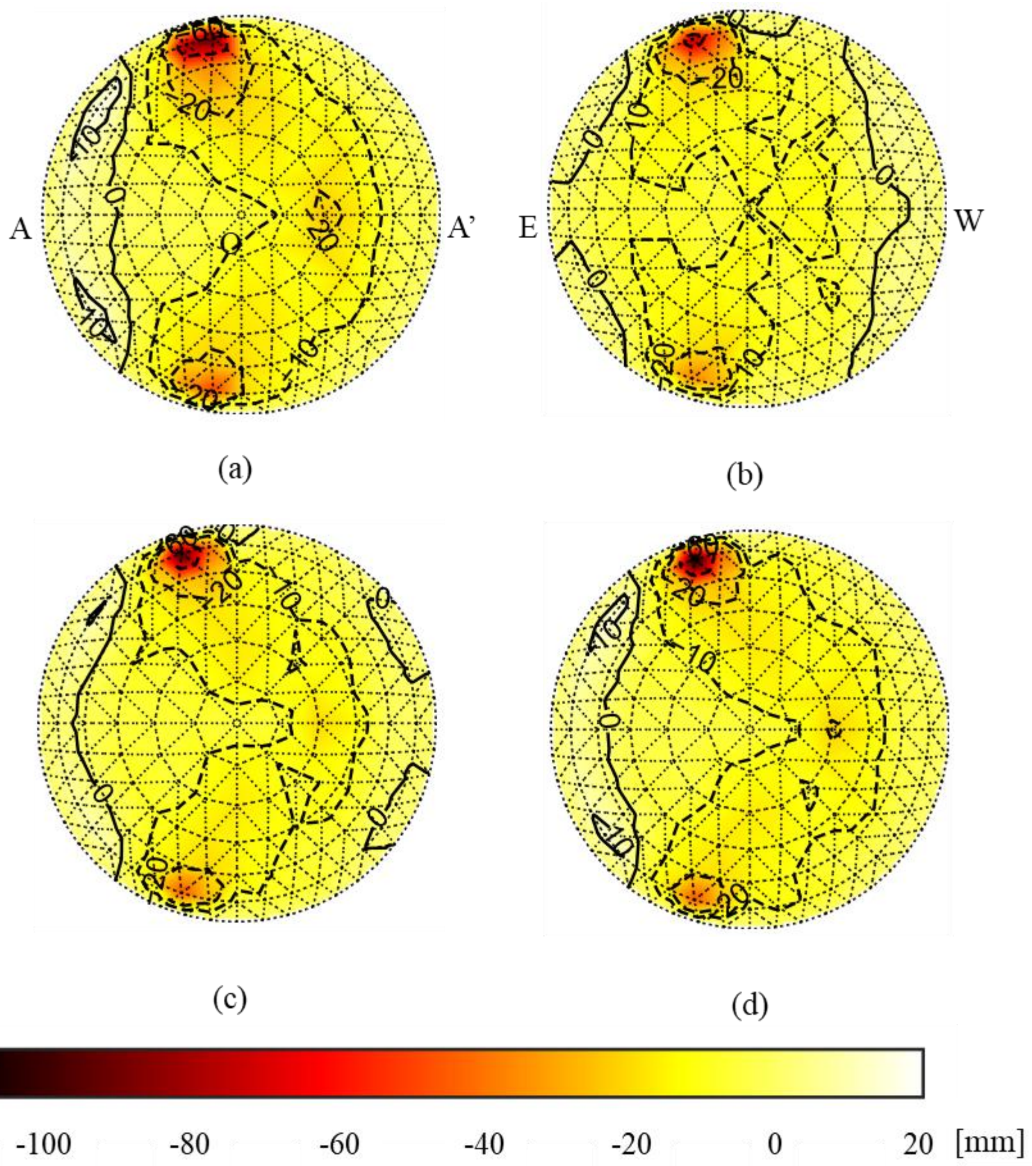

Figure 5.8 Contour plot of deformation for force-based fiber formulation in vertical direction

(a) 2 segments; (b) 4 segments; (c) 8 segments; (d) 10 segments per member

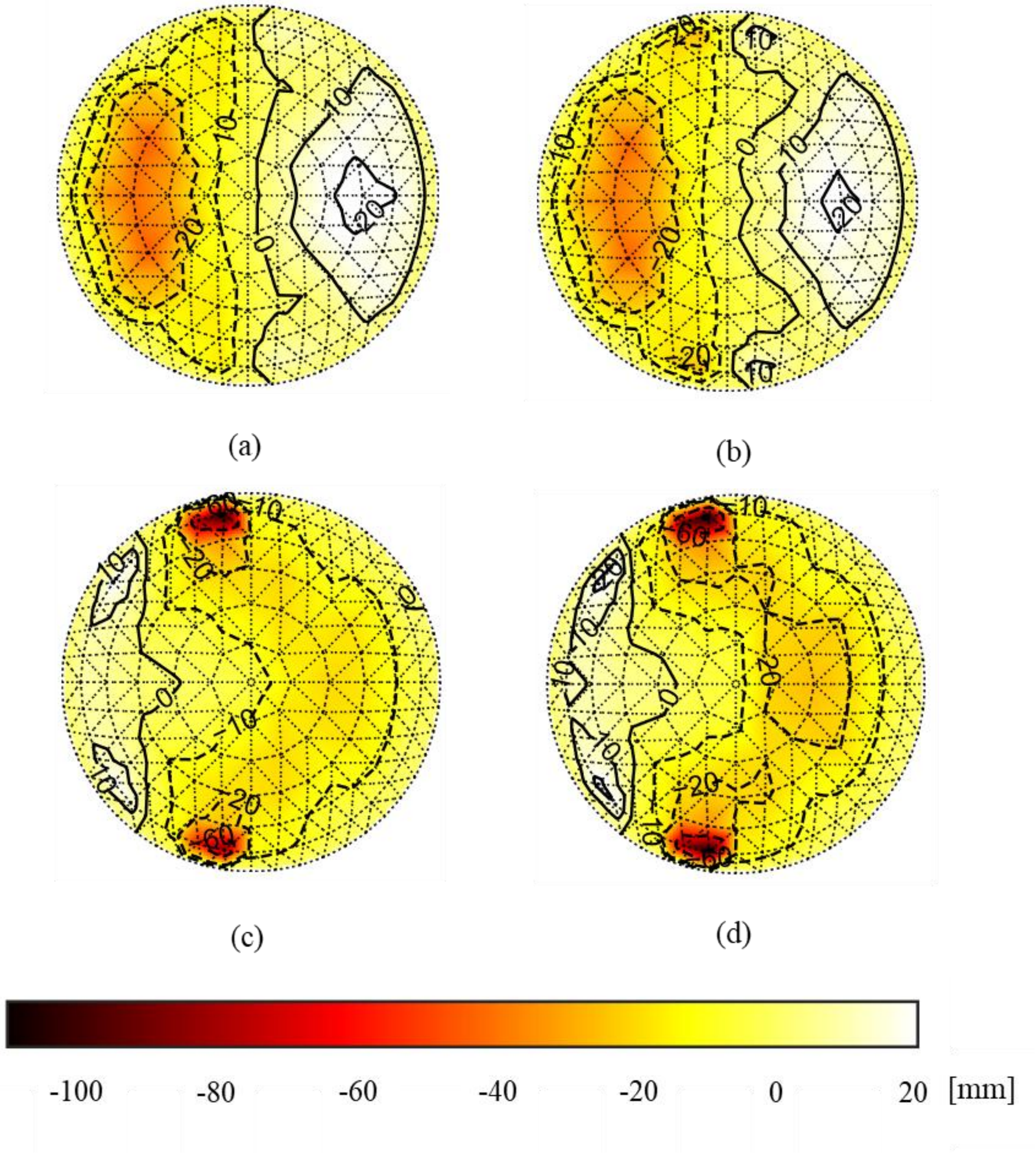

Figure 5.9 Contour plot of deformation for displacement-based fiber formulation in vertical direction (a) 2 segments; (b) 4 segments; (c) 8 segments; (d) 10 segments per member

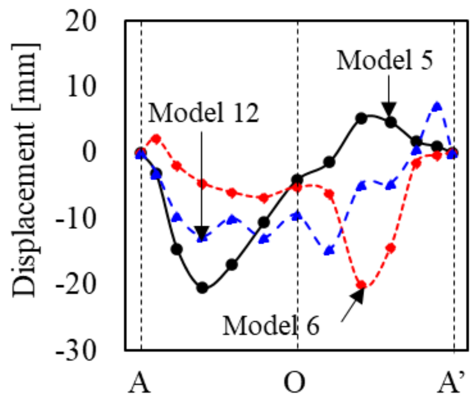

Figure 5.10 Distribution of vertical deformation along AOA’ at the time of peak vertical deformation for various damping model in model with force-based formulation

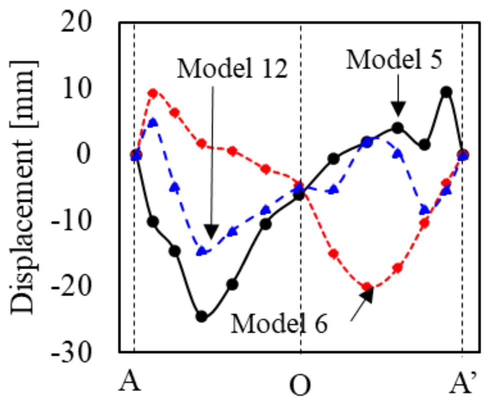

Figure 5.11 Distribution of vertical deformation along AOA’ at the time of peak vertical deformation for various damping model in model with displacement-based formulation

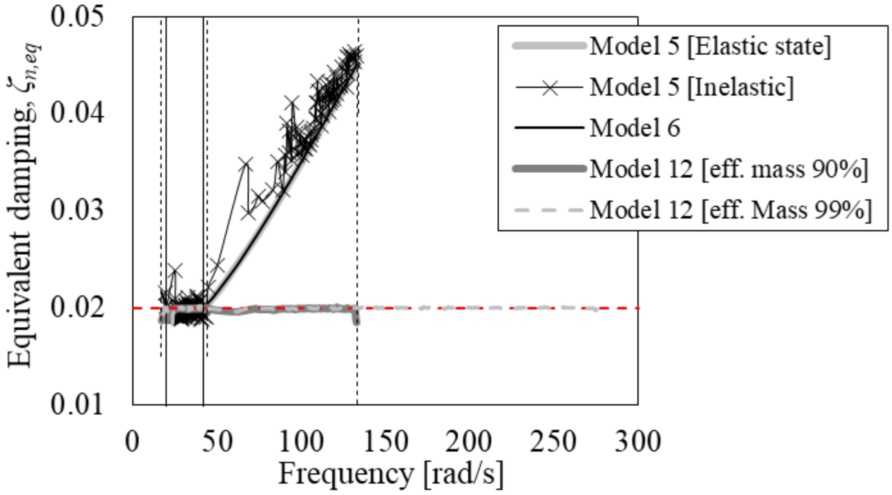

(a)

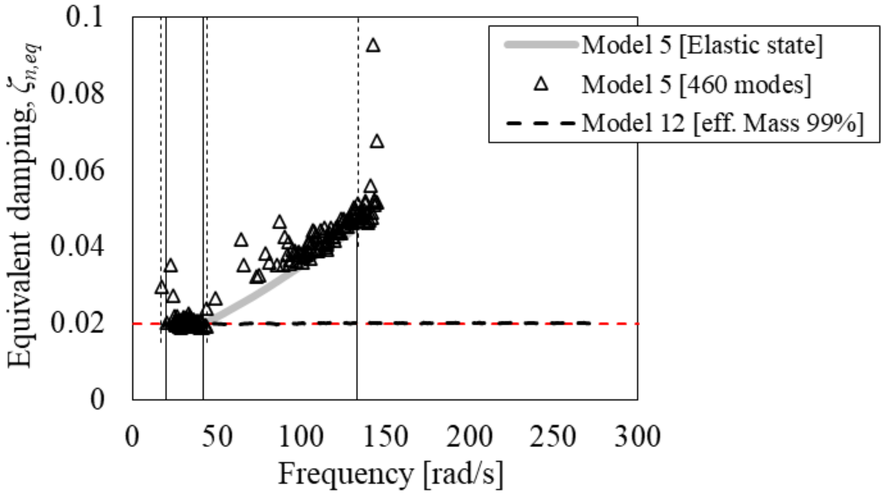

(b)

Figure 5.12 Frequency vs. Equivalent damping ratio for damping models in an inelastic system (a) comparison of various damping models; (b) comparison of Model 5 and Model 12 considering first 460 modes

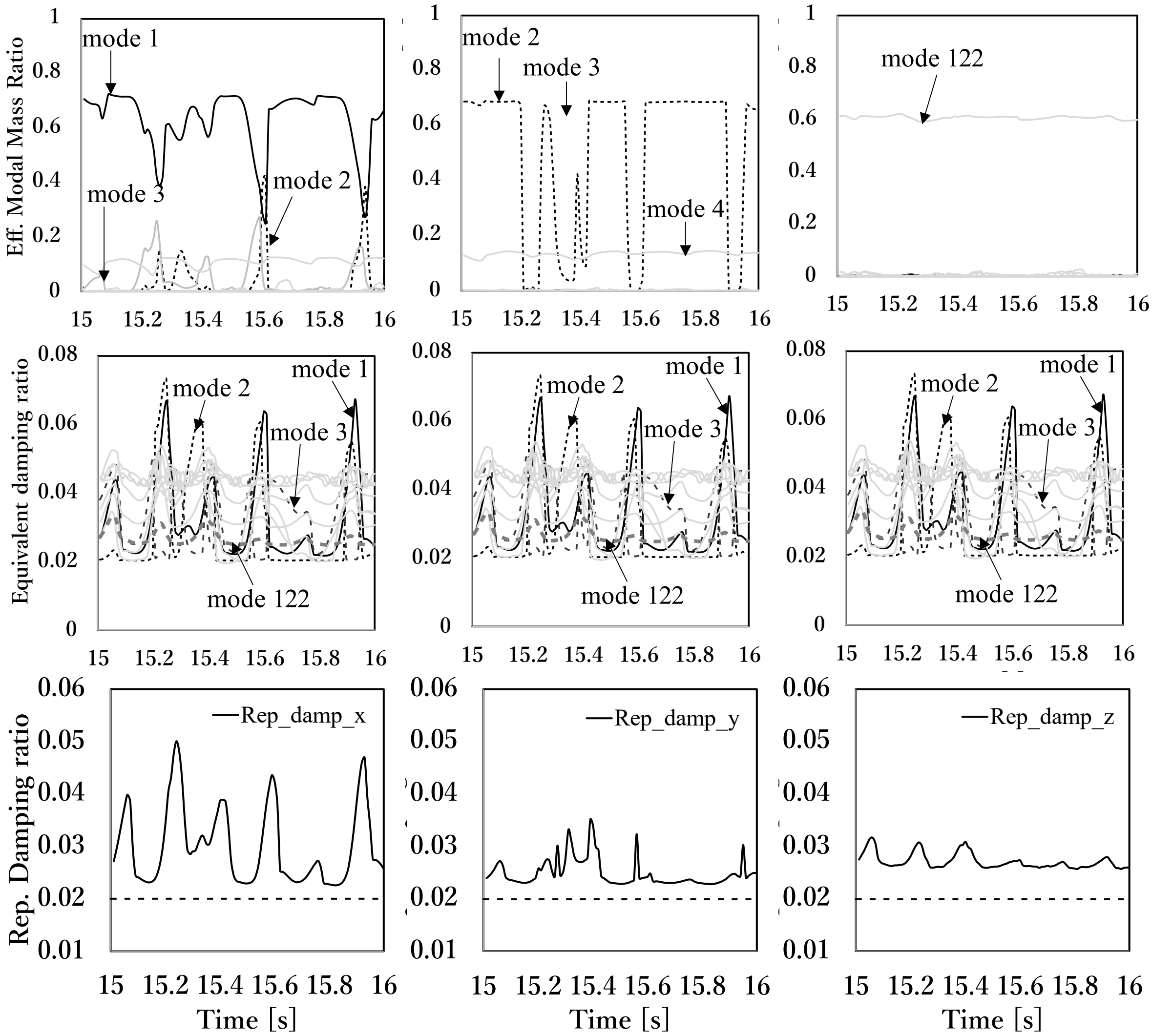

Figure 5.13 Calculation of representative damping ratio for Damping Model 5 for force-based fiber element formulation

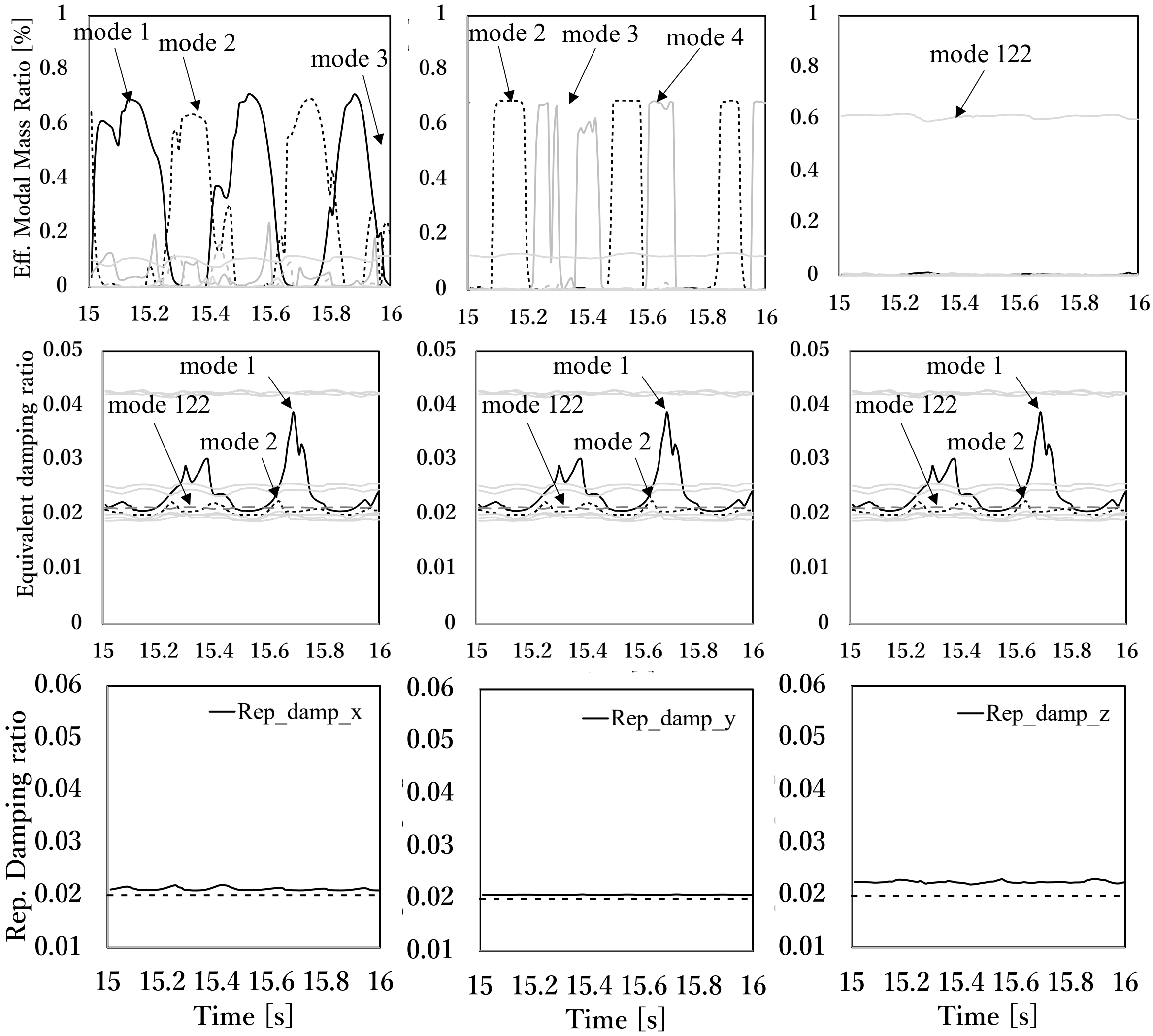

Figure 5.14 Calculation of Representative damping ratio for Damping Model 6 for force-based fiber element formulation

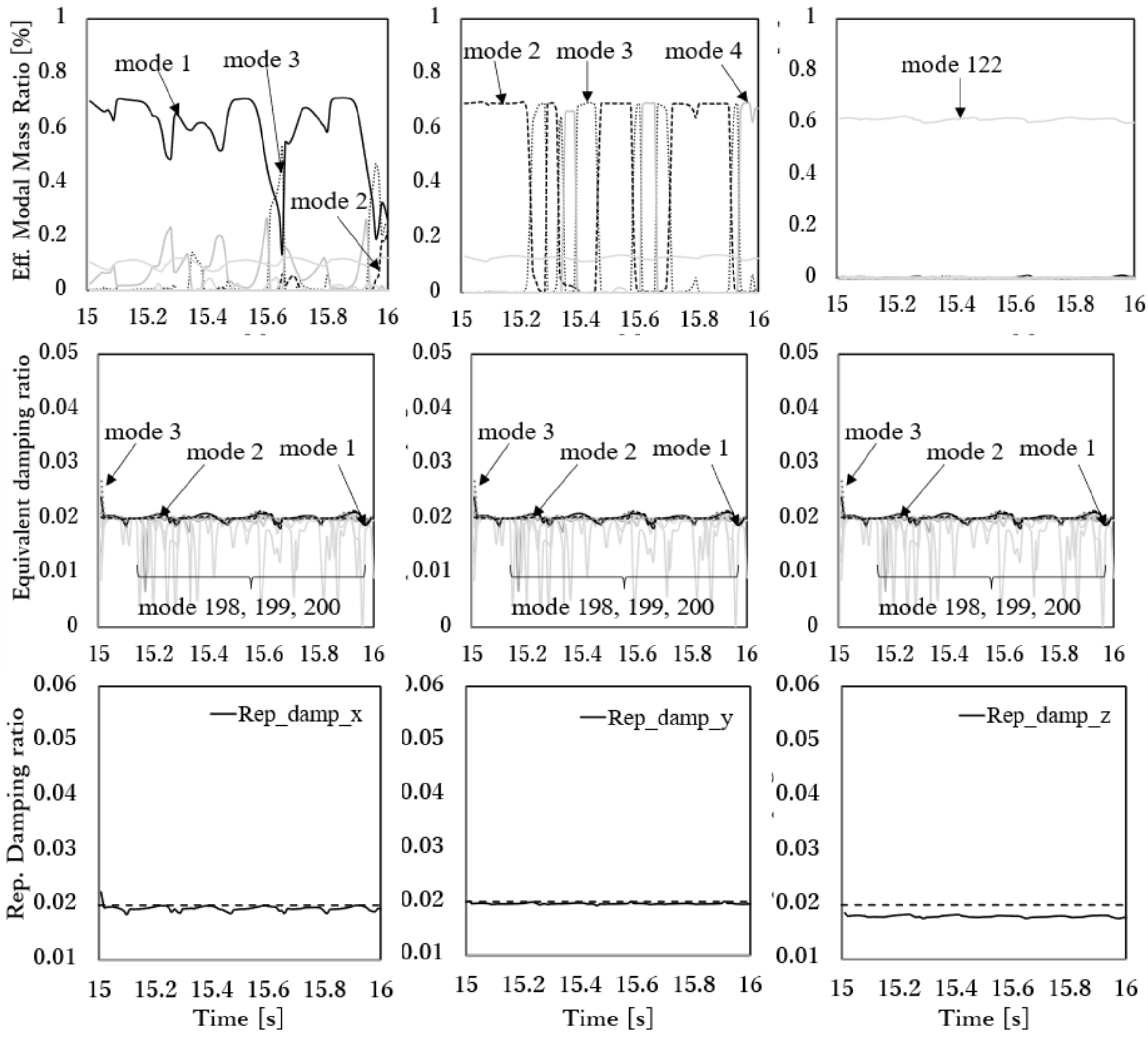

Figure 5.15 Calculation of Representative damping ratio for Damping Model 12 for force-based fiber element formulation

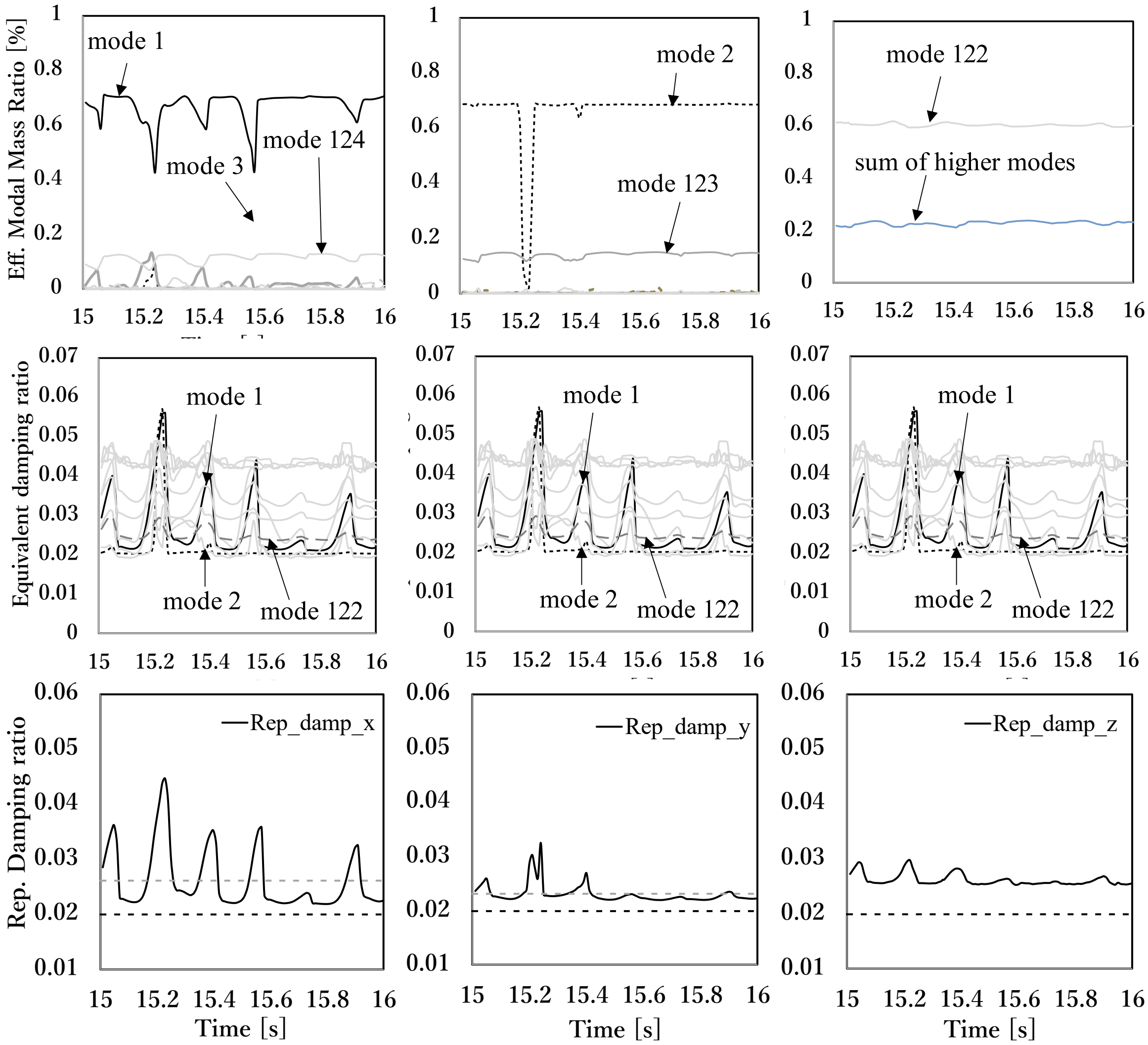

Figure 5.16 Calculation of Representative damping ratio for Damping Model 5 for displacement-based fiber element formulation

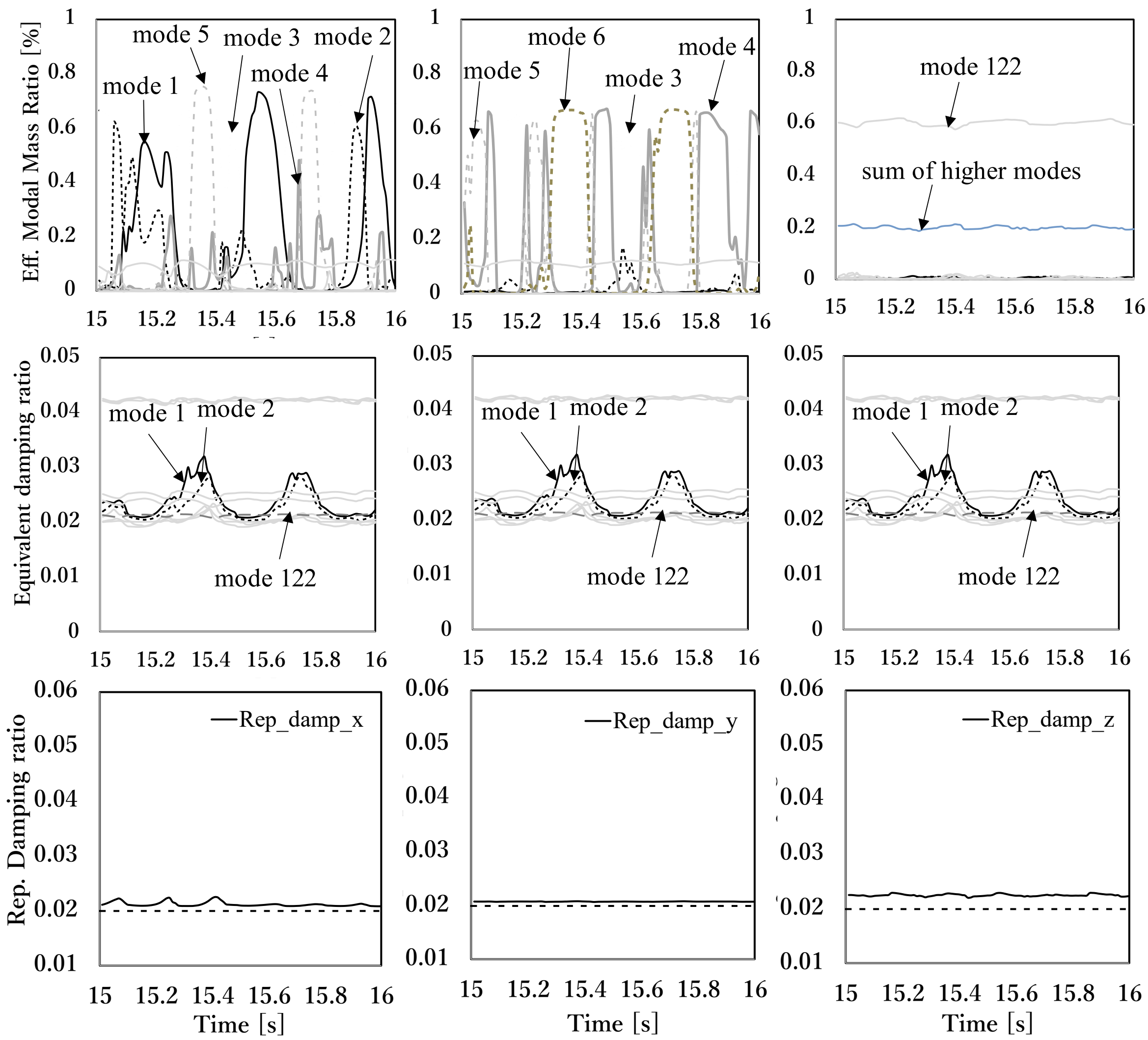

Figure 5.17 Calculation of Representative damping ratio for Damping Model 6 for displacement-based fiber element formulation

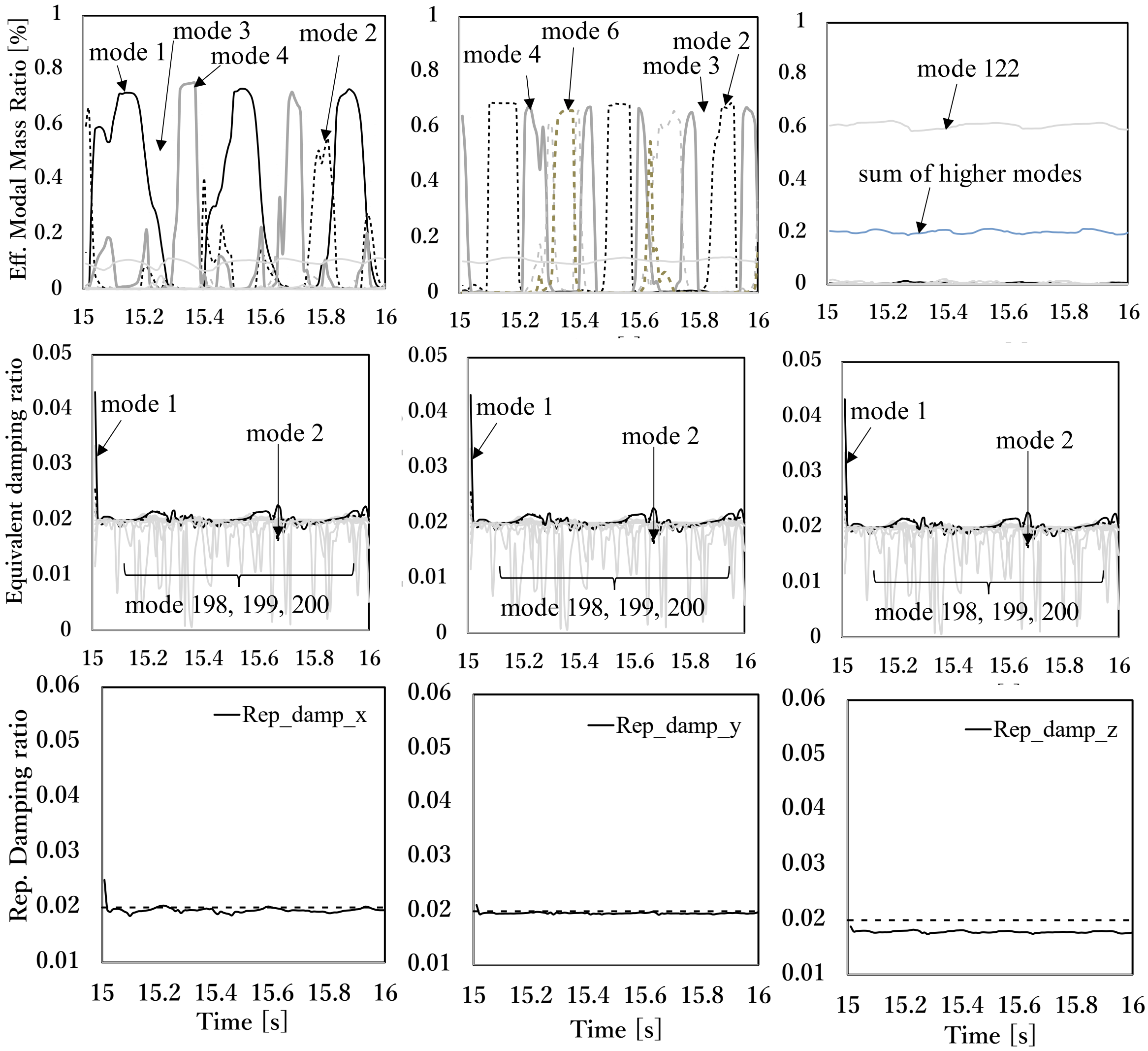

Figure 5.18 Calculation of Representative damping ratio for Damping Model 12 for displacement-based fiber element formulation

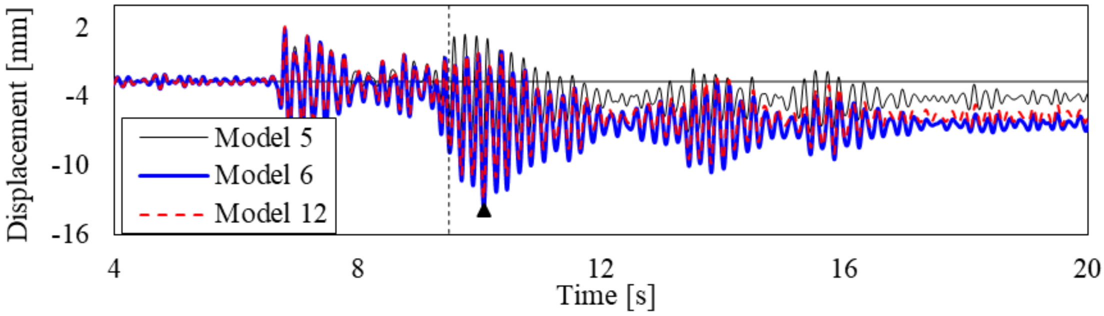

Figure 5.19 Simulated relative vertical displacement at the apex by various damping models by force-based fiber elements

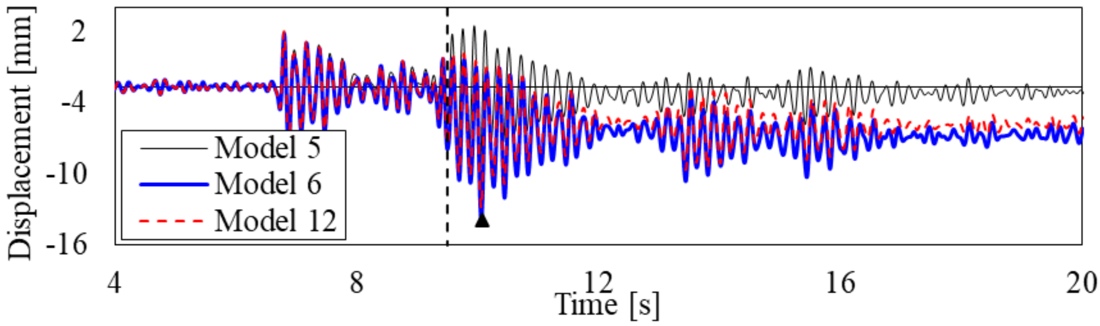

Figure 5.20 Simulated relative vertical displacement at the apex by various damping models by displacement-based fiber elements

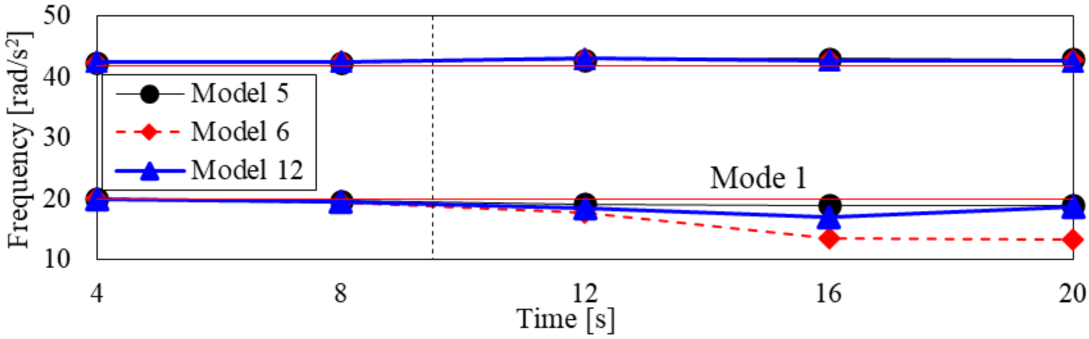

Figure 5.21 Frequency transition for force-based fiber element

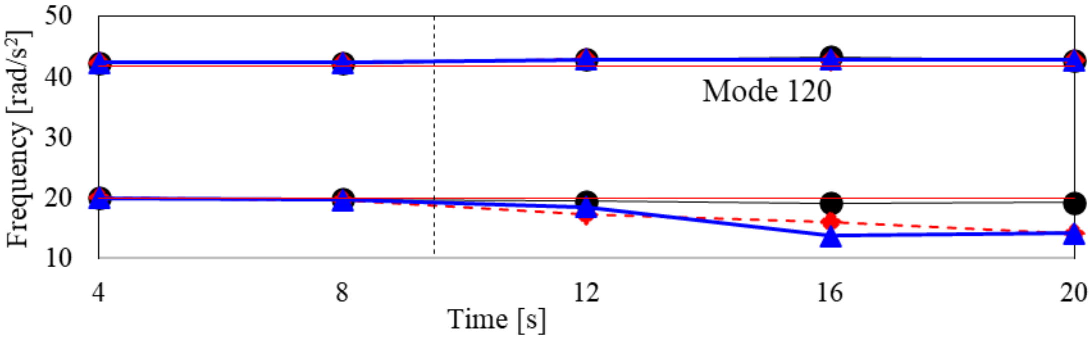

Figure 5.22 Frequency transition for displacement-based fiber element

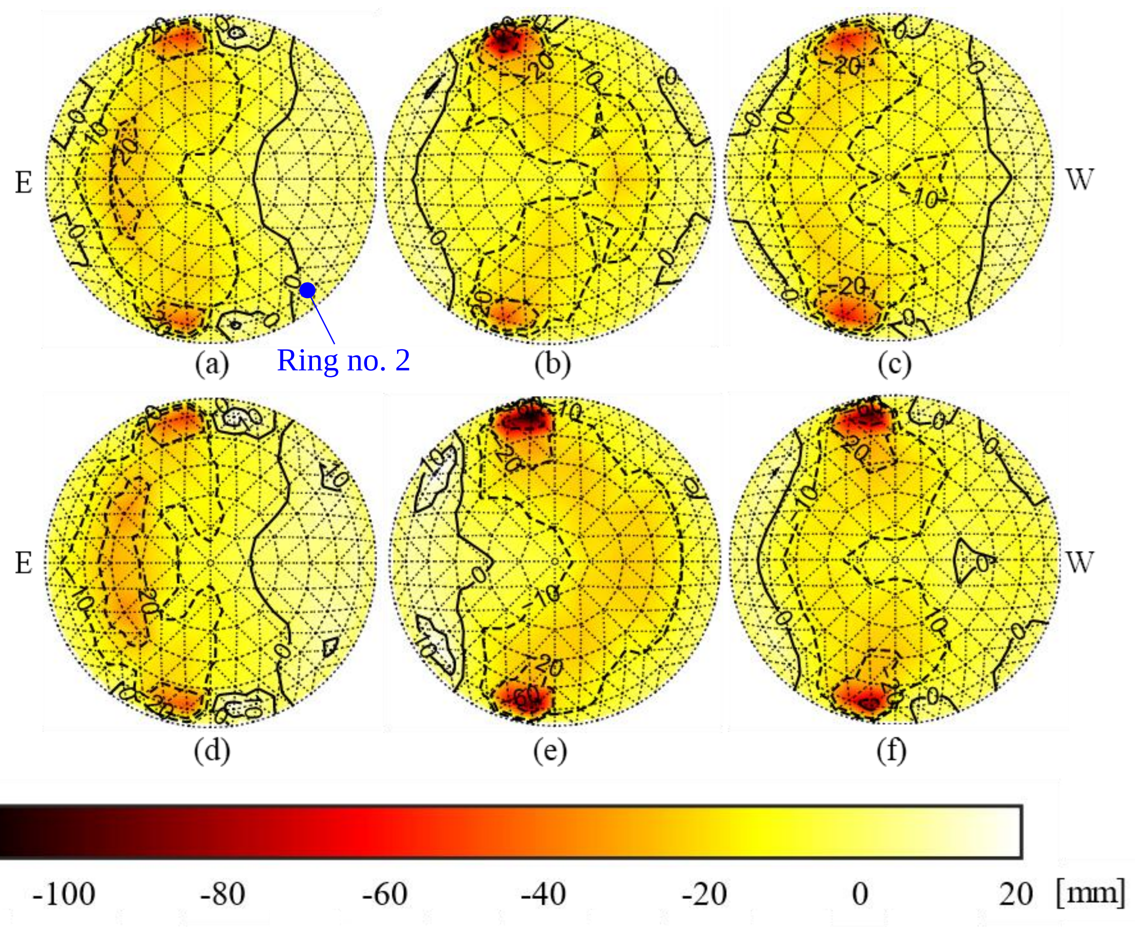

Figure 5.23 Contour for distribution of vertical deformation at the instance of peak displacement for force based element formulation: (a) Damping Model 5; (b) Damping Model 6; (c) Damping Model 12; for displacement based element formulation (d) Damping Model 5; (e) Damping Model 6; (f) Damping Model 12

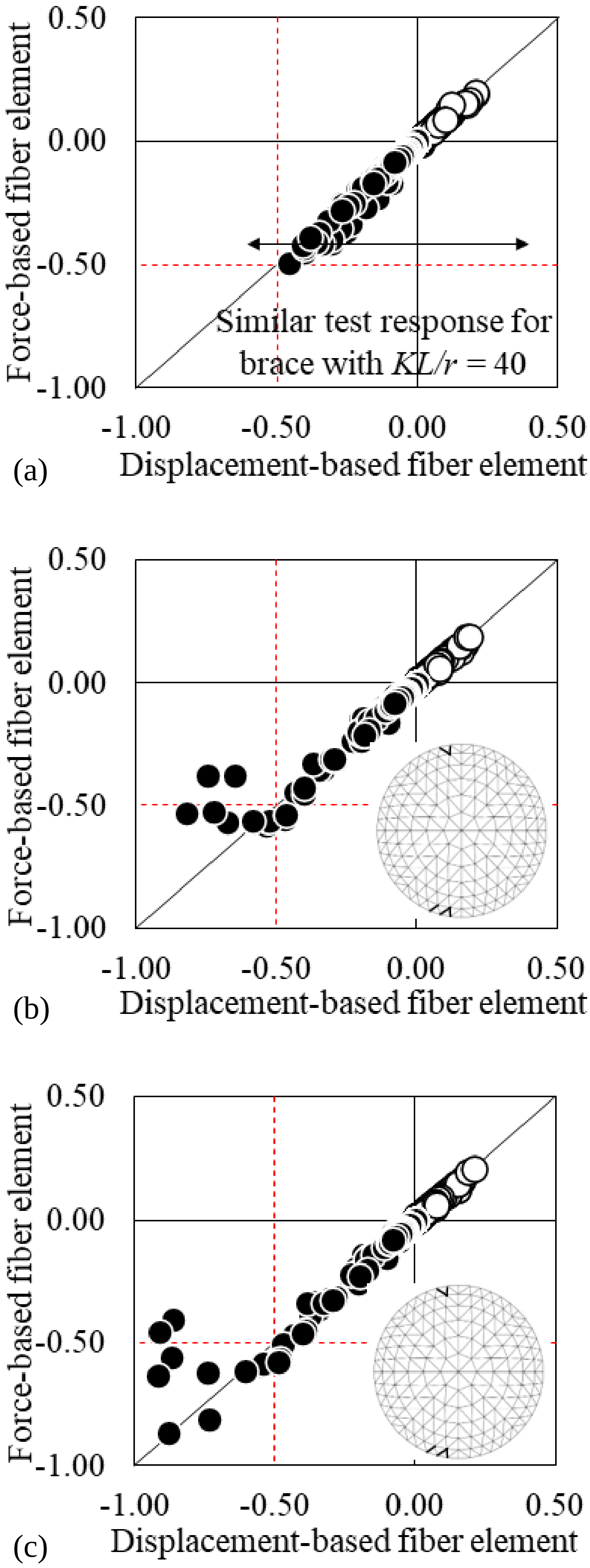

Figure 5.24 Simulated maximum and minimum δ/L [%] by force formulation versus displacement formulation: (a) Damping Model 5; (b) Model 6; and (c) Model 12

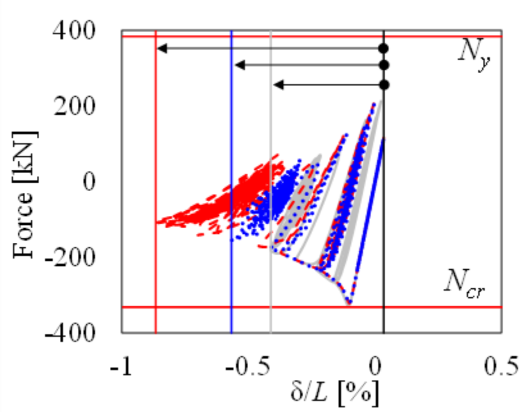

(a)

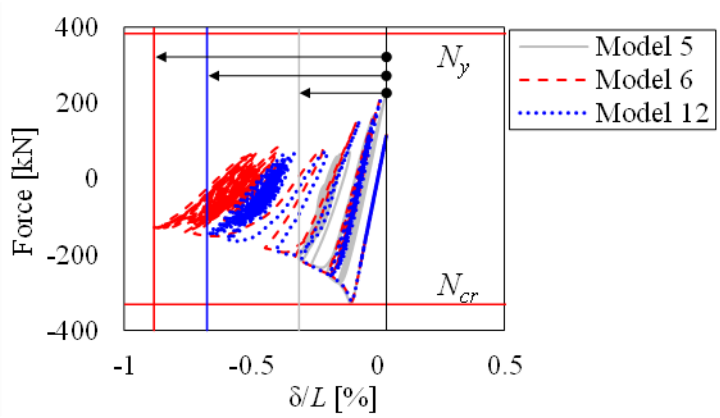

(b)

Figure 5.25 Hysteresis response for one of the members experiencing maximum deformation (a) force-based fiber element (b) displacement-based fiber element

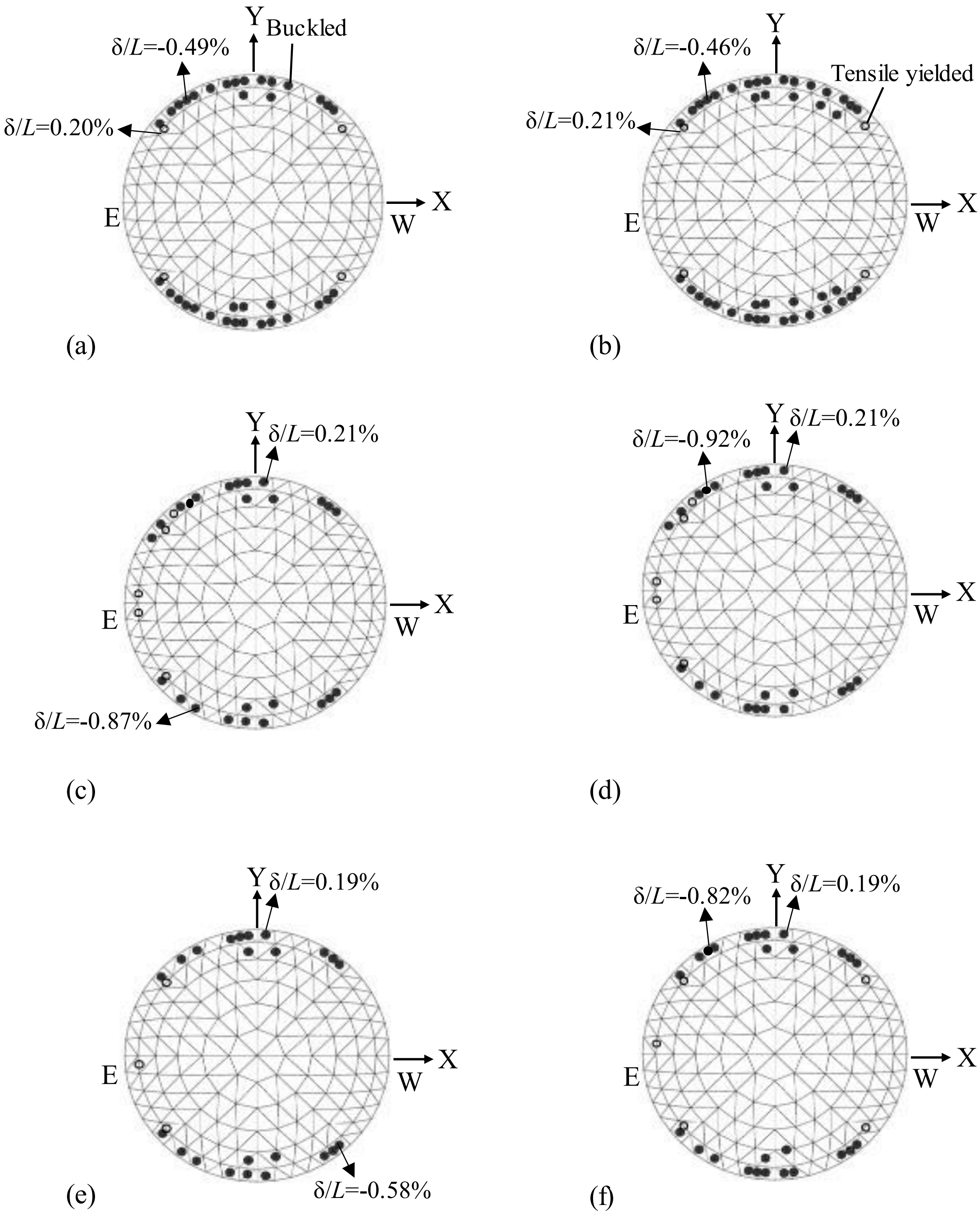

Figure 5.26 Buckled and tensile yielded members: force-based based fiber element – (a) Damping Model 5, (c) Model 6, (e) Model 12: and displacement-based fiber element – (b) Model 5, (d) Model 6, (f) Model 12

Table 5.1 Computational time required by various segments for Damping Model 6

Number of segments	Integration points		Peak displacement [mm]		Computational time [h]	
	Force formulation	Displacement formulation	Force formulation	Displacement formulation	Force formulation	Displacement formulation
2	7	3	95	45	2.76	1.55
4	7	3	75	44	4.53	3.61
8	5	3	102	108	9.02	7.83
10	5	3	111	109	11.29	9.96

Table 5.2 Computational time required by various damping model with 8 segments per member

Damping Model	Computational time [h]	
	Force formulation	Displacement formulation
Model 5	5.44	5.12
Model 6	9.02	7.83
Model 12	15.76	14.76

Table 5.3 Equivalent damping ratio for selected modes for force-based fiber elements

Mode	Damping model 5			Damping model 6			Damping model 12		
	Average	Maximum	Minimum	Average	Maximum	Minimum	Average	Maximum	Minimum
1	0.03	0.07	0.02	0.024	0.039	0.021	0.020	0.024	0.019
2	0.03	0.07	0.02	0.021	0.023	0.020	0.020	0.021	0.018
3	0.03	0.05	0.02	0.020	0.021	0.019	0.020	0.027	0.018
4	0.03	0.05	0.02	0.020	0.020	0.019	0.020	0.025	0.019
5	0.03	0.04	0.02	0.019	0.020	0.019	0.020	0.021	0.019
6	0.02	0.04	0.02	0.019	0.019	0.019	0.020	0.021	0.019
122	0.03	0.03	0.02	0.021	0.021	0.021	0.020	0.021	0.020
123	0.04	0.05	0.04	0.024	0.025	0.023	0.020	0.023	0.019
124	0.03	0.04	0.03	0.025	0.026	0.025	0.020	0.022	0.019

Table 5.4 Equivalent damping ratio for selected modes for displacement-based fiber elements

Mode	Damping model 5			Damping model 6			Damping model 12		
	Average	Maximum	Minimum	Average	Maximum	Minimum	Average	Maximum	Minimum
1	0.027	0.056	0.021	0.024	0.032	0.021	0.020	0.043	0.018
2	0.021	0.057	0.020	0.023	0.028	0.020	0.020	0.026	0.016
3	0.032	0.045	0.020	0.021	0.023	0.020	0.020	0.033	0.019
4	0.025	0.036	0.019	0.020	0.022	0.019	0.020	0.021	0.018
5	0.022	0.033	0.019	0.020	0.022	0.019	0.020	0.031	0.019
6	0.020	0.028	0.019	0.020	0.020	0.019	0.020	0.027	0.019
122	0.025	0.030	0.024	0.021	0.021	0.021	0.020	0.021	0.020
123	0.037	0.048	0.032	0.024	0.024	0.023	0.020	0.023	0.019
124	0.031	0.042	0.029	0.025	0.026	0.024	0.020	0.022	0.019

6 RESPONSE OF THE DOME SUBJECTED TO THE SUITE OF 28 PAIRS OF GROUND MOTIONS

6.1 Introduction

This chapter describes the nonlinear response of reticulated dome subjected to the suite of 28 pairs of ground motions selected as per FEMA P695. Displacement – based fiber element models were used to conduct numerical simulation. The response spectrum for the suit of 28 pairs of ground motion is discussed in Chapter 4.

6.2 Displacement response

Figure 6.1 illustrates the elongation of all axially-loaded members and the ratio of the number of members experiencing more than 0.5% contraction to the total number of all members, for each case of the reticulated dome subjected to the ground motions. For at least 95% of the members, deformation ranged from -0.5% contraction to 0.5% elongation. Given that the simulation of the steel braces as validated in the preceding chapter, showed excellent agreement with the test results, the outcomes for this case would be considered reliable.

Figure 6.2 and Figure 6.3 illustrate the maximum displacement response for each ground motion, represented as grey lines corresponding to the damping models. The lognormal distribution was used to compute the median and 84th percentile displacement as representative responses of the reticulated dome subjected to the suite of ground motions. Damping Model 5, i.e., initial-stiffness-proportional Rayleigh model, exhibited the smallest displacement response in most cases. This may be due to the spurious damping force resulting in reduced displacement. Damping Model 6, tangent-stiffness-proportional Rayleigh model frequently showed the largest displacement response. Since Damping Model 12, which represents modal-damping model, was considered the most realistic among these damping models based on the measurement of damping ratios, Damping Model 6 may be overly conservative.

Figure 6.4 shows the relationship between the maximum contraction across the axially-loaded members and the maximum vertical displacement experienced by the dome under a given seismic excitation. The maximum vertical displacement, resulted in the largest value among three directions as shown in Figure 6.2 and Figure 6.3, was used as an index to evaluate the seismic performance of the reticulated dome. The maximum contraction of the axially-loaded member was generally proportional to the maximum vertical displacement when the maximum contraction was less than -1% or the maximum vertical displacement was below 100 mm. Among the cases studied, the least maximum contraction was observed when Damping Model 5 was applied, likely due to spurious damping forces dissipating the seismic energy. For the reticulated dome subjected to the fault-normal ground motion RSN1176, the maximum vertical displacement reached 400 mm, equivalent to 1% of the dome span, when the maximum contraction of the axially-loaded member was close to -2.5% under Damping Model 6. This vertical displacement was more than twice as large as that observed with Damping Models 5 and 12. According to the damage evaluation criteria of the reticulated dome proposed by (Zhi et al. 2012), a displacement 200 mm serves as the threshold between heavy damage and collapse. Based on this criterion, the reticulated dome subjected to RSN1176 experienced heavy damage when using Damping Models 5 and 12, whereas it was classified as collapse when using Damping Model 6. Conversely, under the fault-parallel ground motion RSN1517, the maximum vertical displacement was less than 200 mm, i.e., 0.5% of the dome span, despite the contraction of the axially-loaded member reached -2.5% when Damping Model 6 was used. As a result, when the maximum vertical displacement was relatively large, the sensitivity of the choice of damping model become more pronounced.

6.3 Seismic risk evaluation

The following section discusses the effect of damping models on the seismic risk evaluation of the reticulated dome. Zhi et al. (2012) provided a damage factor Ds to estimate the damage state of the reticulated dome examined in this paper. Their study involved 3 span types, 3 rise-span ratios, and over 48 ground motion records. The damage factor was determined by several parameters, including the rise-span ratio, maximum displacement, displacement at the elastic limit, plastic strain in the dome, and propagation of plasticity. G. Nie et al. (2017) demonstrated the relationship between the damage factor Ds and the maximum node displacement for a reticulated dome nearly identical to the one used in this paper except for differences in a mass condition. Table 6.2 presents the damage states evaluated by the maximum displacement, based on the relationship between the damage factor and the maximum displacement. The range of the maximum displacement was estimated as rounded values, approximately representing the smallest of this relationship.

Figure 6.5 shows the response for three selected ground motions, along with the 84th percentile response (represented by the red dashed line) for both the fault-normal and fault-parallel cases. In the fault-normal case, for the Izmit event, Model 5 predicted heavy damage, whereas Models 6 and 12 predicted the collapse of the dome. For the Duzce and Chi-Chi events, all damping models predicted heavy and moderate damage, respectively. The 84th percentile prediction indicated moderate damage when using Damping Model 5, but heavy damage when using Models 6 and 12. In the fault-parallel case, heavy damage was observed with Models 6 and 12, and Model 6 predicted collapse during the Chi-Chi event.

Table 6.3 summarizes the computed maximum displacements for each ground motion case and the corresponding damage factors determined using the range shown in Table 6.2. The first column indicates the record serial number of ground motions (fault-normal and fault-parallel) and the damping models used. In the column for damage state, the alphabetical letters “I”, “M”, “H” and “D” represent “Insignificant”, “Moderate”, “Heavy” and “Destroyed”, respectively. Notably, the damage state “None” was not observed in any case. The maximum displacement was calculated as the three-dimensional displacement at a node over the entire duration of the ground motions. The record serial numbers of ground motions that exhibited different damage states across the damping models were highlighted. The largest variation in maximum displacement was observed in the case of the fault-parallel RSN1165. The damage state of the reticulated dome was classified as “Heavy” when Damping Model 5 was used, whereas it was classified as “Destroyed” when Damping Models 6 and 12 were used. Similarly, for the case of the highlighted ground motions except for the fault-parallel ground motions of RSN181, the damage states determined by Damping Model 6 and 12 were worse than that by Damping Model 5. This discrepancy may be due to the spurious damping force in Damping Model 5, which reduced the maximum displacement of thre reticulated dome. For the fault-parallel ground of RSN181, the difference in maximum displacement among the damping models was less than 5% of the maximum displacement, indicating that the dependency of the displacement response on the damping models was not significant. As noted earlier, Damping Model 12 provides the most reliable computational results in terms of damping ratio, Damping Model 5 may lead to unconservative evaluations. Consequently, the choice of damping models has the potential to significantly influence the seismic risk of spatial structures.

6.4 Conclusions

To conduct seismic risk evaluation of a reticulated dome structure, numerical simulations were conducted using 28 pairs of ground motions as per FEMA P695. Based on the Damage parameters laid out by G. Nie et al. (2017), the following conclusions are made:

1. For Damping model 5 – damage assessment was moderate for 61%, heavy for 36%, and damaged for 2% of the ground motions.
2. For Damping model 6 – damage assessment was moderate for 45%, heavy for 46%, and damaged for 7% of the ground motions.
3. For Damping model 12 – damage assessment was moderate for 54%, heavy for 41%, and damaged for 4% of the ground motions.
4. The tangent-stiffness-proportional Rayleigh damping model resulted in the most severe damage evaluation compared to the initial-stiffness-proportional Rayleigh damping and modal damping models, based on nonlinear time history response analysis of 28 pairs of ground motions.
5. Damping Model 5 has the potential to provide more unconservative evaluation of damage state for spatial structures than Damping Models 6 and 12. Damping Model 12 is recommended for the seismic risk analysis to avoid the effects of the spurious damping forces.

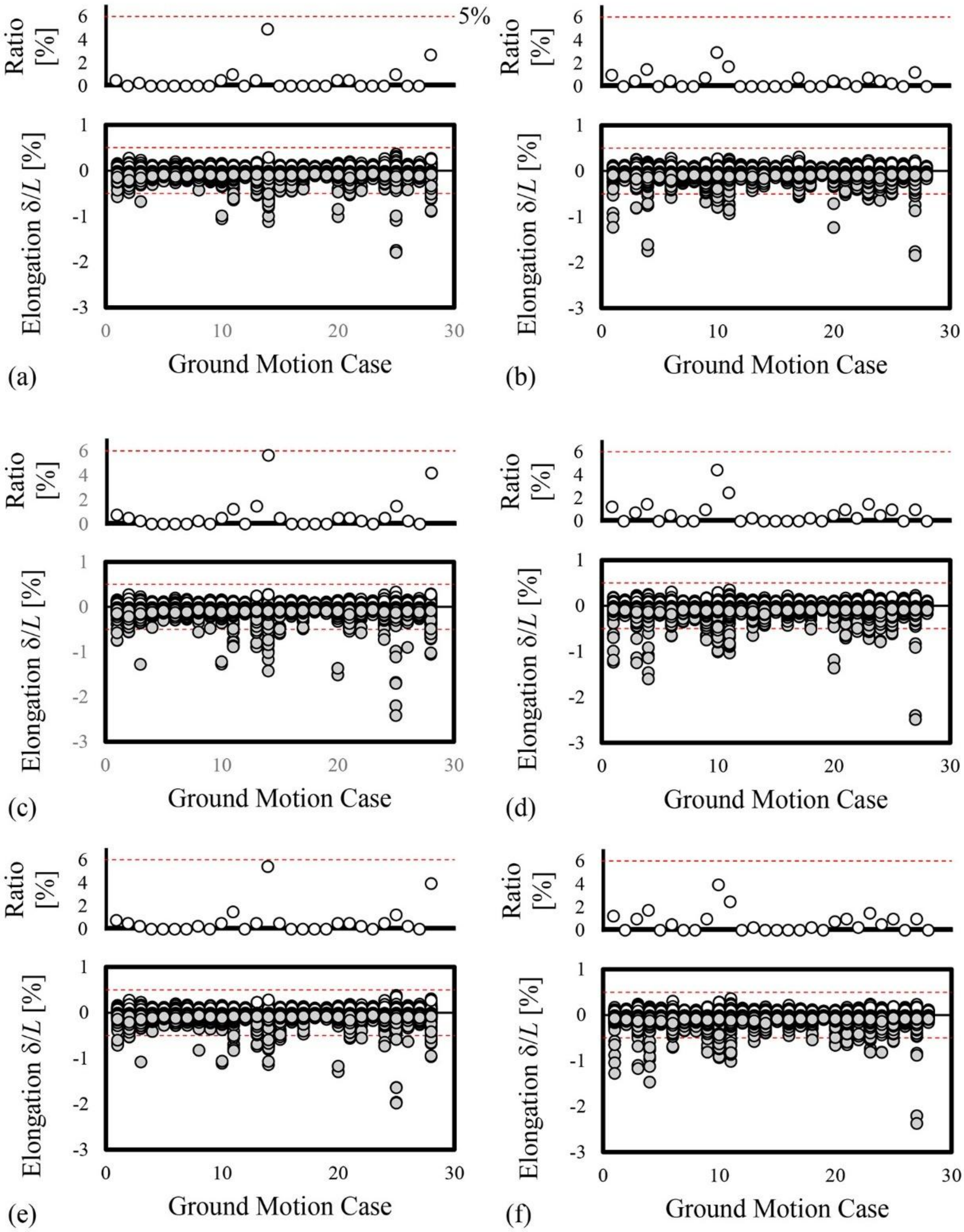

Figure 6.1 Ratio of the number of members experienced contraction more than 5% to that of total members, maximum elongation and contraction of members: (a), (c) and (e) are Damping Models 5, 6, and 12 for the dome subjected to the fault-normal ground motions; and (b), (d) and (f) are Damping Models 5, 6, and 12 for the dome subjected to the fault-parallel ground motions

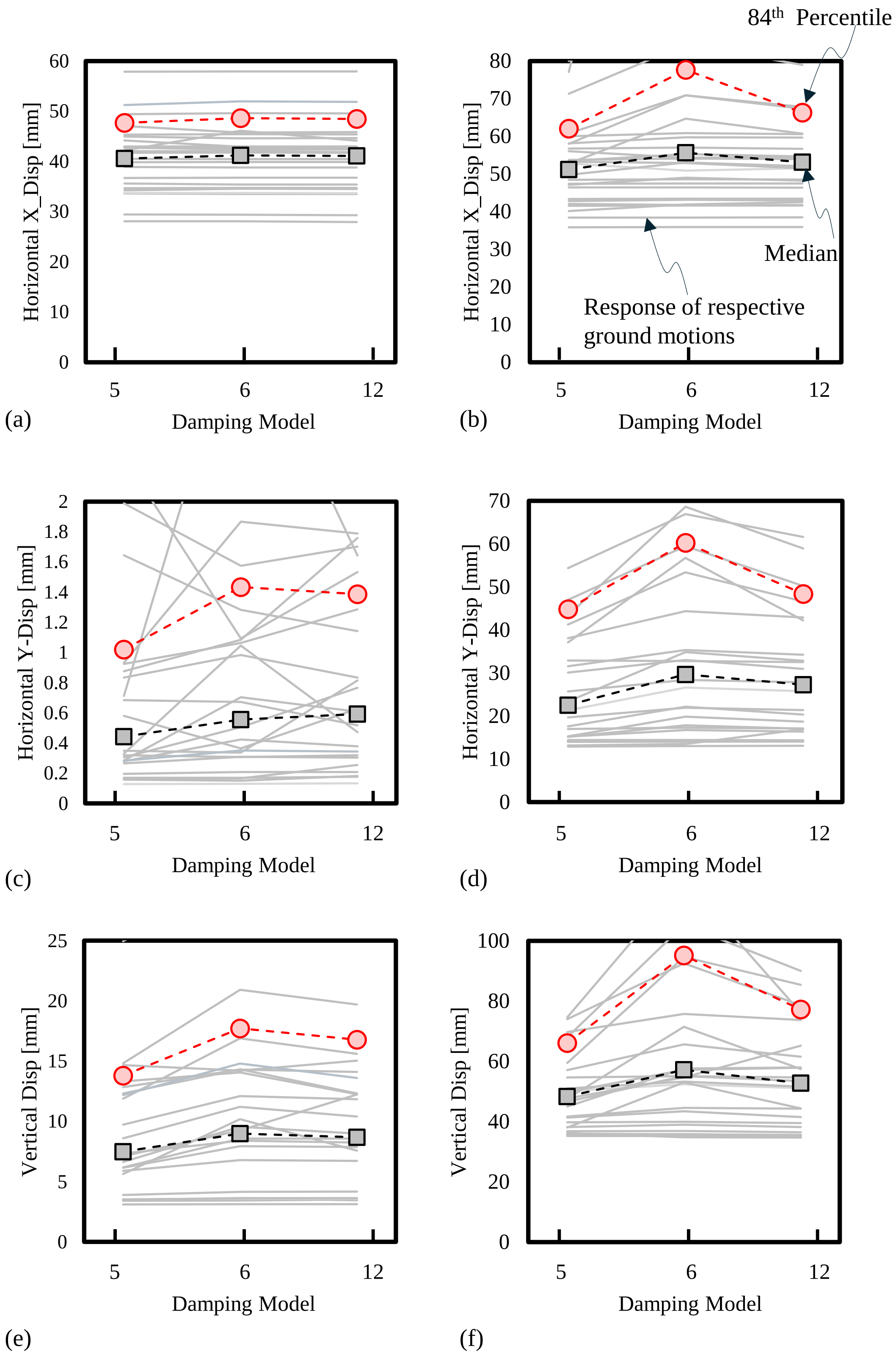

Figure 6.2 Maximum displacement of the reticulated dome subjected to the fault-normal ground motions: (a), (c) and (e) at Apex; and (b), (d) and (f) at a node that exhibited maximum

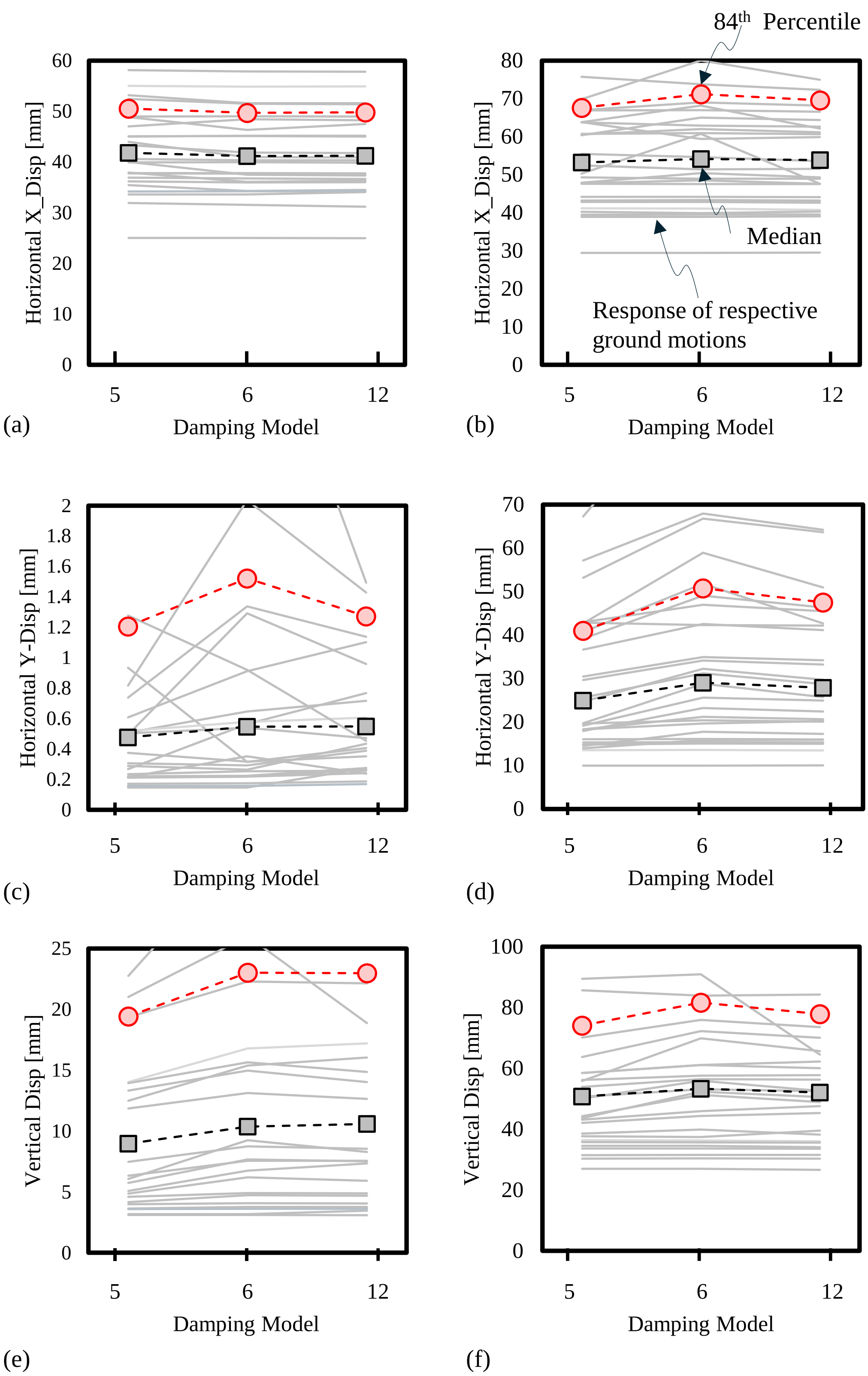

Figure 6.3 Maximum displacement of the reticulated dome subjected to the fault-parallel ground motions: (a), (c) and (e) at Apex; and (b), (d) and (f) at a node that exhibited maximum

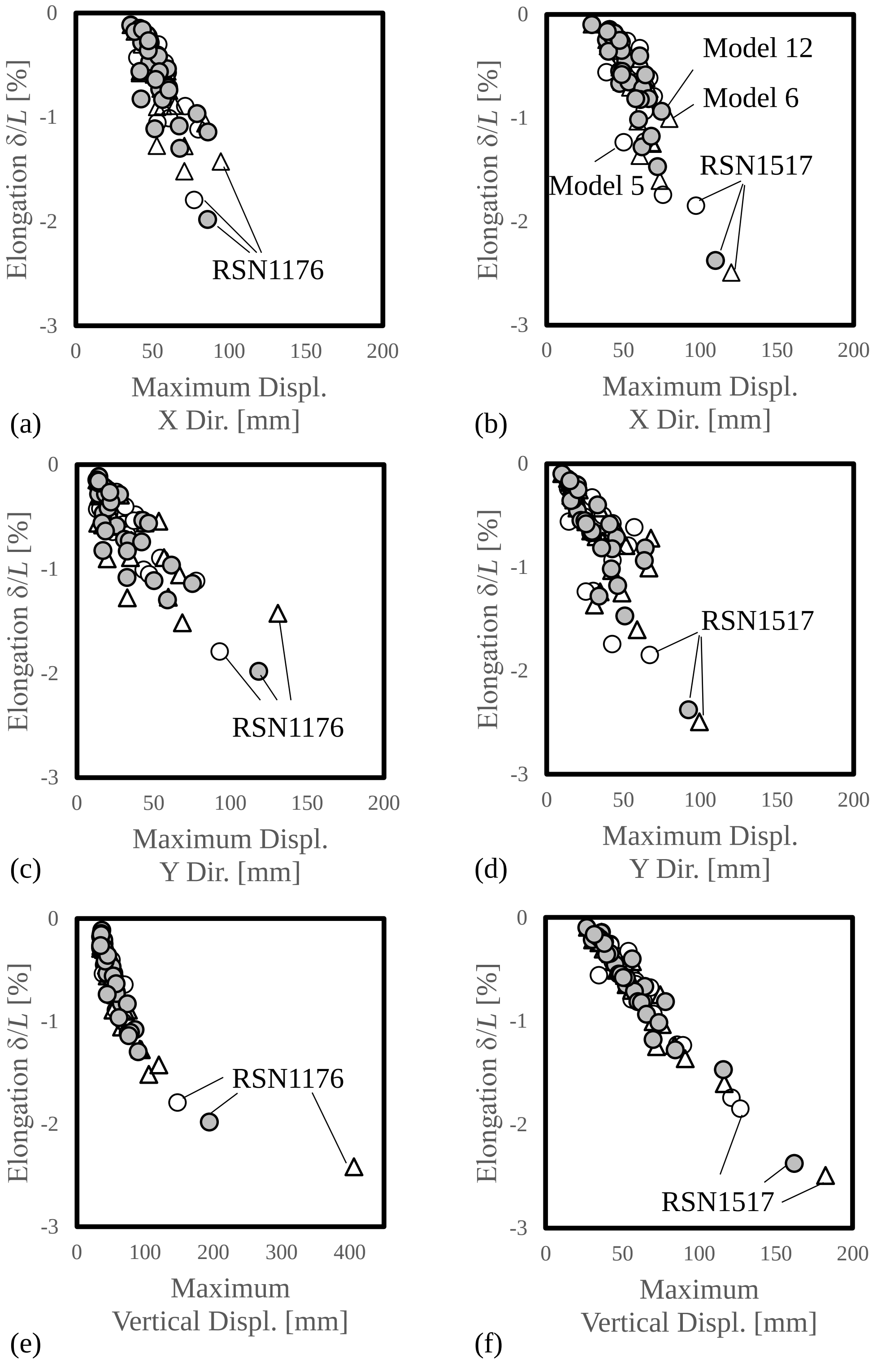

Figure 6.4 Relation between maximum elongation of members versus maximum vertical displacement in all nodes of the dome: (a), (c) and (e) are X-Dir., Y-Dir., and Vertical Dir. for the dome subjected to the fault-normal ground motions; and (b), (d) and (f) are X-Dir., Y-Dir., and Vertical Dir. for the dome subjected to the fault-parallel ground motions

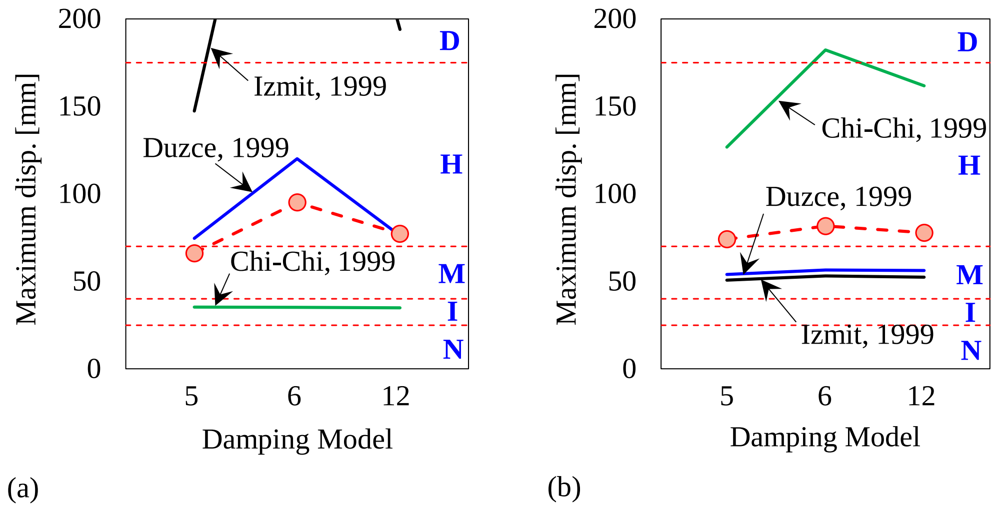

Figure 6.5 Damage states for various damping models under selected ground motions (Izmit, 1999 – RSN 1176; Duzce, 1999 – RSN 1605; Chi-Chi, 1999 – RSN 1517): (a) Fault-normal ground motions; (b) Fault-parallel ground motions

Table 6.1 Computational time for the study of 28 pairs of ground motions.

Case	Record Serial Number (RSN)	Computational time [h]						Computer	
		Fault Normal (FN)			Fault-Parallel (FP)			FN	FP
		Damping Model			Damping Model				
		5	6	12	5	6	12		
1	181	10.7	11.3	34.1	10.8	11.5	34.1	1	1
2	182	10.1	10.7	32.4	9.71	10.5	31.9	1	1
3	292	22.8	24.0	70.7	22.9	23.8	70.7	1	1
4	723	5.93	6.19	13.9	7.25	6.66	12.9	2	2
5	802	9.60	10.4	24.4	9.39	9.14	21.3	2	2
6	821	5.54	5.95	12.9	5.66	6.51	16.7	2	3
7	828	8.43	9.46	21.7	9.25	10.2	29.5	2	3
8	879	10.9	12.0	24.6	11.9	13.4	38.2	2	3
9	1063	5.49	6.02	14.6	5.65	6.20	15.1	3	3
10	1086	10.1	11.6	29.2	10.1	11.4	29.2	3	3
11	1165	8.16	9.13	22.1	8.30	9.20	22.7	3	3
12	1503	20.5	22.6	50.9	21.0	22.2	51.2	2	2
13	1529	19.0	21.3	57.9	19.0	21.2	57.8	4	4
14	1605	6.12	6.87	17.5	5.92	6.45	16.9	4	4
15	126	6.01	6.21	17.8	5.77	5.87	17.0	1	1
16	160	10.4	10.9	32.6	10.2	10.8	32.5	1	1
17	165	14.3	14.9	44.7	14.0	15.0	44.5	1	1
18	495	5.95	5.90	17.6	5.92	6.24	18.0	1	1
19	496	5.32	5.28	11.6	5.79	5.70	17.4	2	1
20	741	6.76	7.28	15.2	6.28	7.13	16.6	2	2
21	753	9.85	10.6	24.0	11.7	10.5	25.9	2	2
22	825	6.84	8.00	18.2	7.64	9.05	24.7	3	3
23	1004	11.7	13.2	34.3	11.8	13.5	34.7	3	3
24	1048	7.90	8.95	22.2	7.87	8.92	22.3	3	3
25	1176	9.30	10.8	25.9	9.24	10.3	25.6	3	3
26	1504	19.4	21.3	57.2	19.2	20.8	57.0	4	4
27	1517	18.3	20.9	57.3	19.2	21.2	57.8	4	4
28	2114	19.8	21.9	59.0	19.2	21.4	58.8	4	4

Table 6.2 Damage factor ranges of the reticulated dome based on the maximum displacement

Damage State	Range of Maximum Displacement [mm]
None (N)	0 – 25
Insignificant (I)	25 – 40
Moderate (M)	40 – 70
Heavy (H)	70 – 175
Destroyed (D)	>175

Table 6.3 Maximum displacement and estimated damage state

RSN	Maximum Displacement [mm]						Damage State					
	Fault-Normal			Fault-Parallel			Fault-Normal			Fault-Parallel		
	5	6	12	5	6	12	5	6	12	5	6	12
RSN126	71.0	72.8	71.6	52.6	57.6	56.8	H	H	H	M	M	M
RSN160	58.3	58.6	58.2	61.4	59.4	59.3	M	M	M	M	M	M
RSN165	65.7	70.2	68.1	53.6	56.2	54.2	**M**	**H**	**M**	M	M	M
RSN181	76.0	77.3	77.3	70.5	70.5	67.9	H	H	H	**H**	**H**	**M**
RSN182	71.6	75.5	75.1	53.2	61.4	59.3	H	H	H	M	M	M
RSN292	82.9	117.7	108.1	69.9	97.7	89.9	H	H	H	**M**	**H**	**H**
RSN495	50.6	50.7	50.3	47.7	47.6	47.4	M	M	M	M	M	M
RSN496	52.3	52.3	52.4	35.9	36.0	35.6	M	M	M	I	I	I
RSN723	67.2	67.9	67.7	77.8	76.6	74.5	M	M	M	H	H	H
RSN741	86.3	131.1	112.1	81.9	126.5	110.4	H	H	H	H	H	H
RSN753	76.5	80.0	75.8	59.9	77.1	65.2	H	H	H	**M**	**H**	**M**
RSN802	56.2	56.9	56.2	50.6	50.3	50.1	M	M	M	M	M	M
RSN821	58.0	58.2	58.2	63.8	63.1	62.7	M	M	M	M	M	M
RSN825	59.9	67.3	65.9	62.0	70.1	68.5	M	M	M	M	H	M
RSN828	59.0	58.9	59.1	49.8	49.6	49.6	M	M	M	M	M	M
RSN879	59.9	66.0	74.8	53.7	60.7	66.9	**M**	**M**	**H**	M	M	M
RSN1004	45.2	45.2	45.2	66.9	67.0	66.5	M	M	M	M	M	M
RSN1048	67.3	73.1	73.4	71.5	76.0	75.4	**M**	**H**	**H**	H	H	H

RSN1063	60.4	67.7	64.1	61.6	62.6	60.7	M	M	M	M	M	M
RSN1086	93.1	114.9	98.5	93.6	113.6	98.4	H	H	H	H	H	H
RSN1165	86.6	91.3	88.2	78.2	80.2	80.9	H	H	H	H	H	H
RSN1176	186.0	506.7	242.1	174.3	465.0	227.9	D	D	D	**H**	**D**	**D**
RSN1503	54.6	54.4	54.2	44.2	44.3	44.2	M	M	M	M	M	M
RSN1504	67.5	82.8	72.3	54.1	79.9	65.3	**M**	**H**	**H**	**M**	**H**	**M**
RSN1517	56.7	56.8	56.8	99.8	120.4	111.8	M	M	M	H	H	H
RSN1529	64.3	86.0	72.8	53.4	77.7	61.4	**M**	**H**	**H**	**M**	**H**	**M**
RSN1605	112.9	181.1	116.0	107.3	177.8	107.0	**H**	**D**	**H**	**H**	**D**	**H**
RSN2114	92.0	107.4	98.8	79.3	93.8	85.4	H	H	H	H	H	H

7 LOCAL-BUCKLING INDUCED DEGRADATION IN ROUND HOLLOW STRUCTURAL SECTIONS OF CONCENTRICALLY BRACED FRAME

7.1 Introduction

Steel concentrically braced frames (CBFs) are widely used in building construction to resist lateral seismic forces, in earthquake-prone regions. During intense seismic activity, th e braces in these systems undergo repeated inelastic deformations, including tensile yielding and compressive buckling. This behavior results in an asymmetric hysteresis response, characterized by a considerable reduction in compressive strength and the development of negative stiffness. A range of steel profiles, such as I-sections, and round, rectangular and square hollow structural sections (HSSs), angles, and channels, are commonly employed in CBF construction. Among these, HSSs are globally recognized for their efficiency as steel brace members. This chapter presents the implementation of a constitutive model within the beam-column fiber element to simulate local-buckling induced degradation in steel braces with round HSS. Subsequently, recommendations for applying the degradation model to concentrically braced frames were proposed.

7.2 Modelling of degradation in OpenSees

The Steel02 material model (Filippou, Popov, and Bertero 1983) is widely used for analysing the response of slender and intermediate braces, particularly when the global slenderness ratio is more than 40 as describe in Chapter 3. This numerical model achieves a good match between experimental and numerical simulation. However, it struggles to predict accurate response in post-buckling range for stocky braces having an effective slenderness ratio below 40. The response of stocky braces is predominantly governed by local buckling - a limitation that selected one-dimensional numerical simulations are unable to address effectively.

Modeling brace components with shell elements is a common approach but it computationally demanding. To address this challenge, an alternative is to model degradation at the material level. Three material models are capable of capturing softening behaviour: the Hysteresis material model, the Pinching4 material, and the IMK material model. These models define the material backbone based on experimental data. However, they require extensive material calibration to achieve accuracy. Furthermore, their applicability becomes limited in complex structures, such as spatial frames where axial members exhibit varying slenderness ratios.

To overcome this limitation, Suzuki and Lignos (2020) introduced a material model (SL Model) based on the Unified Voce Chaboche (UVC) uniaxial material model incorporating isotropic and kinematic hardening. The model was extended to capture local-buckling induced degradation. Initially developed for HSS columns with global slenderness ratios ranging from 16 to 40, the SL model was further refined for round HSS braces through comprehensive parameter adjustments were to ensure reliable simulation results.

The Authors developed a stress-strain constitutive model capable of capturing cyclic hardening and cyclic deterioration due to local buckling. This model is assigned to the fibers of the cross section and subsequently to the element. Authors utilized force-based fiber element consisting of two fiber-based segments at the end, with an elastic segment in between as shown in Figure 7.1. The uniaxial material model incorporates the proposed local-buckling induced degradation rule into the Voce-Chaboche plasticity framework. Stress-strain calculations are performed under the assumption that the plane sections remain plane after the deformation.

In cyclic hardening, the isotropic and kinematic hardening evolution can be represented by the Voce-Chaboche rule. This rule represents normal stress σ as an exponential function of plastic strain as expressed by Eq. (7.1),

$$\sigma = \sigma_{y,m} + \frac{C}{\gamma}\left[1 - e^{-\gamma_1 \varepsilon^p}\right] + Q_\infty\left(1 - e^{-b\varepsilon^p}\right) \tag{7.1}$$

where, $\sigma_{y,m}$ is the initial yield strength, parameters, C and γ define kinematic hardening, Q_∞ and b define isotropic hardening, calibrated from cyclic test.

Figure 7.2(a) shows the effective stress-strain relationship developed by (Suzuki and Lignos 2020) to capture degradation in compression caused by local buckling. In monotonic loading, the tensile path follows the Voce-Chaboche rule. The compression path diverts from the Voce-Chaboche rule once a capping stress $\sigma_{c,m}$ is exceeded. The subsequent post-peak slope $E_{d1,m}$ is steep, but slope $E_{d2,m}$ after the stress drops below $\sigma_{d,m}$ is rather flat. The model parameters depend on width-to-thickness and material yield strength as expressed by Eq. (7.2).

$$CP = a\left(\frac{b}{t}\sqrt{\frac{\sigma_{y,m}}{E}}\right)^{b} \tag{7.2}$$

Where, CP refers to parameter of interest, either $\sigma_{c,m}/\sigma_{y,m}$, $\varepsilon_{c,m}/\varepsilon_{y,m}$, $E_{d1,m}/E$, $E_{d2,m}/E$, $\sigma_{d,m}/\sigma_{c,m}$, and a and b are empirical parameters to be calibrated.

As shown in Figure 7.2(b), The i in the superscript of all variables counts the positive or negative excursion in cyclic loading. The stress-strain relationship deviates from the Voce-Chaboche rule when the line defined by slope $E_{pc1,c}^{i}\left(= E_{d1,m}\right)$ and intercept $\sigma_{d,1}^{i}\left(= \sigma_{c,m} + E_{d1,m} \cdot \varepsilon_{c,m}\right)$ is first crossed. The subsequent compression path follows softening defined by $E_{pc1,c}^{i}$ and $\sigma_{d,1}^{i}$, and possibly, a less steel softening defined by $E_{pc2,c}^{i}$. Upon load reversal to tension, the tension path takes slope $E_{u,t}^{i+1}$, and after exceeding stress $\sigma_{y,t}^{i+1}$, a less steep slope $E_{r,t}^{i+1}$. If the maximum tensile stress experienced from past cycles is exceeded, then the tension path reverts to the Voce-Cheboche rule and the reloading slope $E_{u,t}^{i+2}$ reverts to the initial value E.

In compression, the slope and stress values degrade with respect to the previous compression excursion as express by Eqs. (7.3) and (7.4).

$$\sigma_{(b \text{ or } d1 \text{ or } d2)}^{i} = (1-\beta_i)\sigma_{(b \text{ or } d1 \text{ or } d2)}^{i-2} \tag{7.3}$$

$$E_{(sh,c \text{ or } d1,c \text{ or } d2,c \text{ or } r,t)}^{i} = (1-\beta_i)E_{(sh,c \text{ or } d1,c \text{ or } d2,c \text{ or } r,t)}^{i-2} \tag{7.4}$$

In the above equation, β_i is a cyclic deterioration parameter defined by Eq. (7.5).

$$\beta_i = \left(\frac{E_i}{\Lambda \cdot \sigma_{y,m} - \sum_{j=1}^{i-1} E_j}\right)^{c} \tag{7.5}$$

Where Λ is a reference strain that depend on b/t and $\sigma_{y,m}$, E, and c is rate of cyclic deterioration taken as 1.0.

The unloading slope, from tension to compression or vice versa, and the break point along the tension path degrade according to Eqs. (7.6) and (7.7).

$$E_{u,(t\text{ or }c)}^{i} = \frac{\alpha_E}{\alpha_E - \left(\varepsilon_{u,t}^{i} - \varepsilon_{p,t}^{i-2}\right)} \cdot E \leq E \tag{7.6a}$$

$$E_{u,(t\text{ or }c)}^{i} = \frac{\alpha_E}{\alpha_E - \left(\varepsilon_{u,t}^{i} - \varepsilon_{p,t}^{i-2}\right)} \cdot E \leq E \tag{7.6b}$$

$$\sigma_{y,t}^{i} = \frac{\alpha_\sigma}{\alpha_\sigma - \left(\varepsilon_{u,t}^{i} - \varepsilon_{p,t}^{i-2}\right)} \cdot \sigma_{ym} \tag{7.7}$$

Where, α_E and α_σ are empirical parameters that depend on b/t and $\sigma_{y,m}$. If $\varepsilon_{u,t}^{i} > \varepsilon_{p,t}^{i-2}$ Eqs. (7.6) and (7.7) are invalid, in which case the unloading stiffness from tension to compression and compression to tension reverts to E.

Parameters Λ, α_E and α_σ are defined by Eq. (7.2), employing CP as any of those parameters. The cyclic stress-strain relationship of SL Model is controlled by the 4 parameters that define the Voce-Chaboche rule. Table 7.1 provides the cyclic hardening parameters for the material BCR295 which is utilised in the current study.

7.3 Calibration for round HSS for monotonic loading

7.3.1 Stub column test data

To calibrate the monotonic parameters that define softening branch in compression, data of stub column tests on round HSS as reported by Elchalakani, Zhao, and Grzebieta (2002), and Abe et al., (2023) summarized in Table 7.2 were utilized. To eliminate variability in stress–strain curve, the yield ratio was chosen between 1.0 and 1.3. The range of diameter-to-thickness was between 19 and 57, thereby covering stocky to slender range. Based on the variation observed in σ_u/σ_y , the specimens tested by the Authors, may not be from the same batch. All specimens exhibited inelastic local buckling, as indicated by a ratio $\varepsilon_u/\varepsilon_y$ exceeding 1.0. In Table 7.2 Specimen C8 demonstrated an irregular response, where inelastic local buckling occurred at a local buckling stress lower than the measured yield stress.

Figure 7.3 shows the normalized stress – strain curves for the stud columns. Normalization was performed using the measured yield stress values from the tests. The variations observed in the normalized stress-strain curves were attributed to differences in yield stress values.

7.3.2 Regression analysis results

For the calibration of material model following parameters were considered:

1) ε_c, σ_c: Capping strain and stress at which buckling is occurring
2) ε_d, σ_d: Post buckling strain and stress used to define post-buckling modulus E_{d1}
3) E_{d2}: Second post buckling modulus after which stabilisation of local buckling occurs
4) Normalized D/t for circular section is defined as follows:

$$\alpha = \frac{D}{t} \times \frac{\sigma_y}{E} \tag{7.8}$$

Figure 7.4 shows the variation of monotonic parameters with respect to normalised D/t ratio: Figure 7.4 (a) illustrates the variation of normalized local buckling strain. As the normalized D/t increases, the local buckling strain decreases, indicating that the section with higher D/t are prone to local buckling at smaller stain values. Figure 7.4 (b) presents the variation of normalized local buckling stress, the local buckling stress remain relatively stable for range of D/tratios. Figure 7.4 (c) and (d) illustrate post buckling stress and post buckling modulus E_{d1}, as the normalised D/t increases, σ_d decreases and E_{d1} becomes steep.

The figure suggests that while the local buckling stress remains relatively unchanged with increasing of D/t, the post-buckling strain and post-buckling modulus exhibit an increasing trend with higher D/t.

Table 7.3 provides the calibrated equation for defining material properties under monotonic and cyclic loading. In the post-buckling phase, the second negative stiffness modulus was set to 0.5% of the elastic modulus, as suggested by Yamada, Ishida, and Shimada (2012). To calibrate the cyclic parameters Λ, α_E and α_σ braces with specimen D/t ratio of 31, 40, KL/r of 16 and D/t ratio 40, and KL/r of 40 were used and is shown in Figure 7.9 as red circles. The values were determined through trial and error and are listed in Table 7.3.

The accuracy of the equations can be improved by expanding the dataset for stub columns with round HSSs or by performing virtual stud column tests using finite element software to address the gaps in the data. The current equations are applicable for the D/t ranging from 19 to 57, yield strengths between 357 and 454, which approximately align with the range specified for BCR 295.

Figure 7.5 and Figure 7.6 compare the loading curve from calibration model and corresponding test, the parameters are chosen to match strain hardening to maximum strength and degradation slope over the range of D/t. The predicted equation can capture the post-buckling behaviour with sufficient accuracy.

Figure 7.7 (a) and (b) compare the force-deformation responses between experimental tests and numerical simulations for a round-HSS brace with a D/t ratio of 40 and KL/r of 16. The force – deformation curve is in red curve till the deterioration after which it is continued with black line. The SL Model parameters used for calibration are provided in Table 7.3. The SL Model, with its calibrated parameters, effectively captured the degradation in strength and stiffness. However, the degradation is observed to initiate at lower strain values, in the early cycles, the numerical simulation predicted local buckling initiation at the 5th loading cycle, compared to the test results, in the test the local distortion was observed in the 16th loading cycle, as illustrated in Figure 7.7 (c). This discrepancy occurred because the SL material Model's algorithm transitions into the strain-hardening stage and evaluate current stress values relative to the capping stress. Once the stress exceeds the capping stress, the algorithm entered the post-buckling phase, adjusting the degradation slope. For further clarity, a simplified flowchart of the SL Model algorithm is provided in Appendix A3. This discrepancy can be addressed using two potential approaches:

1) Modifying the SL Model algorithm; Adjust the algorithm to compare strain values against capping strain values, rather than solely relying on stress, to better align with test observations.
2) Increasing the capping stress: Introduce a scaling factor to increase the capping stress, thereby delaying the onset of deterioration and preventing the algorithm from entering the post-buckling phase at lower strain values (earlier cycles). However, this approach may lack scientific accuracy and should be used cautiously.

This method ensures a more precise alignment between numerical simulations and test data, particularly in capturing the strain-hardening and post-buckling behaviour. To account for the higher local buckling strain values, a modification factor of 1.15 was applied to the capping stress value, determined through trial and error. As shown in Figure 7.7 (b), this adjustment resulted in a hysteresis response from the SL Model that closely aligns with the experimental data. The force – deformation curve is in red curve till the deterioration after which it is continued with black line. With the modification factor applied, local buckling was delayed until the 14^{th} loading cycle, significantly improving the accuracy in replicating the post-buckling behavior observed in the test. Similarly, Figure 7.8 illustrate the instance of local buckling in simulation and local distortion in test. The force – deformation curve is in red curve till the deterioration after which it is continued with black line. For the specimen having D/t = 31, the local buckling initiated at the loading cycle 14^{th}, while in test the initiation of local distortion at loading cycle 16. While for specimen having D/t = 40, the instance of local buckling was observed in loading cycle 2 in simulation in contrast to loading cycle 1 in test.

7.3.3 Validation of brace response

The test data listed in Table 7.4 for round-HSS braces were used to evaluate two different modeling techniques: (a) fiber models using a non-degrading material model; and (b) fiber models using the degrading material model calibrated as described in Section 7.3.2. Nine test results on round-HSS braces (Takeuchi and Matsui 2011; B. Kato and Akiyama 1977; Hodzumi et al. 1997; Elchalakani, Zhao, and Grzebieta 2002; Matsui et al. 2018; Black, Wenger, and Popov 1980) were chosen for this study. In the table, sections are described by exterior diameter D by wall thickness t. Furthermore, L, r, and K are total length, radius of gyration, and effective length factor; taking $K = 1.0$ if both ends are pinned, $K = 0.7$ if one end pinned and the other end fixed, $K = 0.5$ if both ends fixed.

All brace specimens were modeled using displacement-based elements with 8 segments and 5 Gauss-Lobatto integration points. The cross-section was divided into 12 fibers in the circumferential direction and 4 fibers in the radial direction (Karamanci and Lignos 2014), with each fiber assigned a calibrated SL Model. The force-deformation response obtained using the SL Model was then compared to the Steel02 material model, with parameters provided by Karamanci and Lignos (2014). For the static analysis, a displacement control analysis was conducted with the displacement increment of 0.1.

As illustrated in Figure 7.9, the specimens represented different slenderness (KL/r) and cross-section compactness (D/t). The U.S. seismic provisions (AISC 341 2022) specify: (i) For special concentrically braced frames, a section limit (highly ductile) of $D/t \leq 0.053\, E/(R_y F_y)$ for round-HSS braces, and slenderness limit $KL/r \leq 200$; and (ii) For special concentrically braced frames, a section limit (moderately ductile) of $D/t \leq 0.062\, E/(R_y F_y)$ for round-HSS braces; where E is elastic modulus, R_y is ratio of expected yield strength to specified minimum yield strength, and F_y is specified minimum yield strength.

The Japanese design code (MLIT 2020) evaluates brace ductility based on slenderness ratio as: (i) Rank BA (most ductile) if $KL/r \leq 495/\sqrt{F}$; (ii) Rank BB (ductile) if $495/\sqrt{F} \leq KL/r \leq 890/\sqrt{F}$ or $1980/\sqrt{F_y} \leq kL/r$; and (iii) Rank BC (less ductile) if $890/\sqrt{F} \leq KL/r \leq 1980/\sqrt{F}$); where F is the yield strength assumed in design in N/mm^2. The Japanese design code does not specify section limits. The 9 specimens were selected to represent all ranges of ductility of U.S. and Japanese design. Figure 7.9 indicates the section limits, in D/t, per U.S. seismic provisions (AISC 341 2022) and slenderness limits, in KL/r, per the Japanese design code (MLIT 2020) using $E = 2.05 \times 10^5$ N/mm^2, $F = F_y = 235$ N/mm^2 and $R_y = 1.6$. Round HSS braces have slenderness ratios (KL/r) ranging from 15.9 to 144, diameter-to-thickness ratios D/t ranging from 14.3 to 63.8, and yield strength in the range of 165 – 360 N/mm^2. The selected specimens were shown against previously simulated braces by Karamanci and Lignos (2014) in hollow white circles.

Figure 7.10 and Figure 7.11 compare the force-deformation response for round braces modelled using Steel02 (black dashed line) and SL Model (red dashed line). It is important to note that the braces with a D/t ratio of 63.5 lie outside the calibrated limits of the SL Model. Except for the brace with D/t = 14.3 and F_y= 165 N/mm^2 (also outside the calibrated range) was not simulated. Despite this, the SL Model demonstrated sufficient accuracy in capturing the force-deformation response within the calibrated range of D/t ratios, slenderness ratios, and yield strength. Table 7.5 compares the post-buckling strengths predicted by numerical models in the last loading cycle with test. Numerical model with and without degradation, the post buckling strength was in the range 0.7-4.5 times the post buckling strength observed in test response. Noticeable difference was observed in specimen with KL/r = 16, D/t =31, KL/r = 16, D/t = 40, and KL/r = 40, D/t = 40, in which numerical model with Steel02 material model predicted post buckling strength approximately 2.7 times that of numerical model with SL model. These findings clearly demonstrate that the proposed fiber model with material degradation (i.e., SL Model) effectively reproduced the post-buckling behavior with improved accuracy.

Based on the comparative study of braces and their stress – strain relationship, the following observations can be made:

1. The SL Model shows limited capability in accurately capturing the Bauschinger effect, as inferred from the steeper slope change when transitioning from tension to

compression in the hysteresis response. This limitation could be addressed by calibration of the isotropic and kinematic hardening parameters using cyclic coupon tests data.

2. The SL Model currently initiates degradation based on capping stress values. However, numerical simulation suggest that local buckling may occur at strain values lower than the capping strain observed in test. Additionally, once degradation begins, the rate of strength deterioration increases in subsequent cycles. This issue could be resolved by modifying the degradation initiation criterion to rely on capping strain rather than capping stress.

3. Further calibration of cyclic parameters based on normalised D/t is necessary, as it governs the pinching effect observed following the onset of local buckling.

4. The Steel02 model tends to overestimate the post buckling response for braces with parameters (D/t = 40, KL/r = 16), (D/t = 31, KL/r = 15.8), (D/t = 40, KL/r = 40). This discrepancy occurs in cases where local buckling followed by global buckling.

7.4 Application of SL Model to Braced frame

To study the effect of the SL Model on the response of a braced frame, the Chevron-braced frame previously designed by Dias (2023) was analyzed. This frame was designed according to U.S. provisions, with lateral loads primarily resisted by the chevron braces.

The beams were proportioned as simply supported members, designed to remain elastic under both tension and compression forces from the braces. The configuration of the 8-story chevron-braced building is shown in Figure 7.12.

In the numerical modelling, columns were modeled using four displacement-based elements with pinned supports, and a P-Delta transformation was applied to account for second-order effects. Beams were modeled as a single element with five integration points, utilizing the Gauss-Lobatto quadrature rule. Braces incorporated corotational transformations to account for geometric nonlinearity. Each flange or web of the beam was subdivided into eight fibers (four in the width direction and two in the thickness direction). Floor diaphragms were represented using elastic truss elements with cross-sectional areas equivalent to the corresponding beam areas. Panel zones were not explicitly modeled; instead, rigid link elements were used to simulate the panel zones. These rigid links were modeled as elastic beam-column elements with cross-sectional areas and moments of inertia 10 times greater than the adjacent structural members (beams, columns, and braces). This setup ensured the numerical model accurately represented the physical behavior of the frame while simplifying the computational complexity of panel zone modelling, the numerical scheme is illustrated in Figure 7.13.

7.5 Response to pushover analysis

A pushover analysis was performed on the braced frame models to evaluate their performance and understand the response of individual members. The nonlinear analysis applied lateral loads incrementally up to a target roof drift of 0.04 radians, following the Ai rule distribution specified in the Japanese Building Standard Law. The results indicated that story drifts were concentrated in the bottom three stories when the Steel02 material was used for braces and in the bottom four stories when the SL model was implemented, while the upper stories remained predominantly elastic, as shown in Figure 7.14. Higher floors show sudden drops in base shear, likely indicating numerical instability may have arisen from incorrect material properties which needs further investigation into material calibration, and further refinements.

7.6 Conclusions

This chapter evaluates modelling techniques for the hysteresis response of circular braces under cyclic loading, considering both material and geometric nonlinearity. A comparative study between two fiber-based numerical models: (1) a non-degrading material model based on Steel02 material model (Filippou, Popov, and Bertero 1983), (2) a calibrated degrading material model based on SL Model material model (Suzuki and Lignos 2020). The performance of these material models is evaluated against the test data of round-HSSs with KL/r = 15.8 - 103 and D/t = 16 - 63, respectively.

Key findings are as follows:

1. Based on limited numerical simulation, the Steel02 material model tends to overestimate the post-buckling responses for the braces with $D/t < 40$, $KL/r < 40$.

2. SL Model can effectively simulate the hysteresis response of round-HSS braces, accounting for both stiffness and strength degradation. The material parameters for SL Model were obtained from monotonic calibration and adjusted for cyclic response. The material model was implemented to simulate round-HSS braces with KL/r ratios ranging from 15.8 to 103 and D/t ratios ranging from 16 to 63.
3. The applicable range of the SL Model for round HSS is as follows: $19 \leq D/t \leq 57$ for the yield strength range of BCR295 (357-454).

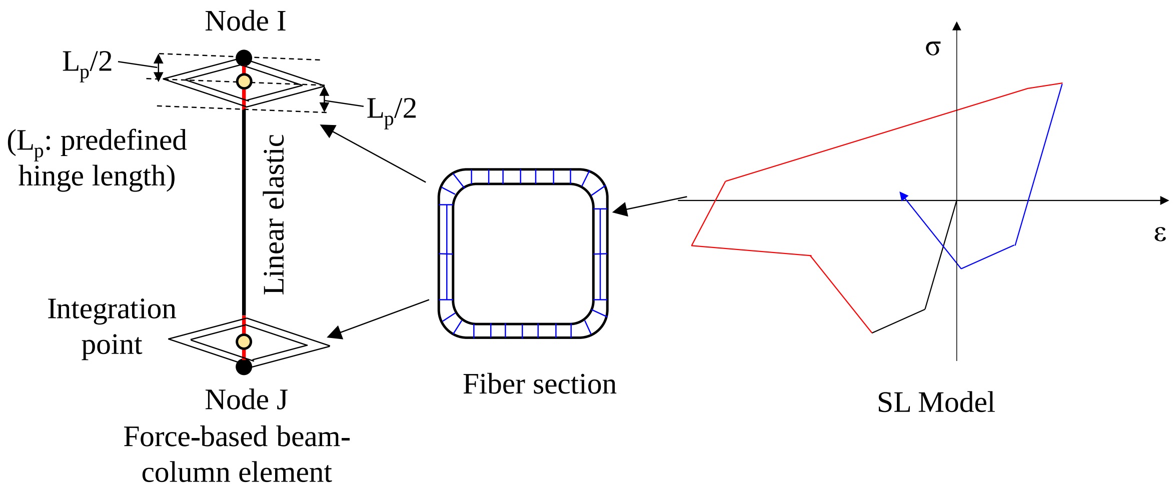

Figure 7.1 Beam-column element schematics (based on Suzuki and Lignos 2020)

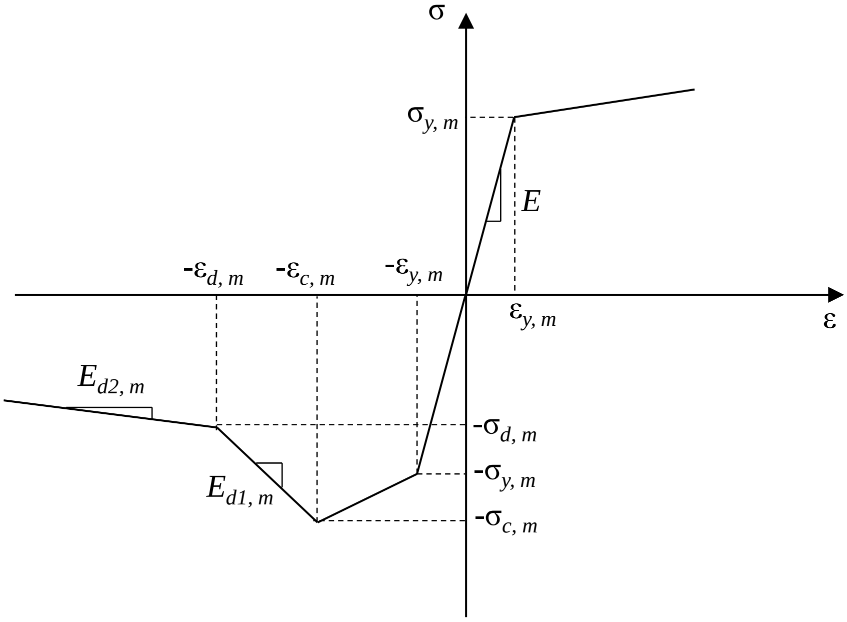

(a)

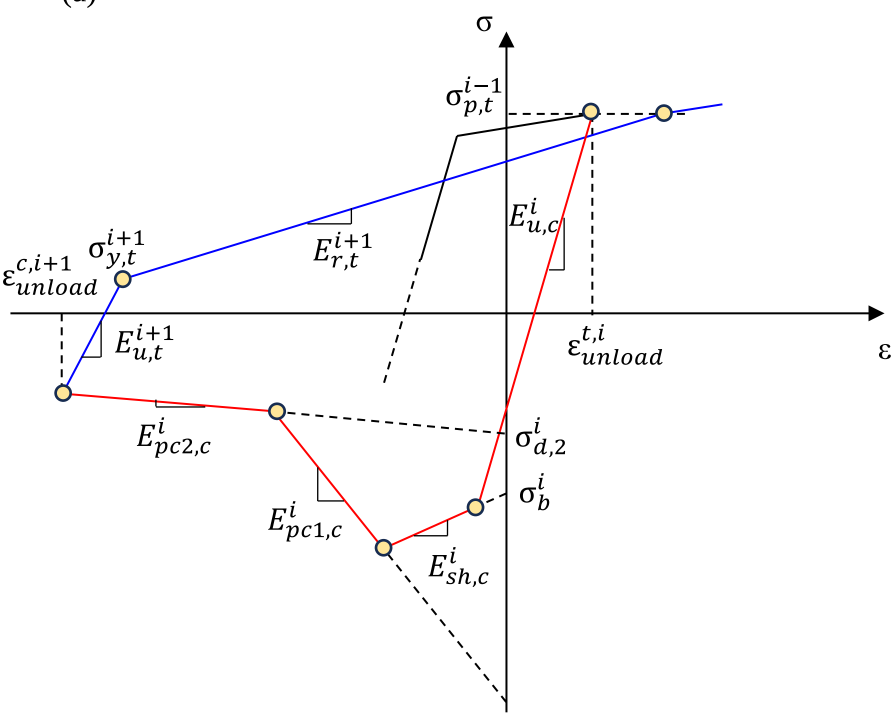

(b)

Figure 7.2 Stress strain curve for cyclic post-buckling stage (based on Suzuki and Lignos 2020)

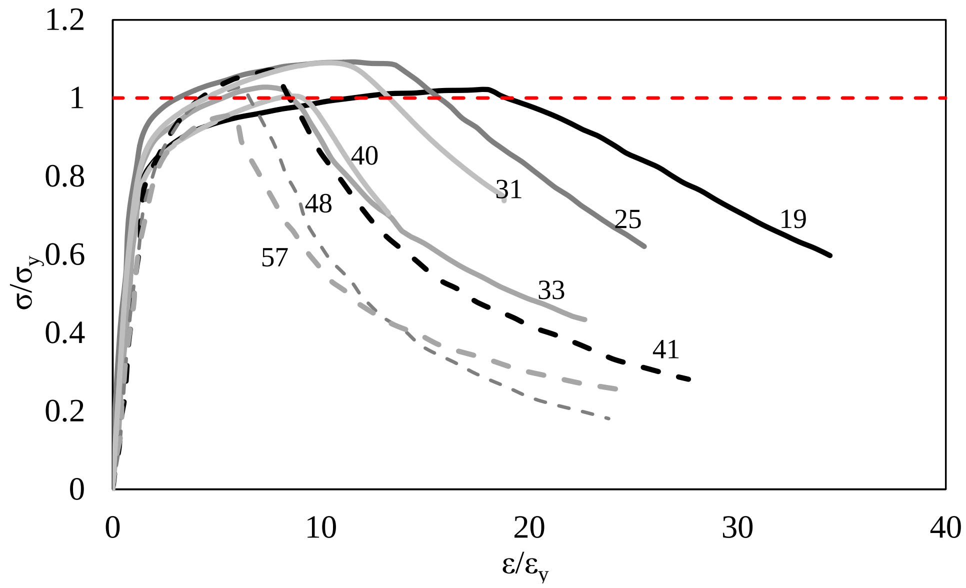

Figure 7.3 Normalised stress strain curve for stub column of various slenderness ratio

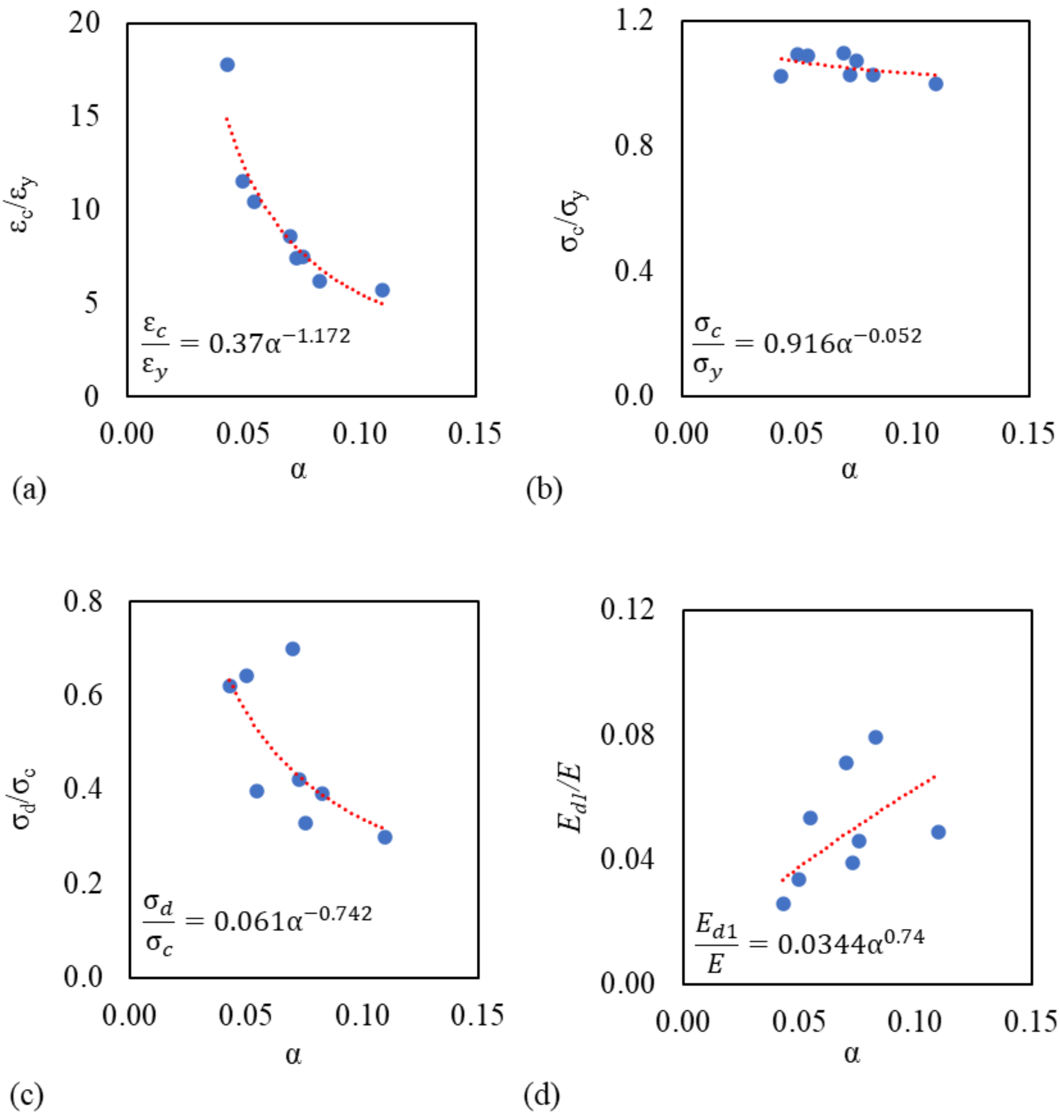

Figure 7.4 Variation of monotonic material parameters with respect to normalised *D*/*t* ratios

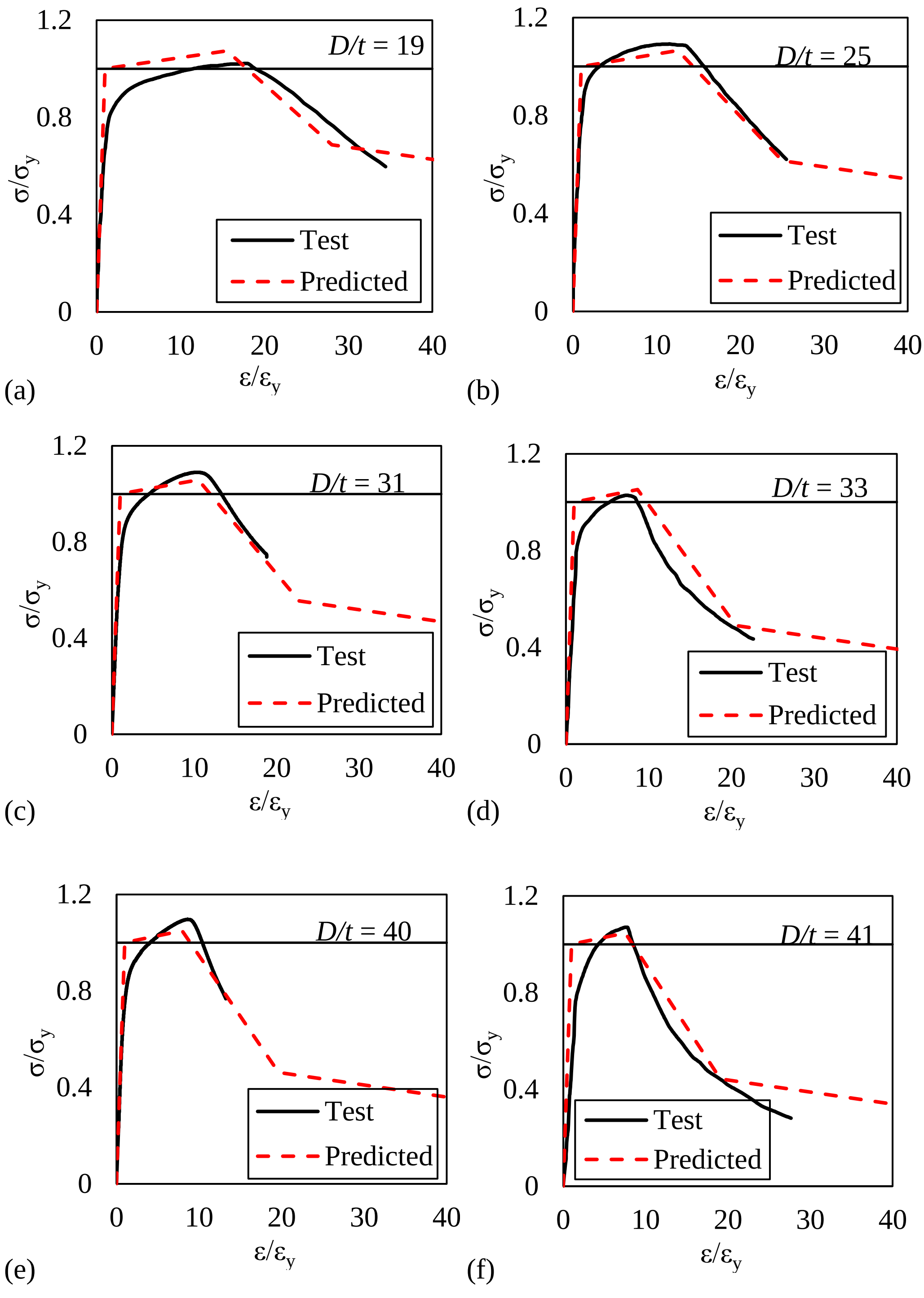

Figure 7.5 Comparison of stress – strain curve between experiment and predicted for various D/t ratios: (a) *D*/*t* = 19; (b) *D*/*t* = 25; (c) *D*/*t* = 31; (d) *D*/*t* = 33; (e) *D*/*t* = 40; (f) *D*/*t* = 41. (continued)

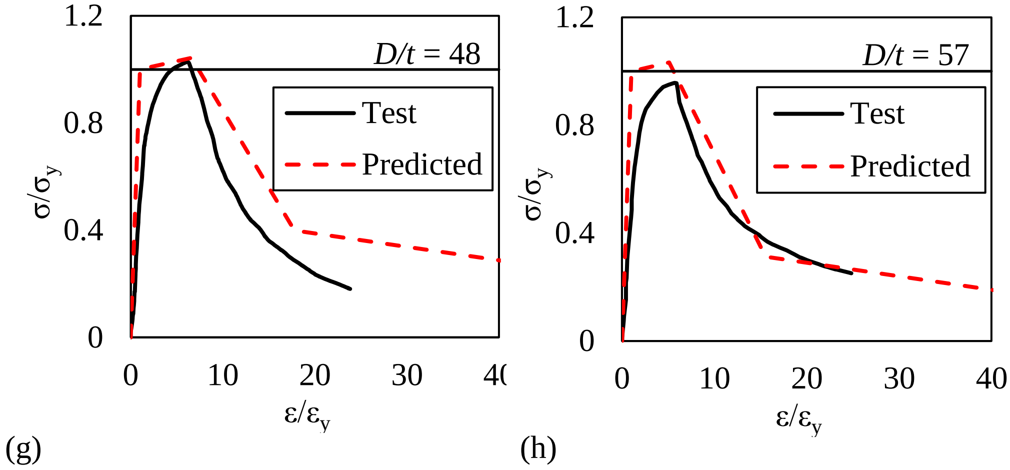

Figure 7.6 Comparison of stress – strain curve between experiment and predicted for various D/t ratio: (g) *D/t* = 48; and (h) *D/t* = 57.

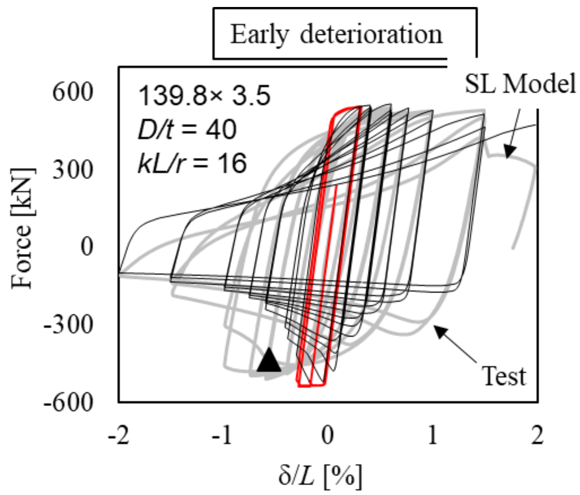

(a)

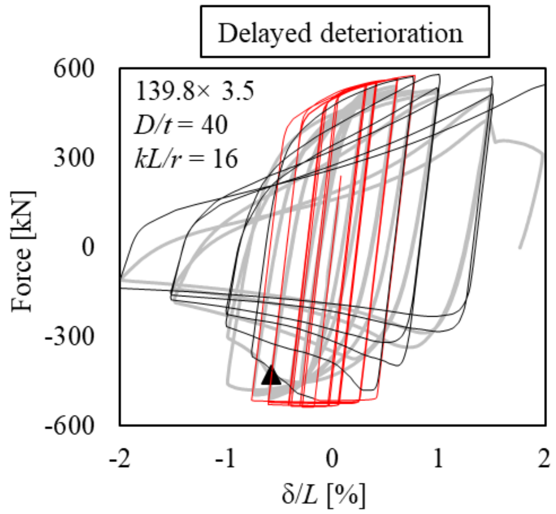

(b)

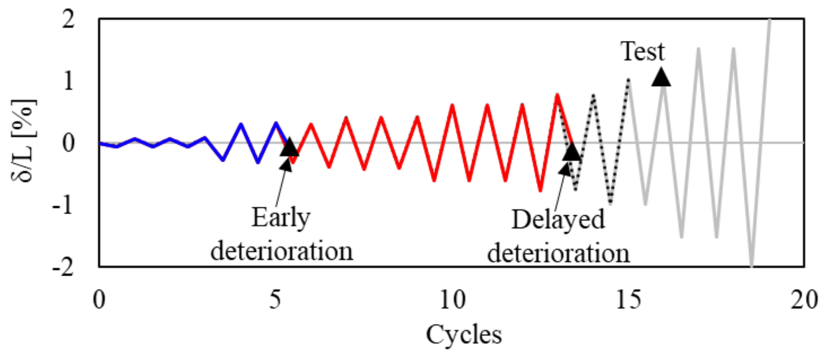

(c)

Figure 7.7 Comparison of force – deformation response for brace (a) without modification factor; (b) with modification factor; (c) Cycles vs. normalised loading protocol showing local buckling instance.

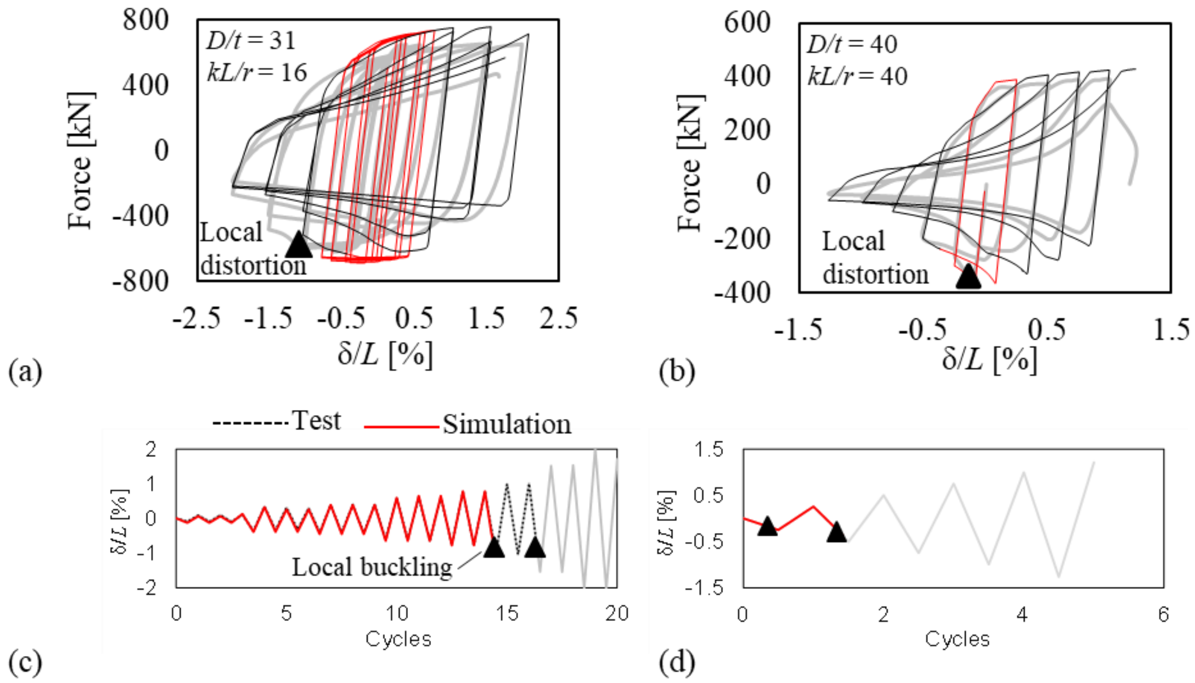

Figure 7.8 Comparison of force – deformation response for brace (a) D/t = 31, KL/r = 15.8 ; (b) D/t = 40, KL/r = 40; Cycles vs. normalised loading protocol showing local buckling instance for (c) D/t = 31, KL/r = 15.8, (d) D/t = 40, KL/r = 40

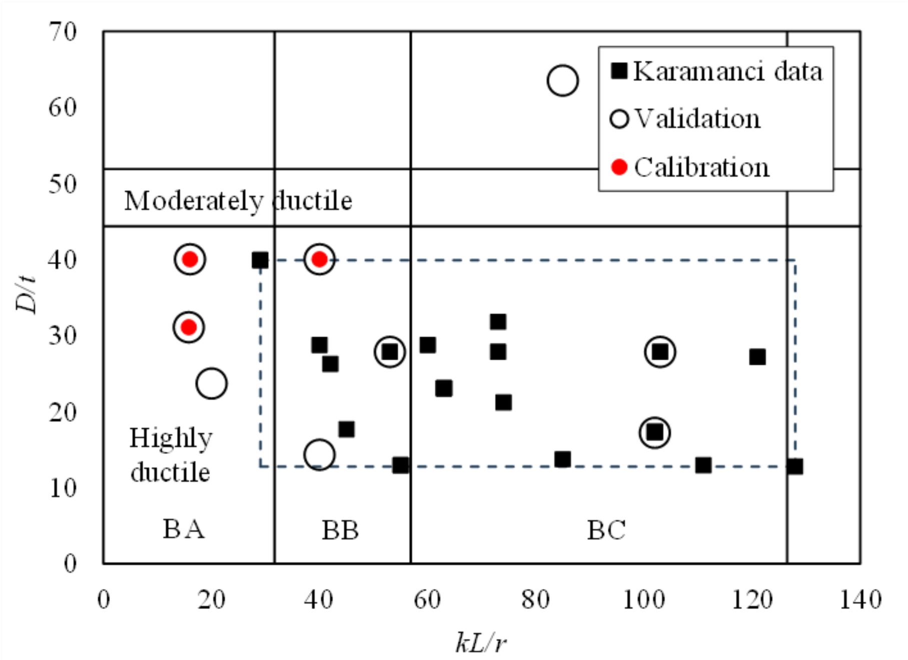

Figure 7.9 Slenderness and compactness ratio of selected braces

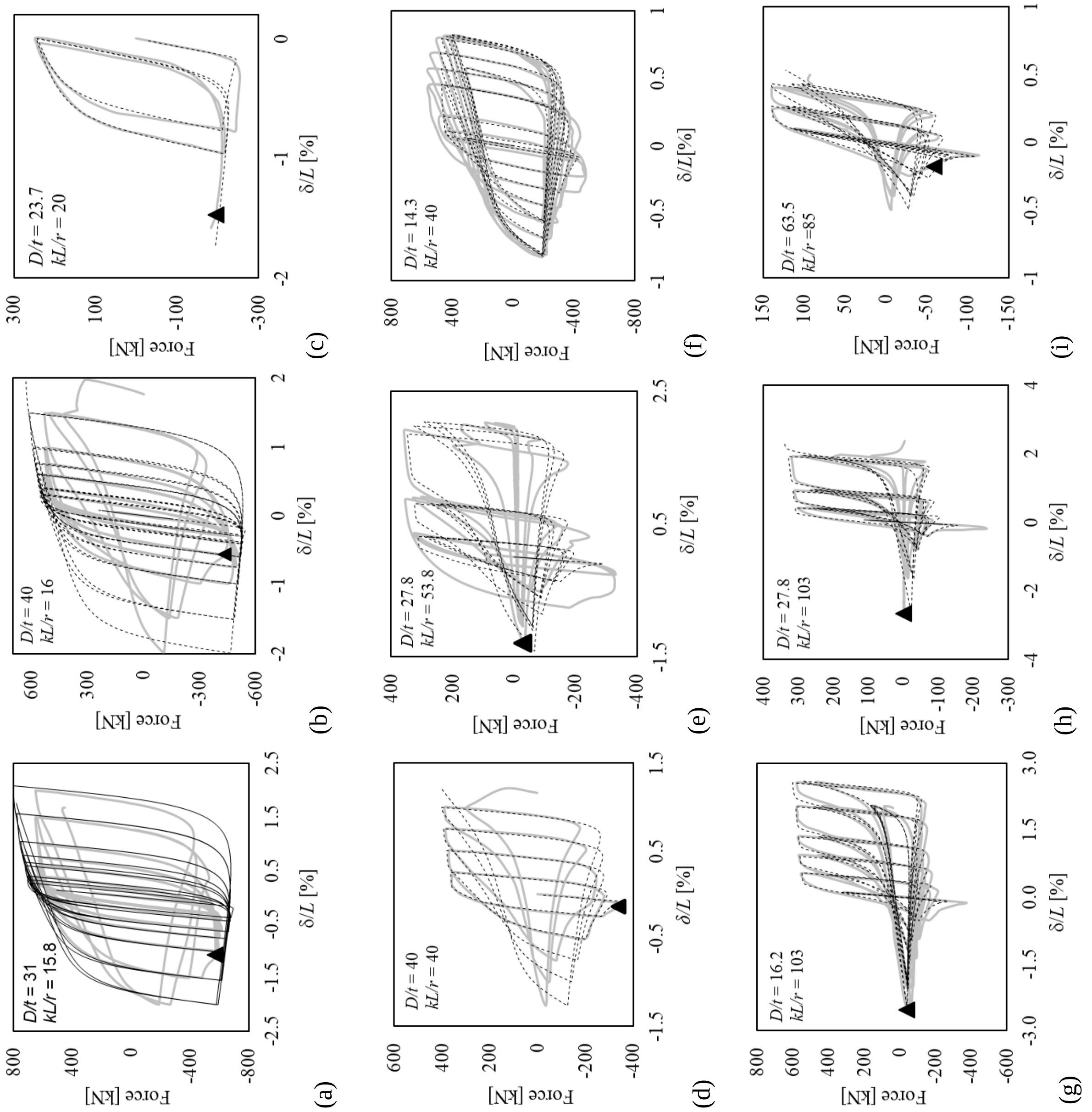

Figure 7.10 Comparison of force – deformation response of test (grey) with Steel02 material model (red): (a) D/t = 31 KL/r = 15.8; (b) D/t = 40 KL/r = 16; (c) D/t = 23.7 KL/r = 20; (d) D/t = 40 KL/r = 40; (e) D/t = 27.8 KL/r = 53.8; (f) D/t = 14.3 KL/r = 40; (g) D/t = 16.2 KL/r = 103; (h) D/t = 27.8 KL/r = 103; (i) D/t = 63.5 KL/r = 85 (▲ shows initiation of local distortion in test)

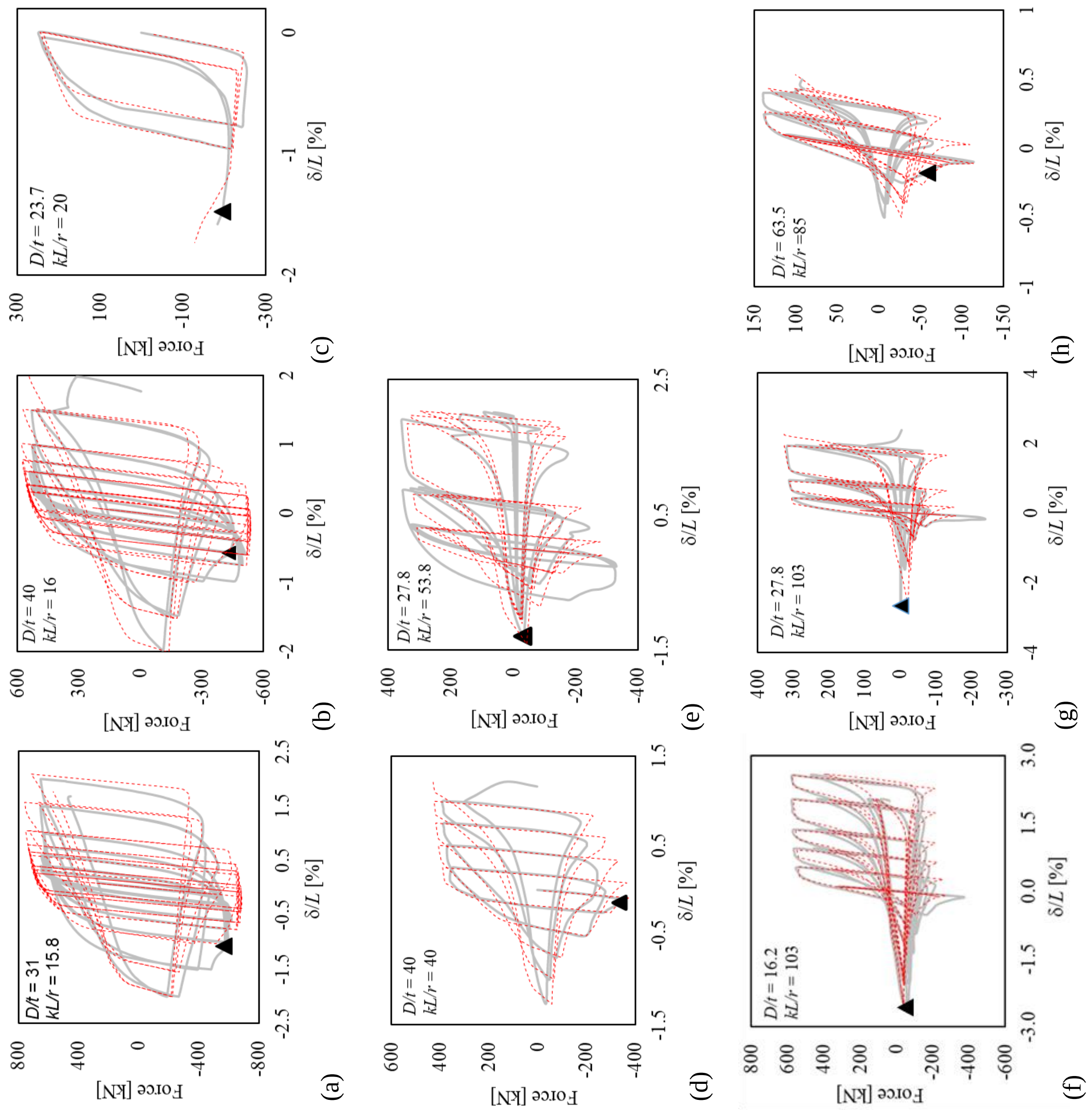

Figure 7.11 Comparison of force – deformation response of test (grey) with SL material model: (a) D/t = 31 KL/r = 15.8; (b) D/t = 40 KL/r = 16; (c) D/t = 23.7 KL/r = 20; (d) D/t = 40 KL/r = 40; (e) D/t = 27.8 KL/r = 53.8; (f) D/t = 16.2 KL/r = 103; (g) D/t = 27.8 KL/r = 103; (h) D/t = 63.5 KL/r = 85 (▲ shows initiation of local distortion in test)

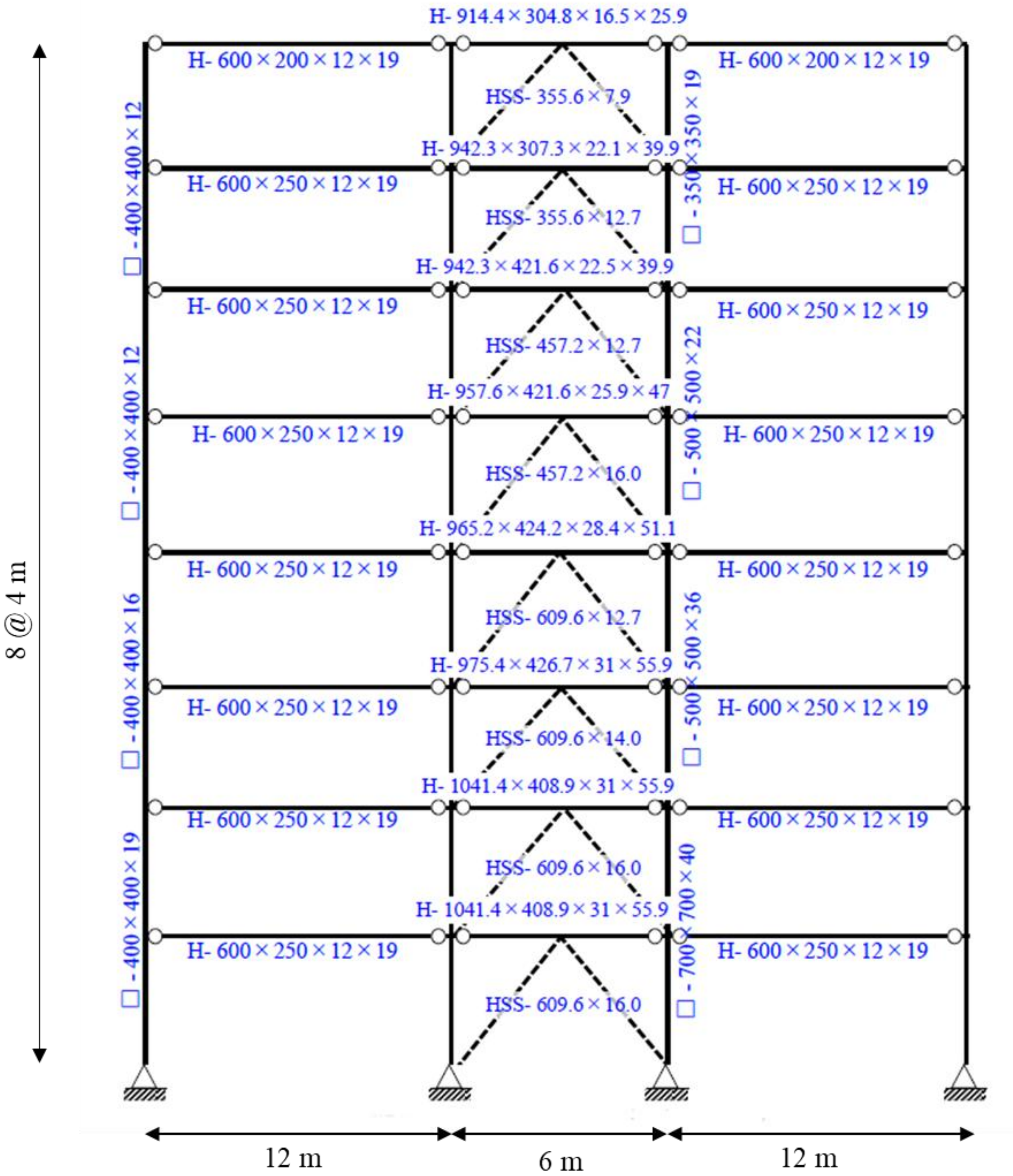

Figure 7.12 8-story chevron building configuration (source: Dias 2023)

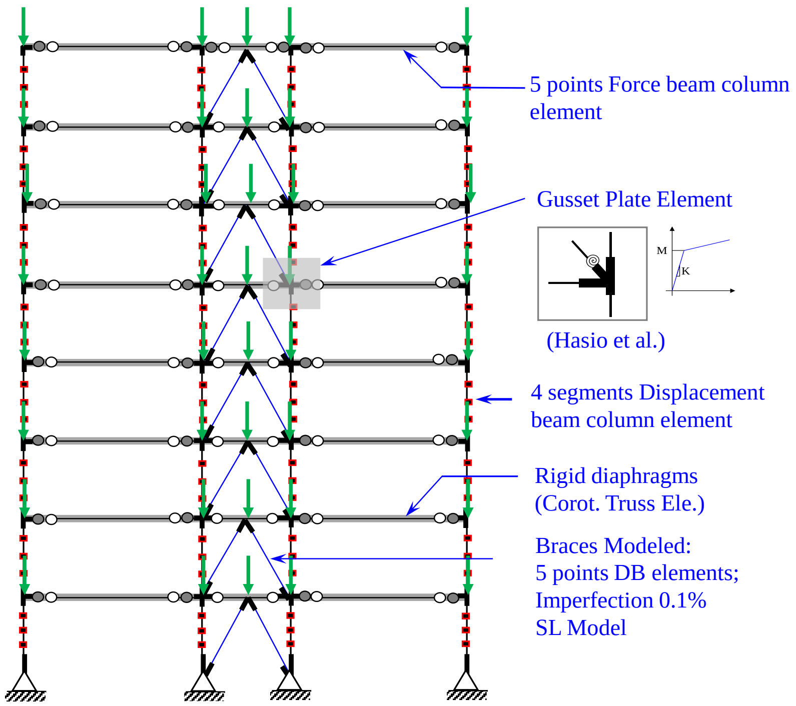

Figure 7.13 Numerical scheme for chevron building modelling

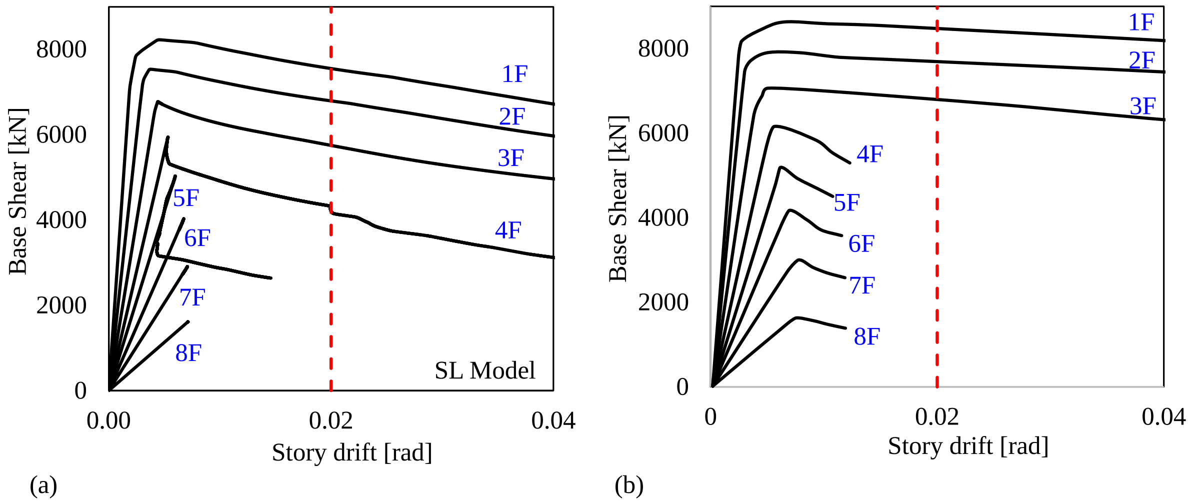

Figure 7.14 Pushover curve for 8 story chevron building employing flexible connection (a) Sl Model; (b) Steel02

Table 7.1 Cyclic hardening parameter for BCR295 (Suzuki and Lignos 2020)

σ_y	C	γ	Q_∞	b
From test	2500	19.0	22.4	7.2

Table 7.2 Dimension and material properties of stub column

No.	Test I.D.	D [mm]	D/t	Measured									Ref.
				σ_y [N/mm²]	σ_u [N/mm²]	σ_c [N/mm²]	ε_y [%]	ε_c [%]	$\frac{\sigma_u}{\sigma_y}$	$\frac{\sigma_c}{\sigma_y}$	$\frac{\varepsilon_u}{\varepsilon_y}$		
1	C1	114.4	19	454	520	461	0.22	3.79	1.15	1.02	17.1		Elchalacani (2002)
2	C2	114.4	25	416	484	443	0.20	2.28	1.16	1.06	11.2		Elchalacani (2002)
3	SC-E1	139.8	31	360	464	400	0.18	1.83	1.29	1.11	10.4		Abe et al. (2023)
4	C3	114.4	33	453	521	459	0.22	1.57	1.15	1.01	7.10		Elchalacani (2002)
5	SC-F1	139.8	40	360	464	395	0.18	1.54	1.29	1.10	8.77		Abe et al. (2023)
6	C5	139.7	41	379	440	399	0.18	1.30	1.16	1.05	7.03		Elchalacani (2002)
7	C6	139.7	48	357	474	362	0.17	1.07	1.33	1.01	6.14		Elchalacani (2002)
8	C8	165.2	57	**395**	481	**374**	0.19	0.96	1.22	**0.95**	4.98		Elchalacani (2002)

Table 7.3 SL material model calibration parameters for round HSS section subjected to monotonic loading

Parameter	σ_c/σ_y	$\varepsilon_c/\varepsilon_y$	E_{d1}/E	σ_d/σ_c	E_{d2}	^	a_σ	a_E
a	0.92	0.37	-0.34	0.061	-0.005E	0.5	0.05	0.05
b	-0.052	-1.17	0.74	-0.742				

E is elastic modulus, $P = a \times \alpha^b$, where P is the parameter

Table 7.4 Test Matrix of steel braces

Sr. No	L [mm]	KL/r	D [mm]	t [mm]	D/t	K	σ_y [MPa]	Reference
BA								
1	1537	16	139.8	4.5	31.07	0.5	360	Abe et al., 2023
2	1537	16	139.8	3.5	40.00	0.5	360	Abe et al., 2023
3	520	20	76.2	3.22	23.66	1	335	Kato, 1977
BB								
4	1930	40	139.8	3.5	40.00	1	254	Hodzumi, 1997
5	1622	53	89.1	3.2	27.81	1	349	Takeuchi et al., 2018
6	2190	40	114	8	14.29	0.65	165	Black et al., 1997
BC								
7	2972	102	89.9	5.48	16.4	1	372	Fell, 2008
8	3135	103	89.1	3.2	27.81	1	349	Takeuchi et al., 2018
9	3006	85	102	1.6	63.50	1	270	Matsui et al. 2018

Table 7.5 Comparison of post buckling strength between test and simulation

Sr. No	KL/r	D/t	σ_y [MPa]	$N_{cr,\ test}$ [kN]	$N_{cr,SL\ Model}$ [kN]	$N_{cr,Steel02}$ [kN]
1	16	31.07	360	187.7	224.0	591.6
2	16	40	360	109.5	137.7	466.7
3	20	23.66	335	182.9	128.1	194.0
4	40	40	254	33.59	57.6	124.8
5	53	27.81	349	34.2	43.1	66.5
6	40	14.29	165	162.34		196.7
7	102	16.4	372	63.01	39.3	41.8
8	103	27.81	349	0.38	21.8	22.9
9	85	63.5	270	6.3	26.8	28.0

8 OBSERVATIONs AND CONCLUSION

8.1 Summary

This research presents a numerical investigation into the dynamic response of a spherical reticulated dome with a 40-m span and 13-m height, serving as a representative model to evaluate the seismic performance of spatial structures. The study validates the applicability of beam-column fiber elements, formulated based on either force or displacement, with segmentations of 2, 4, 8, 10, or 30, for axially loaded members of the dome. The analysis examines how element formulations and damping models influence the vibration displacement response of the dome subjected to Taft ground motion, scaled to 1.3 times the design spectrum specified by Japanese Building Standard Law. Additionally, a seismic risk assessment of the selected dome was conducted using 28 pairs of ground motions, as outlined in FEMA P695 (2009), to explore the broader effects of damping models.

The research also investigates the degradation of strength and stiffness induced by local buckling in stocky axially loaded members, which are commonly used in spatial structures and braced frames. The findings highlight that the failure of stocky braces is frequently governed by local buckling, even when the cross-sectional compactness is within the less ductile or highly ductile range. Existing one-dimensional numerical models face limitations in accurately capturing this local buckling behavior. Consequently, neglecting local buckling in numerical modeling can lead to unrealistic and inaccurate responses, underscoring the importance of considering local buckling in more advanced modeling techniques.

The subsequent sections of the research discuss the main findings and conclude with recommendations and directions for future studies.

8.2 Validation on axially-loaded members of reticulated dome

1. **Effectiveness of Force-Based and Displacement-Based Fiber Elements:** For axially-loaded members commonly used in the reticulated dome, the force-based fiber element with 2 segments was sufficient for tracing the force-displacement relationship. Conversely, displacement-based fiber elements require a minimum of 8

segments to accurately predict the global response of these members, which is influenced by plastic curvature induced by global buckling.

2. **Validation Beyond the Original Range:** Although the slenderness ratios of axially-loaded members in the study were outside the range validated in previous study performed by Uriz et al. (2008), the findings still yielded similar conclusions. This suggests that the fiber-based modeling approach is robust, even different geometric configurations not previously tested, particularly with regard to the force-deformation relationship.

8.3 Seismic risk evaluation of reticulated dome

1. **Elastic Dynamic Response Consistency**: Regardless of the number of segments or the choice of damping models, numerical models using force-based and displacement-based fiber elements consistently predicted identical elastic dynamic responses of the reticulated dome in OpenSees.
2. **Elastic-Plastic Response Sensitivity**: The choice of force formulations, damping models and the number of segments significantly influenced the simulated elastic-plastic response of the reticulated dome, even though the system's plasticity was not extensive. The findings of this research show that commonly employed damping models may behave differently across all the three principal directions. These finding differs with the study by Chopra and Mckenna (2016), which suggested that the influence of damping models on dynamic responses of multi-story frames was limited for the distributed plasticity models. Specifically, the displacement-based fiber element with 8 segments is recommended for reliably estimate both global system and component-level responses in dome structures, while maintaining computational efficiency.
3. **Damping Ratios and Displacement Response**: The average representative damping ratios in all three directions for Rayleigh damping with initial stiffness (Damping Model 5) were 1.26 times the target damping ratio. Rayleigh damping with tangent stiffness (Damping Model 6) and modal damping (Damping Model 12) produced damping ratios nearly identical to the target. Displacement responses computed using Damping Model 6 were 1.1 to 1.2 times higher than those byDamping Model 12, based on the analysis of a suite of ground motions.

Consequently, Damping Model 12 emerged as the most reliable choice among the selected damping models, as it retained consistent damping ratios for higher modes while accurately representing the degradation of the reticulated dome structure.

4. **Nonlinear Time History Analysis Findings**: When the Damping Model 6was used, damage evaluation tended to be most severe compared to Damping Models 5 and 12. Nonlinear time history response analysis subjected to 28 pairs of ground motions indicated that Damping Model 5 has a potential to provide more unconservative evaluation of damage state for spatial structures than Damping Models 6 and 12. Damping Model 12 is recommended for seismic risk analysis to avoid the effects of the spurious damping forces.

8.4 Local buckling induced degradation of steel braces

1. **Limitation of Material Model Without Degradation**: The Steel02 material model demonstrates limitations in capturing the post-buckling responses of the braces with D/t < 40, KL/r < 40

2. **Performance of Material Model with Degradation**: The SL Model effectively simulates hysteresis response of round-HSS braces, accounting for both stiffness and strength degradation. Using material parameters obtained from monotonic calibration and adjusted for cyclic response, the SL Model accurately captured the force–deformation response of round-HSS braces with KL/r ranging from 16 to 103 and D/t ranging from 16 to 63 in this study.

3. The applicable range of the SL Model for round HSS is as follows: $19 \leq {}^{D}/_{t} \leq 57$ for the yield strength range of BCR295 (357-454).

8.5 Recommendations and future work

The research presented in this thesis had several limitations that could not be addressed within the scope of the study. Therefore, future research is necessary to comprehensively understand the performance of the spatial structures. Most of the recommendations outlined here focusing on enhancing the numerical modeling approaches currently available for use.

1. **Broadening the Scope of Structural Analysis**: The present study focused on a specific type of spatial structure. To generalize the findings on element formulations and damping models, future research should investigate a broader range of rise-to-span ratios and substructures to encompass diverse geometric configurations. To better understand the effect on non-structural elements, which are sensitive to acceleration response, future studies should examine the impact of damping models on acceleration behavior. Additionally, since the current study considered only a single ground motion, future work should aim to generalize the findings by incorporating multi-directional seismic excitation.

2. **Seismic Risk Analysis**: Additional seismic risk analyses are required to examine the impact of different damping models on the dynamic responses of the reticulated domes. Fundamentally, the incremental dynamic analysis (IDA) is essential to establish the relationship between the maximum displacement and the scale factor of ground motions. This includes evaluating fiber element strains, the development of plasticity, and overall structural behavior under seismic loading to improve seismic performance assessment of spatial structures. These efforts will contribute more accurate seismic performance assessments of spatial structures. Additionally, effect of slip direction should also be considered in the seismic risk assessment of the reticulated dome.

3. **Enhancing the SL Model**: To improve the accuracy and expend the applicability of the SL Model, several avenues for future research have been identified. The current calibration of the SL Model relies on limited test data. Conducting additional experimental studies on stub columns, combined with virtual simulations for covering a broader range of geometric and material parameters, are essential to refine the model and address the missing range. The SL Model's degradation criteria, depends on capping stress. Future research should modify the algorithm to initiate

degradation based on capping strain, enhancing its ability to replicate observed post-buckling behavior accurately. The calibration of cyclic parameters based on normalised *D/t* ratio. Applying the calibrated SL Model to the reticulated dome structures and braced frames will help investigate the influence of adjacent structural components on the hysteresis response and overall system behavior under cyclic loading. Extending the SL Model to include I-sections would significantly broaden its usability, enabling its application in beam and columns within frame systems. Further calibration of the SL Model to include fracture parameters is necessary to improve its accuracy in capturing failure mechanisms and predicting the ultimate behavior of structural components.

References

ADINA R & D. 2021. “Theory and Modeling Guide Volume I: ADINA Solids & Structures.”

Agüero, A., C. Izvemari, and R. Tremblay. 2006. “Modeling of the Seismic Response of Concentrically Braced Steel Frames Using the Opensees Analysis Environment.” *Advanced Steel Construction* 2 (3): 242–74. https://doi.org/https://doi.org/10.18057/ijasc.2006.2.3.5.

AISC 341. 2022. “Seismic Provisions for Structural Steel Buildings. In Seismic Provisions for Structural Steel Buildings.”

Architectural Institute of Japan (AIJ). 2016. *Recommendation for Design of Latticed Shell Roof Structures*.

Bernal, D. 1994. “Viscous Damping in Inelastic Structural Response.” *Journal of Structural Engineering* 120 (4): 1240–54. https://doi.org/10.1061/(asce)0733-9445(1994)120:4(1240).

Black, R. G., W. A. B. Wenger, and E. P Popov. 1980. “Inelastic Buckling of Steel Struts Under Cyclic Load Reversals.”

Broggiato, G. B., F. Campana, and L. Cortese. 2008. “The Chaboche Nonlinear Kinematic Hardening Model: Calibration Methodology and Validation.” *Meccanica* 43 (2): 115–24. https://doi.org/10.1007/s11012-008-9115-9.

Charney, F. A. 2008. “Unintended Consequences of Modeling Damping in Structures.” *Journal of Structural Engineering* 134 (4): 581–92. https://doi.org/10.1061/(ASCE)0733-9445(2008)134:4(581).

Chopra, A. K. 2012. *Dynamic of Structures*. *Prentice Hall*.

Chopra, A. K., and F. Mckenna. 2016. “Modeling Viscous Damping in Nonlinear Response History Analysis of Buildings for Earthquake Excitation.” *Earthquake Engineering and Structural Dynamics* 45 (2): 193–211. https://doi.org/10.1002/eqe.2622.

Dias, I. 2023. “Seismic Performance and Design of Japanese Steel Chevron Braced Moment Resisting Frames.” *Hokkaido University*. Hokkaido Universtiy.

https://doi.org/10.14943/doctoral.kl15373.

Elchalakani, M., X. Zhao, and R. Grzebieta. 2002. "Tests on Concrete Filled Double-Skin (CHS Outer and SHS Inner) Composite Short Columns under Axial Compression." *Thin-Walled Structures* 40 (5): 415–41. https://doi.org/10.1016/S0263-8231(02)00009-5.

Fan, F., S. Z. Shen, G. A. R. Parke, S. Z. Shen, and G. A. R. Parke. 2005. "Study of the Dynamic Strength of Reticulated Domes under Severe Earthquake Loading." *International Journal of Space Structures* 20 (4): 235–44. https://doi.org/10.1260/026635105775870251.

Fell, B. V., A. M. Kanvinde, G. G. Deierlein, and A. T. Myers. 2009. "Experimental Investigation of Inelastic Cyclic Buckling and Fracture of Steel Braces." *Journal of Structural Engineering* 135 (1): 19–32. https://doi.org/10.1061/(asce)0733-9445(2009)135:1(19).

FEMA P695. 2009. "Quantification of Building Seismic Performance Factors." *Fema P695*.

Filippou, F. C., E. P. Popov, and V. V. Bertero. 1983. "Effects of Bond Deterioriation on Hysteretic Behavior of Reinforced Concrete Joint (EERC 83-19)." *Earthquake Engineering Research Center, University of California, Berkeley*, no. August: 212.

Fragiadakis, M. 2017. "Nonlinear Analysis of Frame Structures under Seismic Loading." *Lecture Notes*, no. October: 150.

Fukutomi, S., T. Okazaki, R. Matsui, and T. Asari. 2020. "Influence of Viscous Damping Model on Time-History Response Analysis of Elastic-Plastic Systems (Part 1): Comparison of Damping Models." *Journal of Structural and Construction Engineering* 85 (778): 1555–63. https://doi.org/10.3130/AIJS.85.1555.

Goggins, J. M., B. M. Broderick, A. Y. Elghazouli, and A. S. Lucas. 2005. "Experimental Cyclic Response of Cold-Formed Hollow Steel Bracing Members." *Engineering Structures* 27 (7): 977–89. https://doi.org/10.1016/j.engstruct.2004.11.017.

Gremer, N., C. Adam, and T. Furtmüller. 2023. "Effect of Damping Model and Inelastic Deformation on the Prediction of Vertical Seismic Acceleration Demand on Steel Frames." *Bulletin of Earthquake Engineering* 21 (1): 207–35. https://doi.org/10.1007/s10518-022-01530-9.

Haddad, M. 2017. “Cyclic Behavior and Finite Element Modeling of Wide Flange Steel Bracing Members.” *Thin-Walled Structures* 111 (October 2016): 65–79. https://doi.org/10.1016/j.tws.2016.11.006.

Hall, J. F. 2006. “Problems Encountered from the Use (or Misuse) of Rayleigh Damping.” *Earthquake Engineering and Structural Dynamics* 35 (5): 525–45. https://doi.org/10.1002/eqe.541.

Hodzumi, H., Y. Makino, M. Sakai, and M. Hirano. 1997. “Studies of Elasto-Plastic Behaviour of Steel Member under Cyclic Axial Force and Its Fracture (No. 1).” *Journal of Structural and Construction Engineering (Transactions of AIJ)* 62 (491): 111–19. https://doi.org/10.3130/aijs.62.111.

Hosseinizad, S A. 2018. “Seismic Response of Lattice Domes.” *Dissertation for the Doctoral Degree*. University of Surrey. https://doi.org/10.1503/cmaj.180710.

Huang, Y., and S. A. Mahin. 2010. “Simulating the Inelastic Seismic Behavior of Steel Braced Frames.” *Pacific Earthquake Engineering Research Center*, no. April.

IASS WG8. 2019. “Guide to Earthquake Response Evaluation of Metal Roof Spatial Structures.” *Report of Activities of IASS WG8*. https://iass-structures.org/resources/Documents/WG Publications and Reports/WG_08/GuideDynamic20200706.pdf.

Ikeda, K., and S. A. Mahin. 1986. “Cyclic Response of Steel Braces.” *Journal of Structural Engineering* 112 (2): 342–61. https://doi.org/10.1061/(asce)0733-9445(1986)112:2(342).

Ikeda, K., S. A. Mahin, and S. N. Dermitzakis. 1984. “Phenomenological Modeling of Steel Braces under Cyclic Loading.” *Rep. No. UCB/EERC-84/09, Earthquake Engineering Research Center*. Berkley, California. https://nehrpsearch.nist.gov/article/PB86-132198/XAB.

Ishikawa, K., and S. Kato. 1997. “Elastic-Plastic Dynamic Buckling Analysis of Reticular Domes Subjected to Earthquake Motion.” *International Journal of Space Structures* 12 (3–4): 205–15. https://doi.org/10.1177/026635119701200309.

Jin, J., and S. El-Tawil. 2003. “Inelastic Cyclic Model for Steel Braces.” *Journal of*

Engineering Mechanics 129 (5): 548–57. https://doi.org/10.1061/(asce)0733-9399(2003)129:5(548).

Karamanci, E., and D. G. Lignos. 2014. "Computational Approach for Collapse Assessment of Concentrically Braced Frames in Seismic Regions." *Journal of Structural Engineering* 140 (8). https://doi.org/10.1061/(asce)st.1943-541x.0001011.

Kato, B., and H. Akiyama. 1977. "Restoring Force Characteristics of Steel Frames Equipped With Diagonal Bracings." *Transactions of the Architectural Institute of Japan*. https://doi.org/10.3130/aijsaxx.260.0_99.

Kato, S., T. Ueki, and Y. Mukaiyama. 1997. "Study of Dynamic Collapse of Single Layer Reticular Domes Subjected to Earthquake Motion and the Estimation of Statically Equivalent Seismic Forces." *International Journal of Space Structures* 12 (3–4): 191–203. https://doi.org/10.1177/026635119701200308.

Kitayama, S., and M. C. Constantinou. 2023. "Effect of Modeling of Inherent Damping on the Response and Collapse Performance of Seismically Isolated Buildings." *Earthquake Engineering and Structural Dynamics* 52 (3): 571–92. https://doi.org/10.1002/eqe.3773.

Lemaitre, J., and J. L. Chaboche. 1991. "Mechanics of Solid Materials." *Cambridge University Press* 28 (08): 28-4548-28–4548. https://doi.org/10.5860/choice.28-4548.

Makowski, Z. S. 1962. "Braced Domes, Their History, Modern Trends and Recent Developments." *Architectural Science Review* 5 (2): 62–79. https://doi.org/10.1080/00038628.1962.9696050.

Matsui, R., T. Nakamura, A. Imamura, and T. Takeuchi. 2018. "Collapse Mechanism of Tower-Supported Steel Stack Composed of Circular Hollow Sections with Large Diameter-to-Thickness Ratio." *Journal of Structural and Construction Engineering* 83 (750): 1171–81. https://doi.org/10.3130/aijs.83.1171.

Matsumoto. 2016. "Experimental Study on the Plastic Deformation Performance of Braces Considering Post-Buckling Behavior - Part 1."

McKenna, F., M. H. Scott, and G. L. Fenves. 2010. "Nonlinear Finite-Element Analysis Software Architecture Using Object Composition." *Journal of Computing in Civil*

Engineering 24 (1): 95–107. https://doi.org/10.1061/(asce)cp.1943-5487.0000002.

Medina, R., and H. Krawinkler. 2004. “Seismic Demands for Nondeteriorating Frame Structures and Their Dependence on Ground Motions.” *Pacific Earthquake Engineering Research Center*, no. May.

MLIT. 2020. “Commentary on Structural Regulations of the Building Design Standard Law of Japan. [In Japanese.].”

Nanhai, Z., and Y. Jihong. 2014. “Structural Vulnerability of a Single-Layer Dome Based on Its Form.” *Journal of Engineering Mechanics* 140 (1): 112–27. https://doi.org/10.1061/(asce)em.1943-7889.0000636.

Neuenhofer, A., and F. C. Filippou. 1997. “Evaluation of Nonlinear Frame Finite-Element Models.” *Journal of Structural Engineering* 123 (7): 958–66. https://doi.org/10.1061/(asce)0733-9445(1997)123:7(958).

Nie, G. B., X. D. Zhi, F. Fan, and J. W. Dai. 2014. “Failure Pattern of Singe-Layer Reticulated Dome under Severe Earthquake and Its Shaking Table Test.” *International Journal of Steel Structures* 14 (2): 399–409. https://doi.org/10.1007/s13296-014-2018-9.

Nie, G., C. Zhang, X. Zhi, and J. Dai. 2017. “Damage Quantification, Damage Limit State Criteria and Vulnerability Analysis for Single-Layer Reticulated Shell.” *Thin-Walled Structures* 120 (April 2016): 378–85. https://doi.org/10.1016/j.tws.2017.09.007.

Nonaka, T. 1973. “An Elastic-Plastic Analysis of a Bar under Repeated Axial Loading.” *International Journal of Solids and Structures* 9 (5): 569–80. https://doi.org/10.1016/0020-7683(73)90070-X.

Sadeghi, A. 2004. “Horizontal Earthquake Loading and Linear/Nonlinear Seismic Behaviour of Double Layer Barrel Vaults.” *International Journal of Space Structures* 19 (1): 21–37. https://doi.org/10.1260/026635104322988344.

Shaback, B., and T. Brown. 2003. “Behaviour of Square Hollow Structural Steel Braces with End Connections under Reversed Cyclic Axial Loading.” *Canadian Journal of Civil Engineering* 30 (4): 745–53. https://doi.org/10.1139/l03-028.

Shing, P. S. B., and S. A. Mahin. 1987. “Elimination of Spurious Higher-mode Response in

Pseudodynamic Tests.” *Earthquake Engineering & Structural Dynamics* 15 (4): 425–45. https://doi.org/10.1002/eqe.4290150403.

Suzuki, Y., and D. G. Lignos. 2020. “Fiber-based Hysteretic Model for Simulating Strength and Stiffness Deterioration of Steel Hollow Structural Section Columns under Cyclic Loading.” *Earthquake Engineering & Structural Dynamics* 49 (15): 1702–20. https://doi.org/10.1002/eqe.3324.

Takeuchi, T., and R. Matsui. 2011. “Cumulative Cyclic Deformation Capacity of Circular Tubular Braces under Local Buckling.” *Journal of Structural Engineering* 137 (11): 1311–18. https://doi.org/10.1061/(ASCE)ST.1943-541X.0000380.

Takeuchi, T., and R. Matsui. 2015. “Cumulative Deformation Capacity of Steel Braces under Various Cyclic Loading Histories.” *Journal of Structural Engineering* 141 (7): 1–11. https://doi.org/10.1061/(ASCE)ST.1943-541X.0001146.

Takeuchi, T., T. Ogawa, and T. Kumagai. 2007. “Seismic Response Evaluation of Lattice Shell Roofs Using Amplification Factors.” *Journal of International Association for Shell and Spatial Structures* 48 (3): 197–210. https://www.researchgate.net/publication/289971639_Seismic_response_evaluation_of_lattice_shell_roofs_using_amplification_factors.

Tatemichi, I., T. Hatato, Y. Anma, and S. Fujiwara. 1997. “Vibration Tests on a Full-Size Suspen-Dome Structure.” *International Journal of Space Structures* 12 (3–4): 217–24. https://doi.org/10.1177/026635119701200310.

Tremblay, R. 2002. “Inelastic Seismic Response of Steel Bracing Members.” *Journal of Constructional Steel Research* 58 (5–8): 665–701. https://doi.org/10.1016/S0143-974X(01)00104-3.

Uriz, P., F. C. Filippou, and S. A. Mahin. 2008. “Model for Cyclic Inelastic Buckling of Steel Braces.” *Journal of Structural Engineering* 134 (4): 619–28. https://doi.org/10.1061/(asce)0733-9445(2008)134:4(619).

Uriz, P., and S. A. Mahin. 2008. “Toward Earthquake-Resistant Design of Concentrically Braced Steel-Frame Structures.” *Pacific Earthquake Engineering Research Center*, no. November: 1–401. https://peer.berkeley.edu/publications/2008-08.

Vazna, R. V., and M. Zarrin. 2020. "Sensitivity Analysis of Double Layer Diamatic Dome Space Structure Collapse Behavior." *Engineering Structures* 212 (June). https://doi.org/10.1016/j.engstruct.2020.110511.

Wakabayashi, M., T. Nakamura, M. Shibata, N. Yoshida, and H. Masuda. 1977. "Proceedings of the Sixth World Conference on Earthquake Engineering" Ill: 3188–95.

Wilson, E. L., A. Der Kiureghian, and E. P. Bayo. 1981. "A Replacement for the Srss Method in Seismic Analysis." *Earthquake Engineering & Structural Dynamics* 9 (2): 187–94. https://doi.org/10.1002/eqe.4290090207.

Yamada, S., T. Ishida, and Y. Shimada. 2012. "Hysteresis Model of RHS Columns in the Deteriorating Range Governed by Local Buckling." *Journal of Structural and Construction Engineering (Transactions of AIJ)* 77 (674): 627–36.

Yang, D. B., Y. G. Zhang, and J. Z. Wu. 2010. "Computation of Rayleigh Damping Coefficients in Seismic Time-History Analysis of Spatial Structures." *Journal of the International Association for Shell and Spatial Structures* 51 (164): 125–35. https://www.researchgate.net/publication/290591976_Computation_of_Rayleigh_damping_coefficients_in_seismic_time-history_analysis_of_spatial_structures.

Yang, D., C. Yun, J. Wu, and Y. Yao. 2018. "Seismic Response and Failure Mechanism of Single-Layer Latticed Domes with Steel Columns and Braces as Substructures." *Thin-Walled Structures* 124 (March): 458–67. https://doi.org/10.1016/j.tws.2017.12.038.

Yang, F., X. Zhi, and F. Fan. 2019. "Effect of Complex Damping on Seismic Responses of a Reticulated Dome and Shaking Table Test Validation." *Thin-Walled Structures* 134 (January): 407–18. https://doi.org/10.1016/j.tws.2018.10.025.

Zheng, H. D., and J. Fan. 2019. "Phenomenological Hysteretic Model for Steel Braces Including Inelastic Postbuckling and Low-Cycle Fatigue Prediction." *Journal of Structural Engineering* 145 (6). https://doi.org/10.1061/(asce)st.1943-541x.0002319.

Zhi, X. D., G. B. Nie, F. Fan, and S. Z. Shen. 2012. "Vulnerability and Risk Assessment of Single-Layer Reticulated Domes Subjected to Earthquakes." *Journal of Structural Engineering* 138 (12): 1505–14. https://doi.org/10.1061/(asce)st.1943-541x.0000589.

Zhong, J., J. Zhang, X. Zhi, and F. Fan. 2018. “Identification of Dominant Modes of Single-Layer Reticulated Shells under Seismic Excitations.” *Thin-Walled Structures* 127 (June): 676–87. https://doi.org/10.1016/j.tws.2018.03.004.

Appendix

A.1. Theory of element formulation

Various element formulations are available for the numerical modeling of steel structures, ranging from 3D solid elements to 1D beam-column elements. The choice of formulation depends on several factors, such as computational time, desired global or local response, and other specific requirements. The seismic response of structures is also influenced by the damping model used in numerical modeling. This appendix is based on the lecture notes of Fragiadakis (2017) and provides a discussion on the formulation of 1D elements utilized in the numerical modeling of spherical dome structures in OpenSees, The lecture notes provided valuable insight into understanding the OpenSees framework.

A1.1. Section Stiffness and Section Forces

The structure can be analyzed using either a stiffness-based or force-based approach, allowing the forces in the members to be determined accordingly. The following section outlines the displacement-based and force-based element formulations used for analyzing the nonlinear dynamic response of the structure. It begins by discussing section stiffness and section forces, followed by an explanation of the two formulations.

For an arbitrary section depicted in the Figure A.1, the displacement at any points composed of axial displacement and bending displacement, let *u(x)* represents the axial displacement and *w(x)* represents the vertical displacement, thus the total displacement at any point is given by Eq. (A.1).

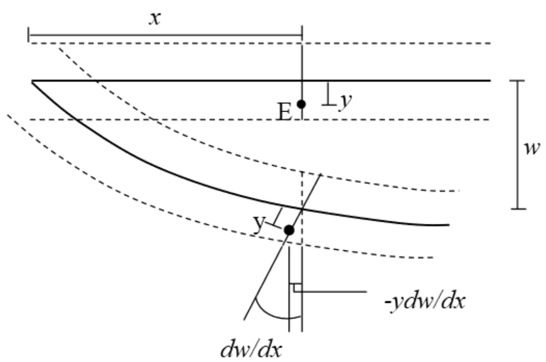

Figure A.1 Section deformation in bending (adapted from Fragiadakis 2017)

$$u(x,y) = u_{axial} + u_{bending} = u(x) - y\frac{dw(x)}{dx} \tag{A.1}$$

Differentiating Eq. (A.1) to get axial strain ε_x.

$$\varepsilon_x(x,y) = \frac{du}{dx} = \frac{du(x)}{dx} - y\frac{d^2w(x)}{d^2x} = e - y\kappa_z \tag{A.2a}$$

$$\varepsilon_x(x,y) = \begin{bmatrix} 1 & -y \end{bmatrix}\begin{bmatrix} e \\ \kappa_z \end{bmatrix} = a_s(x)d_s(x) \tag{A.3b}$$

The same equation in matrix form is represented by ((A.3b), where *e* represents axial strain and κ_z represents section curvature. At a given section both axial force and bending moment will be present, section force is given by (A.4). By differentiating section force by section strain will give section stiffness k_s, given by Eq. (A.5).

$$D_x(x) = \begin{bmatrix} N(x) \\ M(x) \end{bmatrix} \tag{A.4}$$

$$k_s = \frac{\partial D_s}{\partial d_s} = \frac{\partial D_s}{\partial \sigma}\frac{\partial \sigma}{\partial d_s} = \frac{\partial D_s}{\partial \sigma}\frac{\partial \sigma}{\partial \varepsilon}\frac{\partial \varepsilon}{\partial d_s} \tag{A.5}$$

The material constitutive relationship is expressed by the term $\frac{\partial \sigma}{\partial \varepsilon}$, which represents the slope of the uniaxial material law and is equal to Young's modulus, E, for a linear elastic material. To account for the distribution of strain and stress across the section, Eq. (A.5) is integrated to derive the section stiffness. By applying the principle of virtual work, the section stiffness can be calculated as shown below.

$$W_{ext} = W_{int}$$

$$\delta d_s^T D_s = \int_A \delta\varepsilon^T \sigma dA$$

$$\delta d_s^T D_s = \int_A \delta d_s^T a_s^T \sigma dA$$

$$D_s = a_s^T \int_A \sigma dA \tag{A.6}$$

After taking derivative with respect to dA and solving further, the section stiffness is calculated by Eq. (A.7), the section is subdivided into number of layers of equal height, n_{fb}. each fibre has an area A_i located at y_i. To calculate stress and strain at every layer midpoint rule is utilized.

$$dD_s = a_s^T d\sigma$$

$$\frac{dD_s}{d\sigma} = a_s^T$$

$$k_s = \frac{\partial D_s}{\partial \sigma}\frac{\partial \sigma}{\partial \varepsilon}\frac{\partial \varepsilon}{\partial d_s} = \int_A a_s^T \frac{\partial \sigma}{\partial \varepsilon} a_s dA$$

$$k_s = \int_A E(y) a_s^T a_s dA$$

$$k_s = \int_A E(y) a_s^T a_s dA = \int_A E(y) \begin{bmatrix} 1 & -y \\ -y & y^2 \end{bmatrix} dA = \sum_{i=1}^{n_{fb}} E_i A_i \begin{bmatrix} 1 & -y \\ -y & y^2 \end{bmatrix} \tag{A.7}$$

Using virtual work principle, section forces are calculated further. Strain times stress will give the internal work at a given section and, section deformation times section forces will represent external force. Since the stress is not constant throughout the section due to variation in strain, the section forces are calculated by summing forces of each layer, given by Eq. (A.8).

$$W_{ext} = W_{int}$$

$$\delta d_s^T D_s = \int_A \delta\varepsilon^T \sigma dA$$

$$\delta d_s^T D_s = \int_A \delta d_s^T a_s^T \sigma dA$$

$$D_s = \int_A a_s^T \sigma dA$$

$$D_s = \begin{bmatrix} N \\ M_z \end{bmatrix} = \int_A a_s^T \sigma dA = \begin{bmatrix} \int_A \sigma dA \\ \int_A -y\sigma dA \end{bmatrix} = \int_A \begin{bmatrix} 1 \\ -y \end{bmatrix} \sigma dA$$

$$D_s = \begin{bmatrix} N \\ M_z \end{bmatrix} = \int_A a_s^T \sigma dA = \sum_{i=1}^{n_{fb}} \begin{bmatrix} \sigma_i A_i \\ -\sigma_i A_i y_i \end{bmatrix} = \sum_{i=1}^{n_{fb}} \sigma_i A_i \begin{bmatrix} 1 \\ -y_i \end{bmatrix} = \sum_{i=1}^{n_{fb}} a_{s,i}^T \sigma_i A_i \tag{A.8}$$

A1.2. Displacement based beam column element

One of the commonly used element formulations in finite element software is the displacement-based element formulation, widely applied for nonlinear frame elements. In this formulation, the transverse and axial displacements are represented using suitable interpolation functions. For example, cubic Hermitian polynomial shape functions are used for transverse displacement, while linear Lagrange shape functions are employed for axial displacement. These functions provide an exact solution for a linear, elastic prismatic beam, resulting in linear curvature and constant axial force along the element length (Neuenhofer and Filippou, 1997).

In OpenSees, three coordinate systems are utilized: the global coordinate system, the local coordinate system, and the basic (or corotational) coordinate system. The basic coordinate system is attached to the element and accounts for its rigid body motion, separating rigid body effects from strain-inducing quantities (Fragiadakis, 2017). For a planar frame problem, each node has three degrees of freedom (DOFs), resulting in six DOFs in the Cartesian coordinate system and three DOFs in the basic coordinate system. Let v represent the displacement vector in the basic coordinate system; the relationship between section deformation d_s and v is then defined as Eq (A.9):

$$d_s(x) = B_N(x)v \tag{A.9}$$

In 2-dimensional setting the section deformation d_s have dimension 2×1 representing axial and bending deformations. In 3-dimensional setting this is given as 3×1 representing axial and biaxial bending deformations. The deformation vector v in basic system has the dimension 3×1 or 6×1 based on the modelling setting. $B_N(x)$ represents strain displacement transformation matrix, and θ_1 θ_1 and θ_2 are the end rotations in the basic coordinate system of the element, further the deflection due to bending *w(x)* is given by Eq. (A.10).

$$w(x) = \left(x - \frac{2x^2}{L} + \frac{x^3}{L^2}\right)\theta_1 + \left(-\frac{x^2}{L} + \frac{x^3}{L^2}\right)\theta_2 \tag{A.10}$$

Double differentiating transverse displacement $w(x)$ will give curvature κ_z, $B_N(x)$ stores double derivative of the shape function of the beam element and given by Eq. (A.12).

$$\kappa_z = \frac{\partial^2 w}{\partial x^2} = \frac{1}{L}\left[2\left(3\frac{x}{L} - 2\right)\theta_1 + 2\left(3\frac{x}{L} - 1\right)\theta_2\right] \tag{A.11}$$

$$B_N(x) = \frac{1}{L}\begin{bmatrix} 1 & 0 & 0 \\ 0 & 2\left(3\frac{x}{L} - 2\right) & 2\left(3\frac{x}{L} - 1\right) \end{bmatrix} \tag{A.12}$$

Using virtual work principle the equilibrium and stiffness matrix is then calculated

$$W_{basic} = W_{int}$$

$$\delta v^T S = \int_v \delta\varepsilon^T \sigma dV$$

$$= \int_v (a_s \delta d_s)^T C(a_s d_s) dV$$

$$= \int_v \delta d_s{}^T a_s C(a_s d_s) dV$$

$$= \int_L \delta v_T B_N^T \left(\int_A \frac{\partial\sigma}{\partial\varepsilon} a_s^T a_s dA\right) B_N v dL$$

$$= \delta v^T \left(\int_L B_N^T k_s B_N dL\right) v$$

$$\delta v^T S = \delta v^T K_N v$$

$$S = K_N v \tag{A.13}$$

Eq. (A.13) represents the weak form of equilibrium, which satisfies the equilibrium equation on average sense at the nodal points. K_N gives the basic matrix integrated over the element length.

To ensure element is in equilibrium, the element forces are calculated using virtual work principle utilizing Gauss Legendre numerical quadrature.

$$W_{basic} = W_{int}$$
$$\delta v^T S = \int_v \delta\varepsilon^T \sigma dV$$
$$\int_L \left(\int_A \delta\varepsilon^T \sigma dA \right) dL$$
$$\int_L \delta d_s^T \left(\int_A \delta a_s^T \sigma dA \right) dL$$
$$S = \int_L B_N^T D_s dL \tag{A.14}$$

b_e matrix relates forces in the basic system and the cartesian system. Figure A.2 shows the forces for an element in both the system.

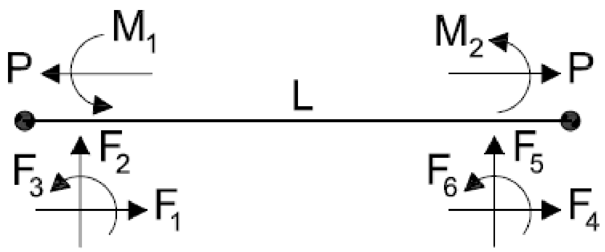

Figure A.2 Forces in basic and cartesian system (source: Fragiadakis 2017)

$$F_1 = -P$$
$$F_2 = \frac{M_1 + M_2}{L}$$
$$F_3 = M_1$$
$$F_4 = P$$
$$F_5 = -\frac{M_1 + M_2}{L}$$
$$F_6 = M_2$$

In matrix form the relationship is written as

$$\begin{bmatrix} F_1 \\ F_2 \\ F_3 \\ F_4 \\ F_5 \\ F_6 \end{bmatrix} = \begin{bmatrix} -1 & 0 & 0 \\ 0 & \frac{1}{L} & \frac{1}{L} \\ 0 & 1 & 0 \\ 1 & 0 & 0 \\ 0 & -\frac{1}{L} & -\frac{1}{L} \\ 0 & 0 & 1 \end{bmatrix} \begin{bmatrix} P \\ M_1 \\ M_2 \end{bmatrix}$$

$$P_e = b_e S$$

In a similar way the relation between deformations in both the coordinate system can be calculated using virtual energy principle.

$$\delta W_{basic} = \delta W_{int}$$
$$\delta v^T S = \delta u_e^T P_e$$
$$\delta v^T S = \delta u_e^T b_e S$$
$$v = b_e^T u_e$$

Further extending to calculate K_e, element stiffness matrix in local coordinate system

$$W_{local} = W_{basic}$$
$$\delta u_e^T P_e = \delta v^T S$$
$$\delta u_e^T K_e u_e = \delta v^T K_N v$$
$$\delta u_e^T K_e u_e = \delta (b_e^T u_e)^T K_N (b_e^T u_e)$$
$$K_e u_e = b_e K_N b_e^T u_e$$
$$K_e = b_e K_N b_e^T$$

Due to straightforward implementation, many finite elements utilize displacement-based element in their finite element package. The one of the limitations of this formulation is that it requires a denser mesh to get the accurate result.

A1.3. Force based beam column element

The force-based element formulation, which follows the flexibility-based approach, offers a significant advantage by allowing the use of a single element per member, unlike the displacement-based elements that often require multiple elements per member. In force-based elements, section forces are derived from nodal forces. Since the force interpolation functions are inherently accurate in the absence of element loads, the constant axial force along the element length and the linear distribution of bending moments enables the use of a single element. This enhances computational efficiency while maintaining accuracy, unlike displacement-based elements, where accuracy depends on the choice of shape functions. In displacement-based formulations, rotations at element ends tend to localize, requiring a denser mesh when sections begin to yield, to achieve comparable accuracy.

Implementing force-based elements in software is more complex than displacement-based elements. In displacement-based formulations, forces are applied, and displacements are directly obtained, with section deformations calculated from nodal deformations, aligning well with most material laws that use strain as input. However, in force-based formulations, an additional iterative step, known as the state determination step, is necessary. This step ensures equilibrium between section forces and nodal forces, making the process more intricate but essential for accurate results.

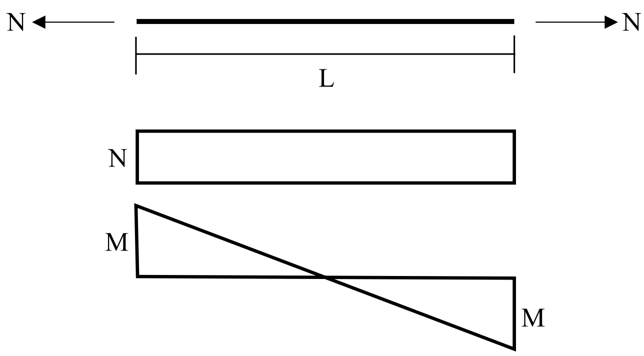

Figure A.3 Forces in basic system

The Figure A.3 shows force interpolation in the basic system, the element basic forces and element basic deformations are denoted as S and v. The section forces D_s at an arbitrary cross section is calculated from element basic forces $S = K_N v$. The element forces are related to section forces by Eqs. (A.15) and (A.16).

$$D_s = b_s(x)S \tag{A.15}$$

$$\begin{bmatrix} N(x) \\ M(x) \end{bmatrix} = \begin{bmatrix} 1 & 0 & 0 \\ 0 & \left(1 - \frac{x}{L}\right) & \frac{x}{L} \end{bmatrix} \begin{bmatrix} N \\ M_1 \\ M_2 \end{bmatrix} \tag{A.16}$$

$b_s(x)$ in the Eq. (A.15) represents force interpolation function. M_1 and M_2 are beam end moments and N is the axial force. In the basic system, the element deformations v are calculated by the use of virtual work principle.

$$W_{basic} = W_{int} \tag{A.17}$$

$$\delta v^T S = \int_L \int_A \delta\varepsilon_x^T \sigma_x dA dx \tag{A.18}$$

$$\int_A \delta\varepsilon_x^T \sigma_x dA = \delta d_s^T \int_A a_s^T \sigma dA = \delta d_s^T D_s = \delta d_s^T b_s(x) S \tag{A.19}$$

$$v = \int_L b_s^T(x) d_s dx \tag{A.20}$$

In the force-based formulation, section deformations are integrated along the element length to account for distributed effects. However, as internal forces are not directly available to verify equilibrium conditions, an additional step known as the element state determination is required. This iterative process ensures equilibrium between the section forces and the nodal forces. The stiffness matrix for the element is computed using the inverse of the basic flexibility matrix, The process of calculating the stiffness matrix is represented by Eq. (A.21).

$$F_N = \frac{\partial v}{\partial S} = \frac{\partial v}{\partial d_s}\frac{\partial d_s}{\partial S} = \frac{\partial v}{\partial d_s}\frac{\partial d_s}{\partial D_s}\frac{\partial D_s}{\partial S}$$

$$F_N = \int_L b_s^T f_s b_s dx \tag{A.21}$$

The F_N in the Eq. (A.21) gives section flexibility matrix $f_s = k_s^{-1}$. The stiffness matrix in the local coordinate system is derived in a manner similar to that of the displacement-based element formulation. In an elastic state, the flexibility matrix is given by Eq. (A.23).

$$K_e = b_e K_N b_e^T \tag{A.22}$$

$$F_N = \int_L b_s^T f_s b_s dx = \begin{bmatrix} \frac{L}{EA} & 0 & 0 \\ 0 & \frac{L}{3EI} & -\frac{L}{6EI} \\ 0 & -\frac{L}{6EI} & \frac{L}{3EI} \end{bmatrix} \tag{A.23}$$

A1.4. Element state determination

The section deformations are obtained in an iterative manner given by Eq. (A.24).

$$\Delta d_s = k_s^{-1} D_s \Rightarrow k_s^{-1} b_s(x) \Delta S$$
$$\Delta d_s = k_s^{-1} b_s(x) F_N \Delta v \tag{A.24}$$

The process starts by calculating the basic force vector S from the Cartesian nodal displacements. Next, the section forces D_s are derived using the force interpolation function and are corrected based on the constitutive law of the fibers. The residual section forces are then multiplied by the section flexibility and integrated along the element length to compute the residual element displacements. The iterative procedure at the element level continues until the residual deformations are minimized, meeting an energy-based convergence criterion. The procedure can be summarized in the following steps.

For every element, initially the increment of the section forces ΔD_s is calculated and then the section deformation d_s are obtained.

$$\Delta d_{s,i}^j(x) = k_s^{-1} \Delta D_{s,i}^j(x)$$
$$\Delta d_{s,i}^j(x) = d_{s,i-1}(x) + \Delta d_{s,i}^j(x) \tag{A.25}$$

The residual forces $D_u(x)$ and residual deformation $r_u(x)$ for every section are calculated using Eq. (A.26), based on the section's deformations, section forces and section stiffness. The section deformations are then integrated to obtain the residual element displacements given by Eq. (A.27). If v_r is not zero, the element displacements v are set to $-v_r$, and the interactions are performed at member level.

$$D_u^j(x) = D_{s,i}^j(x) - D_{s,i}^{j-1}(x)$$

$$r_u^j(x) = k_s^{-1} D_u^j(x) \tag{A.26}$$

$$v_r^j = \int_L b_s(x) r_u^j(x) dx \tag{A.27}$$

Usually, one or two force-based elements are sufficient for modeling; however, increasing the number of integration points or refining the mesh can enhance the accuracy of the force-based formulation (Neuenhofer and Filippou 1997). Despite this, force-based formulations may face localization problems, especially with softening behaviors like cracking in reinforced concrete members. Localization is influenced by the number of integration points and can cause a loss of objectivity; finer discretization can lead to an artificially steep softening curve at the location of plastic moments or damage. In force-based formulations, the plastic hinge length is the distance between the Gauss points near the member ends and adjacent sections. To reduce localization effects, the number of integration points can be selected to better approximate the actual plastic hinge length.

.

A.2. OpenSees Numerical model for brace

```
proc Pipesection {secID matID numSubdivCirc numSubdivRad intRad extRad} {
# Pipesection $secID $matID $intRad $extRad $numSubdivCirc $numSubdivRad
# input parameters
# secID - section ID number
# matID - material ID number
# numSubdivCirc - number of fiber section along circumference
# numSubdivRad - nummber of fiber section along radius
# intRad - internal radius
# extRad - external radius
set SecTagTorsion 200;
set Ubig 1.0e10;  # A large number
uniaxialMaterial Elastic $SecTagTorsion $Ubig
section Fiber  $secID -torsion $SecTagTorsion {
        #           matID  numSubdivCirc  numSubdivRad $y $z intRad extRad
        patch circ $matID $numSubdivCirc $numSubdivRad 0 0 $intRad $extRad
0 360
    }
}


## Units N-mm

wipe
model BasicBuilder -ndm 2 -ndf 3
set Datadir 528-Check;      # set up name of data directory
file mkdir $Datadir;

source Get_Rendering.tcl;

puts "directory defined"

## Nodes
            # 1-2-Rigid offset 2-3-4-5-6 Brace 12-13-Rigid offset 0.01%
initial imperfection
# node 1 0.0 0.0 0.0
# node 2 304.8 0.0 0.0
# node 3 557.9 0.0 0.0
# node 4 811.0 2.0 0.0
# node 5 1064.1 0.0 0.0
# node 6 1317.2 0.0 0.0
# node 7 1622 0.0 0.0
# # extra node for 8 element
# node 8 431.35 0.0 0.0
# node 9 684.45 0.0 0.0
# node 10 937.55 0.0 0.0
# node 11 1190.65 0.0 0.0
# # -------------------------------------------------------------------

# # # 8 elements------------------------------------
node 1 0.0 0.0 0.0
node 2 304.8 0.0 0.0
node 8 431.35 0.0 0.0
node 3 557.9 0.0 0.0
node 9 684.45 0.0 0.0
node 4 811.0 2.0 0.0
node 10 937.55 0.0 0.0
node 5 1064.1 0.0 0.0
node 11 1190.65 0.0 0.0
```

```
node 6 1317.2 0.0 0.0
node 7 1622 0.0 0.0

# ## 10 elements
# node 1 0.0 0.0 0.0
# node 2 304.8 0.0 0.0
# node 3 406.04 0.0 0.0
# node 4 507.28 0.0 0.0
# node 5 608.52 0.0 0.0
# node 8 709.76 0.0 0.0
# node 9 811 2.0 0.0
# node 10 912.24 0.0 0.0
# node 11 1013.48 0.0 0.0
# node 12 1114.72 0.0 0.0
# node 13 1215.96 0.0 0.0
# node 6 1317.2 0.0 0.0
# node 7 1622.0 0.0 0.0


# nodes for 30 element
# node 1 0.0 0.0 0.0
# node 2 304.8 0.0 0.0
# node 3 338.55 0.0 0.0
# node 4 372.3 0.0 0.0
# node 5 406.04 0.0 0.0
# node 6 439.8 0.0 0.0
# node 33 473.54 0.0 0.0
# node 8 507.3 0.0 0.0
# node 9 541.04 0.0 0.0
# node 10 574.8 0.0 0.0
# node 11 608.54 0.0 0.0
# node 12 642.3 0.0 0.0
# node 13 676.04 0.0 0.0
# node 14 709.8 0.0 0.0
# node 15 743.55 0.0 0.0
# node 16 777.3 0.0 0.0
# node 17 811.04 2.0 0.0
# node 18 844.8 0.0 0.0
# node 19 878.54 0.0 0.0
# node 20 912.3 0.0 0.0
# node 21 946.04 0.0 0.0
# node 22 979.8 0.0 0.0
# node 23 1013.54 0.0 0.0
# node 24 1047.3 0.0 0.0
# node 25 1081.04 0.0 0.0
# node 26 1114.8 0.0 0.0
# node 27 1148.54 0.0 0.0
# node 28 1182.3 0.0 0.0
# node 29 1216.04 0.0 0.0
# node 30 1249.8 0.0 0.0
# node 31 1283.54 0.0 0.0
# node 32 1317.3 0.0 0.0
# node 7 1622.0 0.0 0.0

puts "node defined"

## Mass
mass 7 1.0 0.0 0.0

puts "mass defined"
```

```
#Boundary Conditions
fix 1 1 1
fix 7 0 1

puts "boundary condition defined"

## Materials

#uniaxialMaterial Steel01 $matTag $Fy $E0 $b <$a1 $a2 $a3 $a4>
#uniaxialMaterial Steel01 1 24.0 29000.0 0.01

uniaxialMaterial Steel02 1 349 205000 0.001 25 0.925 0.15 0.0005 0.01
0.0005 0.01

##uniaxialMaterial Fatigue $matTag $tag <-E0 $E0> <-m $m> <-min $min> <-max
$max>
#uniaxialMaterial Fatigue 300 1 -E0 0.05 -m -0.458

## Pipe Section
#patch circ $matTag $numSubdivCirc $numSubdivRad $yCenter $zCenter $intRad
$extRad $startAng $endAng
set SecTagTorsion 200;
set Ubig 1.0e10;  # A large number
uniaxialMaterial Elastic $SecTagTorsion $Ubig
section fiberSec 1 -torsion $SecTagTorsion {
patch circ 1 20 16 0.0 0.0 41.35 44.55 0 360.0
}

puts "material defined"

## Transformation
geomTransf Corotational 1

## Define Model
#element elasticBeamColumn $eleTag $iNode $jNode $A $E $Iz $transfTag
#element nonlinearBeamColumn $eleTag $iNode $jNode $numIntgrPts $secTag
$transfTag
set np 5

# # 4 elements---------------------------------------------------------------
----------------------
# element elasticBeamColumn 1 1 2 1.00E+03  1.00E+08    1.00E+06    1   ;#
'Rigid' offset
# element forceBeamColumn 2 2 3 $np 1 1 ;# Brace
# element forceBeamColumn 3 3 4 $np 1 1 ;# Brace
# element forceBeamColumn 4 4 5 $np 1 1 ;# Brace
# element forceBeamColumn 5 5 6 $np 1 1 ;# Brace
# element elasticBeamColumn 6 6 7 1.00E+03  1.00E+08    1.00E+06    1   ;#
'Rigid' offset
# --------------------------------------------------------------------------
------------------------
# # 8 elements---------------------------------------------------------------
----------------------
element elasticBeamColumn 1 1 2 1.00E+03    1.00E+08    1.00E+06    1   ;#
'Rigid' offset
element forceBeamColumn 2 2 8 $np 1 1 ;# Brace
element forceBeamColumn 3 8 3 $np 1 1 ;# Brace
element forceBeamColumn 4 3 9 $np 1 1 ;# Brace
element forceBeamColumn 5 9 4 $np 1 1 ;# Brace
element forceBeamColumn 6 4 10 $np 1 1 ;# Brace
element forceBeamColumn 7 10 5 $np 1 1 ;# Brace
```

```
element forceBeamColumn 8 5 11 $np 1 1 ;# Brace
element forceBeamColumn 9 11 6 $np 1 1 ;# Brace
element elasticBeamColumn 10 6 7 1.00E+03   1.00E+08    1.00E+06    1    ;#
'Rigid' offset
# # ---------------------------------------------------------------------------
--------------------------
# # 10 elements
# element elasticBeamColumn 1 1 2 1.00E+03  1.00E+08    1.00E+06    1    ;#
'Rigid' offset
# element forceBeamColumn 2 2 3 $np 1 1 ;# Brace
# element forceBeamColumn 3 3 4 $np 1 1 ;# Brace
# element forceBeamColumn 4 4 5 $np 1 1 ;# Brace
# element forceBeamColumn 5 5 8 $np 1 1 ;# Brace
# element forceBeamColumn 6 8 9 $np 1 1 ;# Brace
# element forceBeamColumn 7 9 10 $np 1 1 ;# Brace
# element forceBeamColumn 8 10 11 $np 1 1 ;# Brace
# element forceBeamColumn 9 11 12 $np 1 1 ;# Brace
# element forceBeamColumn 10 12 13 $np 1 1 ;# Brace
# element forceBeamColumn 11 13 6 $np 1 1 ;# Brace
# element elasticBeamColumn 12 6 7 1.00E+03 1.00E+08    1.00E+06    1    ;#
'Rigid' offset
#----------------------------------------------------------------------------
--------------------------

# # 30 elements-------------------------------------------------------------
-----------------------
# element elasticBeamColumn 1 1 2 1.00E+03  1.00E+08    1.00E+06    1    ;#
'Rigid' offset
# element forceBeamColumn 2 2 3 $np 1 1 ;# Brace
# element forceBeamColumn 3 3 4 $np 1 1 ;# Brace
# element forceBeamColumn 4 4 5 $np 1 1 ;# Brace
# element forceBeamColumn 5 5 6 $np 1 1 ;# Brace
# element forceBeamColumn 6 6 33 $np 1 1 ;# Brace
# element forceBeamColumn 7 33 8 $np 1 1 ;# Brace
# element forceBeamColumn 8 8 9 $np 1 1 ;# Brace
# element forceBeamColumn 9 9 10 $np 1 1 ;# Brace
# element forceBeamColumn 10 10 11 $np 1 1 ;# Brace
# element forceBeamColumn 11 11 12 $np 1 1 ;# Brace
# element forceBeamColumn 12 12 13 $np 1 1 ;# Brace
# element forceBeamColumn 13 13 14 $np 1 1 ;# Brace
# element forceBeamColumn 14 14 15 $np 1 1 ;# Brace
# element forceBeamColumn 15 15 16 $np 1 1 ;# Brace
# element forceBeamColumn 16 16 17 $np 1 1 ;# Brace
# element forceBeamColumn 17 17 18 $np 1 1 ;# Brace
# element forceBeamColumn 18 18 19 $np 1 1 ;# Brace
# element forceBeamColumn 19 19 20 $np 1 1 ;# Brace
# element forceBeamColumn 20 20 21 $np 1 1 ;# Brace
# element forceBeamColumn 21 21 22 $np 1 1 ;# Brace
# element forceBeamColumn 22 22 23 $np 1 1 ;# Brace
# element forceBeamColumn 23 23 24 $np 1 1 ;# Brace
# element forceBeamColumn 24 24 25 $np 1 1 ;# Brace
# element forceBeamColumn 25 25 26 $np 1 1 ;# Brace
# element forceBeamColumn 26 26 27 $np 1 1 ;# Brace
# element forceBeamColumn 27 27 28 $np 1 1 ;# Brace
# element forceBeamColumn 28 28 29 $np 1 1 ;# Brace
# element forceBeamColumn 29 29 30 $np 1 1 ;# Brace
# element forceBeamColumn 30 30 31 $np 1 1 ;# Brace
# element forceBeamColumn 31 31 32 $np 1 1 ;# Brace
# element elasticBeamColumn 32 32 7 1.00E+03    1.00E+08    1.00E+06
1    ;#  'Rigid' offset
```

```
# # ---------------------------------------------------------------------------------------------

puts "elements defined"

## Recorder
#recorder Node -file $Datadir/LoadDisp.out -time -node 7 -dof 1 disp;
recorder Node -file $Datadir/LoadDisp.txt -time -node 7 -dof 1 disp;
#recorder Element -file $Datadir/force.out -time -ele 1 2 localForce;

#recorder Element -file $Datadir/ele_2_sec_def.txt -time -ele all section deformation
#recorder Element -file $Datadir/ele_sec_def.txt -time -ele 2 3 4 5 6 7 8 9 10 11 12 13 14 15 16 17 18 19 20 21 22 23 24 25 26 27 28 29 30 31 section deformation
puts "recorder defined"

set modelName 528_30ele;
set loadCaseName Cyclic

# command: createODB "ModelName" "LoadCaseName" Nmodes
#createODB "$modelName" "$loadCaseName" 0

## Apply the nodal Load
pattern Plain 1 Linear { load 7 1.0 0.0 0.0 }

puts "load defined"

## Static Analysis parameters
test EnergyIncr 1.0e-3 100 0
algorithm KrylovNewton
system UmfPack
numberer RCM
constraints Plain
analysis Static

# Cyclic analysis
# integrator    DisplacementControl 7   1   -0.0050 ;   analysis    Static;   analyze 10  ;   puts    "   1   "
# integrator    DisplacementControl 7   1   -0.0050 ;   analysis    Static;   analyze 12  ;   puts    "   2   "
# integrator    DisplacementControl 7   1   0.0050  ;   analysis    Static;   analyze 179 ;   puts    "   3   "
# integrator    DisplacementControl 7   1   -0.0050 ;   analysis    Static;   analyze 175 ;   puts    "   4   "
# integrator    DisplacementControl 7   1   0.0050  ;   analysis    Static;   analyze 176 ;   puts    "   5   "
# integrator    DisplacementControl 7   1   -0.0050 ;   analysis    Static;   analyze 177 ;   puts    "   6   "
# integrator    DisplacementControl 7   1   0.0050  ;   analysis    Static;   analyze 176 ;   puts    "   7   "
# integrator    DisplacementControl 7   1   -0.0050 ;   analysis    Static;   analyze 1035    ;   puts    "   8   "
# integrator    DisplacementControl 7   1   0.0050  ;   analysis    Static;   analyze 2020    ;   puts    "   9   "
# integrator    DisplacementControl 7   1   -0.0050 ;   analysis    Static;   analyze 2014    ;   puts    "   10  "
# integrator    DisplacementControl 7   1   0.0050  ;   analysis    Static;   analyze 2025    ;   puts    "   11  "
```

```
# integrator    DisplacementControl 7   1   -0.0050 ;   analysis    Static;
analyze 2033    ;   puts    "   12  "
# integrator    DisplacementControl 7   1   0.0050  ;   analysis    Static;
analyze 2039    ;   puts    "   13  "
# integrator    DisplacementControl 7   1   -0.0050 ;   analysis    Static;
analyze 3632    ;   puts    "   14  "
# integrator    DisplacementControl 7   1   0.0050  ;   analysis    Static;
analyze 5298    ;   puts    "   15  "
# integrator    DisplacementControl 7   1   -0.0050 ;   analysis    Static;
analyze 4513    ;   puts    "   16  "
# integrator    DisplacementControl 7   1   0.0050  ;   analysis    Static;
analyze 4582    ;   puts    "   17  "
# integrator    DisplacementControl 7   1   -0.0050 ;   analysis    Static;
analyze 4542    ;   puts    "   18  "
# integrator    DisplacementControl 7   1   0.0050  ;   analysis    Static;
analyze 4590    ;   puts    "   19  "
# integrator    DisplacementControl 7   1   -0.0050 ;   analysis    Static;
analyze 7148    ;   puts    "   20  "
# integrator    DisplacementControl 7   1   0.0050  ;   analysis    Static;
analyze 10411   ;   puts    "   21  "
# integrator    DisplacementControl 7   1   -0.0050 ;   analysis    Static;
analyze 9594    ;   puts    "   22  "
# integrator    DisplacementControl 7   1   0.0050  ;   analysis    Static;
analyze 9848    ;   puts    "   23  "
# integrator    DisplacementControl 7   1   -0.0050 ;   analysis    Static;
analyze 9739    ;   puts    "   24  "
# integrator    DisplacementControl 7   1   0.0050  ;   analysis    Static;
analyze 9838    ;   puts    "   25  "
# integrator    DisplacementControl 7   1   -0.0050 ;   analysis    Static;
analyze 9827    ;   puts    "   26  "
# integrator    DisplacementControl 7   1   0.0050  ;   analysis    Static;
analyze 9798    ;   puts    "   27  "
# integrator    DisplacementControl 7   1   -0.0050 ;   analysis    Static;
analyze 13048   ;   puts    "   28  "
# integrator    DisplacementControl 7   1   0.0050  ;   analysis    Static;
analyze 14419   ;   puts    "   29  "

#increment 0.01
integrator  DisplacementControl 7   1   -0.0100 ;   analysis    Static;
analyze 5   ;   puts    "   1   "
integrator  DisplacementControl 7   1   -0.0100 ;   analysis    Static;
analyze 6   ;   puts    "   2   "
integrator  DisplacementControl 7   1   0.0100  ;   analysis    Static;
analyze 90  ;   puts    "   3   "
integrator  DisplacementControl 7   1   -0.0100 ;   analysis    Static;
analyze 88  ;   puts    "   4   "
integrator  DisplacementControl 7   1   0.0100  ;   analysis    Static;
analyze 88  ;   puts    "   5   "
integrator  DisplacementControl 7   1   -0.0100 ;   analysis    Static;
analyze 89  ;   puts    "   6   "
integrator  DisplacementControl 7   1   0.0100  ;   analysis    Static;
analyze 88  ;   puts    "   7   "
integrator  DisplacementControl 7   1   -0.0100 ;   analysis    Static;
analyze 518 ;   puts    "   8   "
integrator  DisplacementControl 7   1   0.0100  ;   analysis    Static;
analyze 1010    ;   puts    "   9   "
integrator  DisplacementControl 7   1   -0.0100 ;   analysis    Static;
analyze 1007    ;   puts    "   10  "
integrator  DisplacementControl 7   1   0.0100  ;   analysis    Static;
analyze 1013    ;   puts    "   11  "
```

```
integrator  DisplacementControl 7   1   -0.0100 ;   analysis    Static;
analyze 1017    ;   puts    "   12  "
integrator  DisplacementControl 7   1   0.0100  ;   analysis    Static;
analyze 1020    ;   puts    "   13  "
integrator  DisplacementControl 7   1   -0.0100 ;   analysis    Static;
analyze 1816    ;   puts    "   14  "
integrator  DisplacementControl 7   1   0.0100  ;   analysis    Static;
analyze 2649    ;   puts    "   15  "
integrator  DisplacementControl 7   1   -0.0100 ;   analysis    Static;
analyze 2257    ;   puts    "   16  "
integrator  DisplacementControl 7   1   0.0100  ;   analysis    Static;
analyze 2291    ;   puts    "   17  "
integrator  DisplacementControl 7   1   -0.0100 ;   analysis    Static;
analyze 2271    ;   puts    "   18  "
integrator  DisplacementControl 7   1   0.0100  ;   analysis    Static;
analyze 2295    ;   puts    "   19  "
integrator  DisplacementControl 7   1   -0.0100 ;   analysis    Static;
analyze 3574    ;   puts    "   20  "
integrator  DisplacementControl 7   1   0.0100  ;   analysis    Static;
analyze 5206    ;   puts    "   21  "
integrator  DisplacementControl 7   1   -0.0100 ;   analysis    Static;
analyze 4797    ;   puts    "   22  "
integrator  DisplacementControl 7   1   0.0100  ;   analysis    Static;
analyze 4924    ;   puts    "   23  "
integrator  DisplacementControl 7   1   -0.0100 ;   analysis    Static;
analyze 4870    ;   puts    "   24  "
integrator  DisplacementControl 7   1   0.0100  ;   analysis    Static;
analyze 4919    ;   puts    "   25  "
integrator  DisplacementControl 7   1   -0.0100 ;   analysis    Static;
analyze 4914    ;   puts    "   26  "
integrator  DisplacementControl 7   1   0.0100  ;   analysis    Static;
analyze 4899    ;   puts    "   27  "
integrator  DisplacementControl 7   1   -0.0100 ;   analysis    Static;
analyze 6524    ;   puts    "   28  "
integrator  DisplacementControl 7   1   0.0100  ;   analysis    Static;
analyze 7210    ;   puts    "   29  "

puts "analysis done"

wipe
```

A.3. SL Model Flow chart

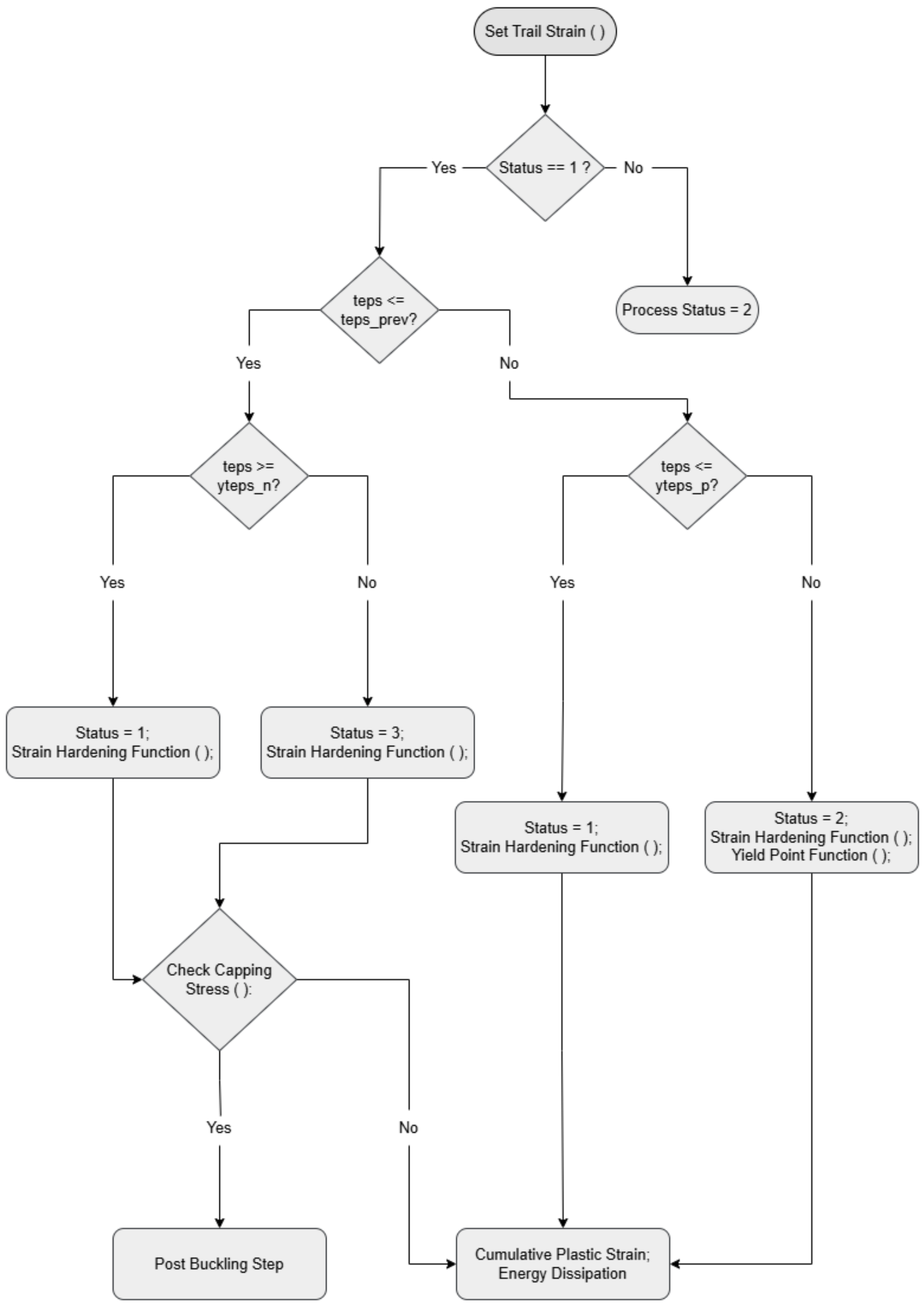

Figure A.4 Pre-buckling stage

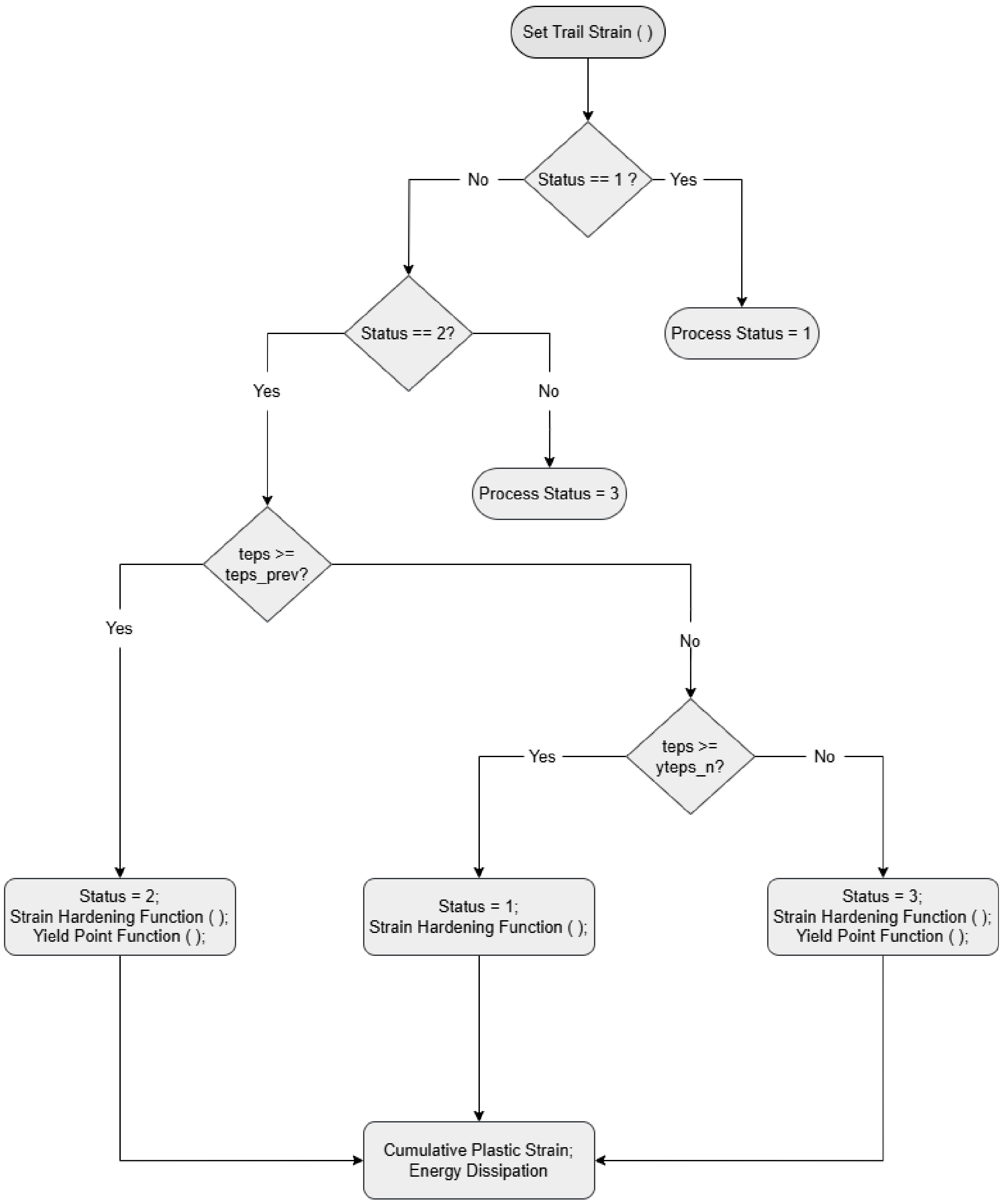

Figure A.5 Pre-buckling stage (continued)

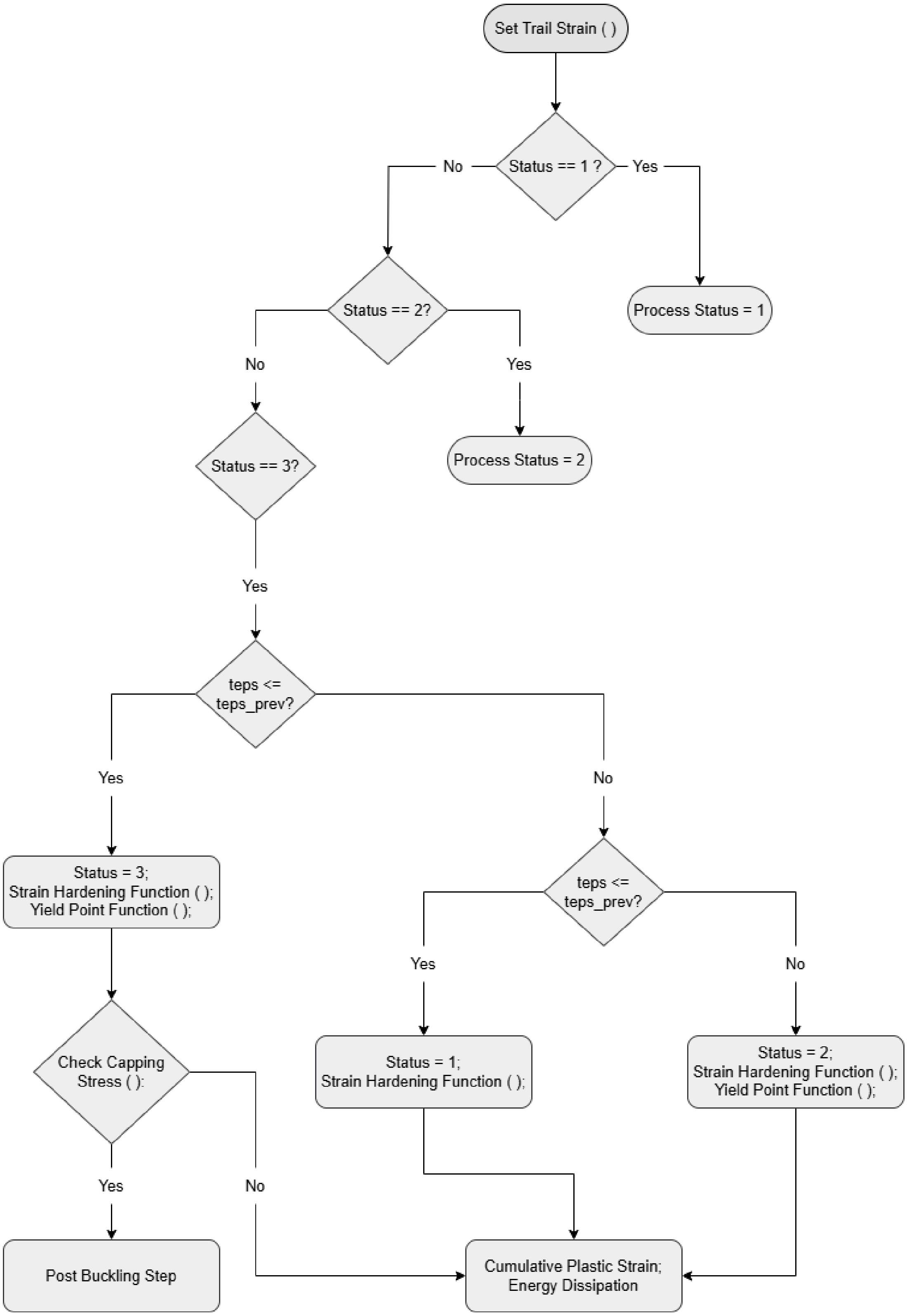

Figure A.6 Pre-buckling stage (continued)

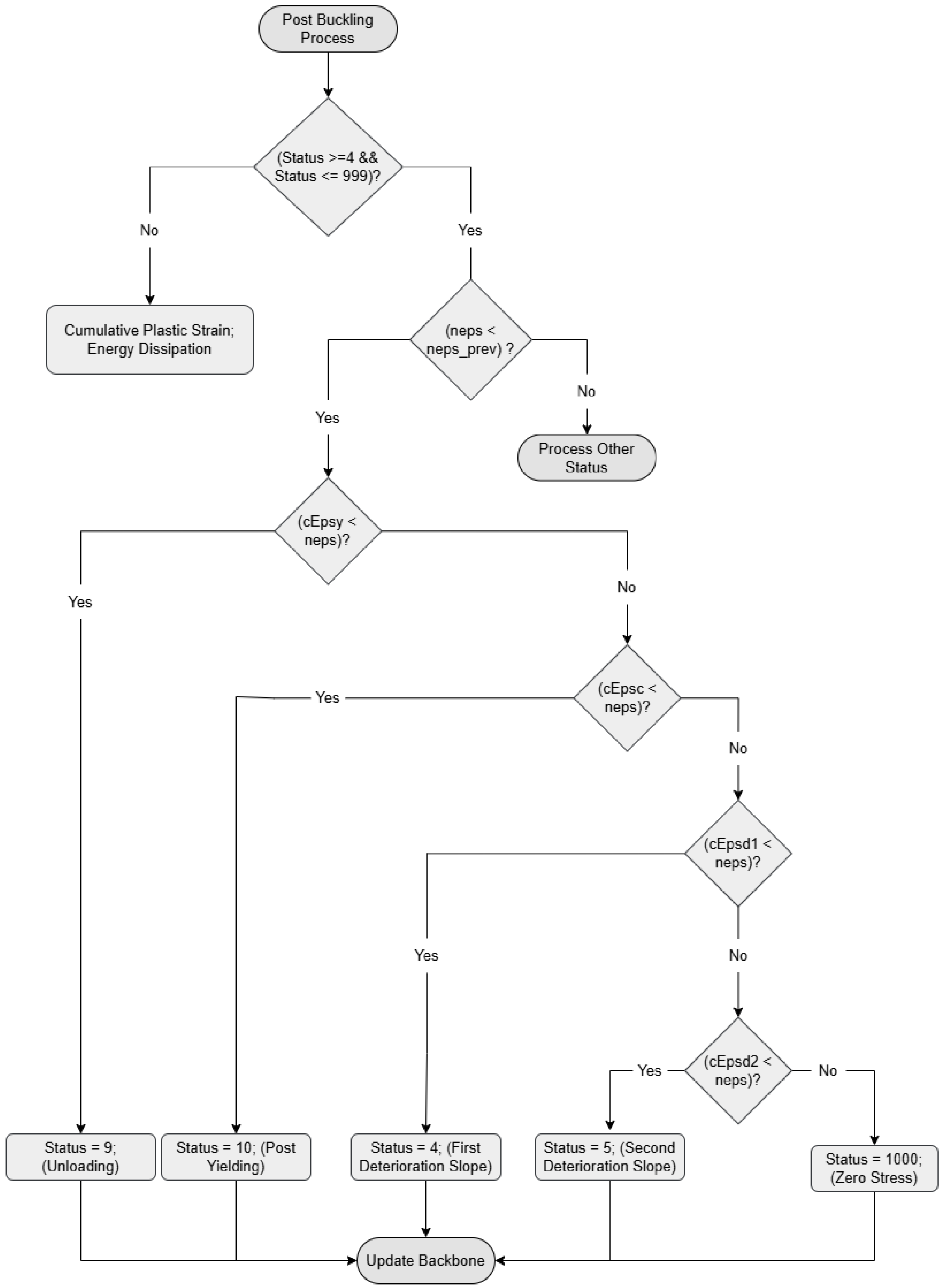

Figure A.7 Post buckling stage (status 9, 10, 4, 5, 1000)

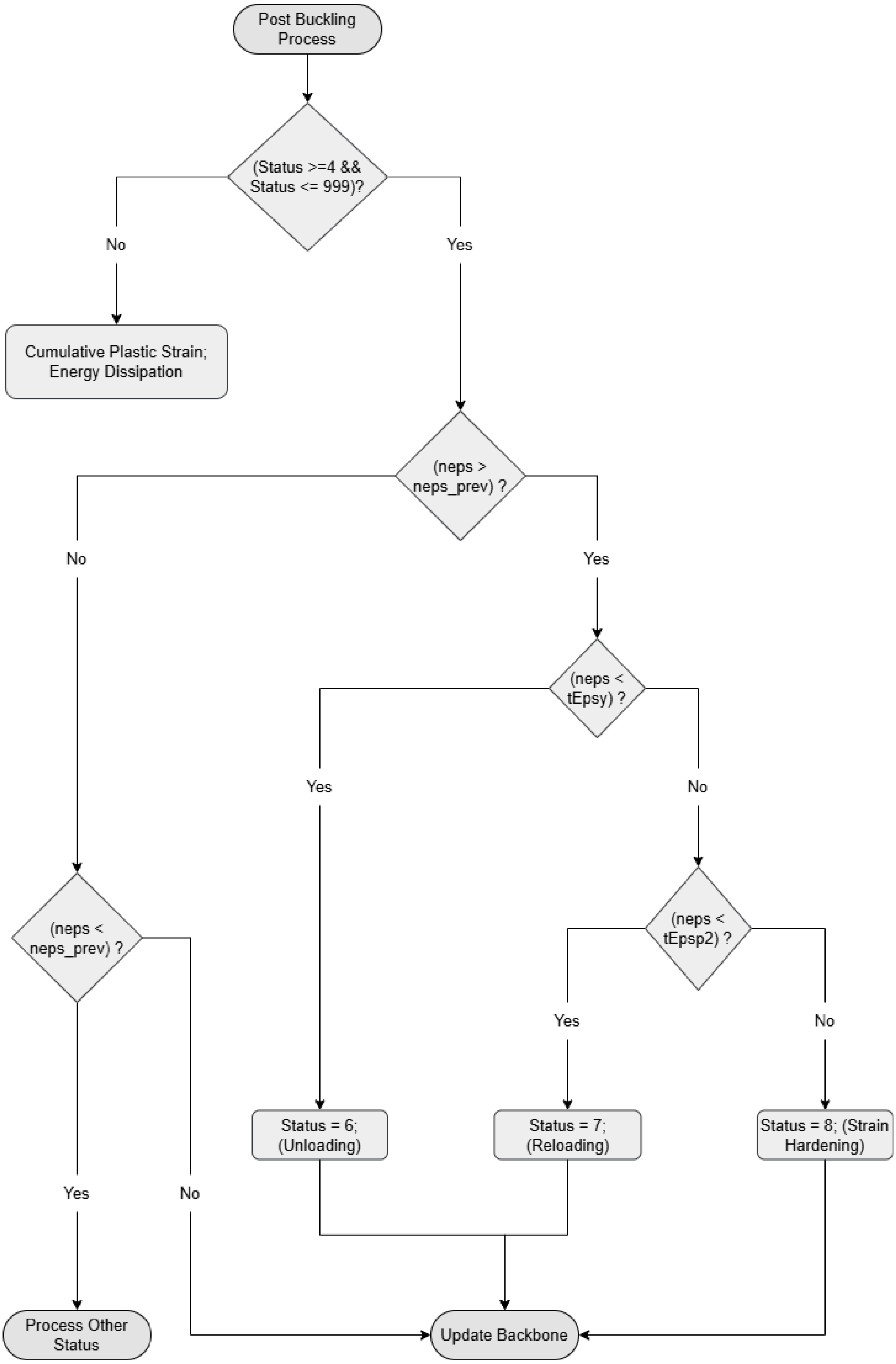

Figure A.8 Post buckling stage (status 6, 7, and 8)

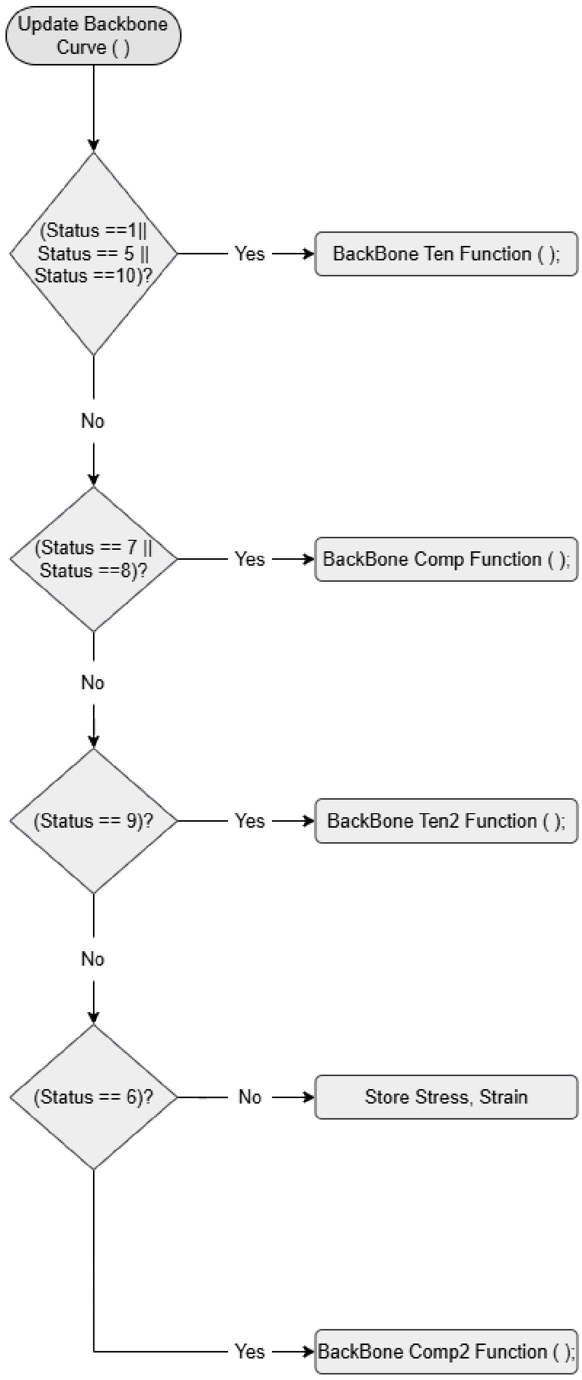

Figure A.9 Post buckling stage (Update backbone curve)